Adaptive Wavelet-Based Direct Numerical Simulations of Rayleigh-Taylor Instability

by

Scott J. Reckinger

M.S., Mech. Eng., University of Colorado Boulder, 2010

B.S., Actuarial Science, University of St. Thomas, 2006

B.A., Mathematics, University of St. Thomas, 2006

A thesis submitted to the

Faculty of the Graduate School of the

University of Colorado in partial fulfillment

of the requirements for the degree of

Doctor of Philosophy

Department of Mechanical Engineering

2013

This thesis entitled:
Adaptive Wavelet-Based Direct Numerical Simulations of Rayleigh-Taylor Instability
written by Scott J. Reckinger
has been approved for the Department of Mechanical Engineering

Prof. Oleg V. Vasilyev

Dr. Daniel Livescu

Prof. David R. Kassoy

Prof. Peter E. Hamlington

Prof. John P. Crimaldi

Date

The final copy of this thesis has been examined by the signatories, and we find that both the content and the form meet acceptable presentation standards of scholarly work in the above mentioned discipline.

Reckinger, Scott J. (Ph.D., Mechanical Engineering)

Adaptive Wavelet-Based Direct Numerical Simulations of Rayleigh-Taylor Instability

Thesis directed by Prof. Oleg V. Vasilyev

The compressible Rayleigh-Taylor instability (RTI) occurs when a fluid of low molar mass supports a fluid of higher molar mass against a gravity-like body force or in the presence of an accelerating front. Intrinsic to the problem are highly stratified background states, acoustic waves, and a wide range of physical scales. The objective of this thesis is to develop a specialized computational framework that addresses these challenges and to apply the advanced methodologies for direct numerical simulations of compressible RTI. Simulations are performed using the Parallel Adaptive Wavelet Collocation Method (PAWCM). Due to the physics-based adaptivity and direct error control of the method, PAWCM is ideal for resolving the wide range of scales present in RTI growth. Characteristics-based non-reflecting boundary conditions are developed for highly stratified systems to be used in conjunction with PAWCM. This combination allows for extremely long domains, which is necessary for observing the late time growth of compressible RTI. Initial conditions that minimize acoustic disturbances are also developed. The initialization is consistent with linear stability theory, where the background state consists of two diffusively mixed stratified fluids of differing molar masses. The compressibility effects on the departure from the linear growth, the onset of strong non-linear interactions, and the late-time behavior of the fluid structures are investigated. It is discovered that, for the thermal equilibrium case, the background stratification acts to suppress the instability growth when the molar mass difference is small. A reversal in this monotonic behavior is observed for large molar mass differences, where stratification enhances the bubble growth. Stratification also affects the vortex creation and the associated induced velocities. The enhancement and suppression of the RTI growth has important consequences for a detailed understanding of supernovae flame front acceleration and fuel capsule designs for inertial confinement fusion.

Dedication

For my little exploding star, Birk Oliver.

For Connor Nicholas, Katelynn Lee, and Merith Jade.

Just go with the flow...

Acknowledgements

Dr. Oleg V. Vasilyev, my advisor at CU-Boulder, has played a pivotal role in my development as a scientist, but has also provided me with a multitude of rare and exciting opportunities. He has taught me how to be flexible, tenacious, and persistent. Dr. Vasilyev's experience in computational fluid dynamics has been crucial to my educational growth. The opportunity to work at LANL as a doctoral candidate with my second advisor, Dr. Daniel Livescu, is invaluable. Dr. Livescu's expertise on Rayleigh-Taylor instability is irreplaceable and without it, my doctoral work would not be as successful. I would like to thank my thesis defense committee members, Dr. David Kassoy, Dr. Peter Hamlington, and Dr. John Crimaldi. Also, thank you to Dr. Olivier DesJardins and Dr. Kamran Mohseni for their service on my comprehensive exam committee. For all the helpful discussions, thanks to my Multi-Scale Modeling and Simulation Lab mates: Alireza Nejadmalayeri, Alexei Vezolainen, Jonathan Regele, Qianlong Liu, Eric Brown-Dymkoski, and Nurlybek Kasimov. To my other CU-Boulder friends, thanks for all the laughs.

To my parents, my formal educational journey may be coming to an end, but because of your steadfast support and love, I will never stop learning. To my siblings and their families, thanks for being fans.

Most importantly, I would be lost without my number one collaborator, my favorite classmate, my crux, my hero, my personal chef, my best friend, Dr. Shanon Reckinger. I am so proud of you. Lastly, thank you CU, for a doggone good time.

Contents

Chapter

Tables

Table

Figures

Figure

Chapter 1

Introduction

1.1 Motivation and Objective

The great physicist, Albert Einstein, is quoted as saying "Look deep into nature, and then you will understand everything better." Scientists have been doing so for millennia, and the discoveries made about the natural world are endless. Turbulence and turbulent mixing have been studied for decades, yet the true nature of turbulence remains one of the greatest and most pressing unresolved scientific mysteries. Fundamental questions about the physics of the turbulent mixing between fluids at unstably stratified interfaces have yet to be answered. Rayleigh-Taylor instability arises from the vorticity generated at perturbed interfaces, in which the direction of the mean density gradient is opposite an acceleration, due to gravity-like body forces, accelerating fronts, or local differential motions [69, 82]. The instability occurs in a wide variety of astrophysical, atmospheric, oceanic, and geophysical flows and plays crucial roles in many engineering applications. The same physics involved with an overturned glass of water spilling to the floor can explain why some exploding stars appear as brilliant flashes of light, on astrophysical timescales, that are visible across the universe and are used to measure galactic distances. The universality of the turbulent mixing throughout the universe is truly remarkable.

The success of previous experimental, theoretical, and computational investigations of Rayleigh-Taylor instability lies in both the new physics that have been unveiled and the doors of new exploration that have been opened. Much is known about the early growth of the instability, as small interfacial perturbations grow exponentially until the amplitudes of the disturbances are sufficiently

large. Bubble and spike structures form as the two fluids interpenetrate each other. Models for the asymptotic behavior of individual perturbations have been successful, yet the transition from linear to nonlinear growth is not fully understood. For Rayleigh-Taylor systems in nature, modal perturbations couple, forming larger structures and an acceleration of the mixing region. As the bubbles merge, the flow experiences a self-similar growth, where the dominant bubble size is proportional to the mixing layer height. In this regime, a theoretical universal growth factor can be measured. The influence of the mixing on the growth rate has profound consequences for many applications, such as the thermonuclear flame front propagation in type Ia supernovae [9]. The full effects of compressibility, background stratification, diffusivity, density differences, and initial conditions on the growth of the instability needs further investigation.

The dependence of the late-time growth on the initial small amplitude perturbations is of critical importance, since long wavelength perturbations are uncontrolled in experiments. Therefore, numerical simulations must be employed for the full characterization of the initial conditions, and thus a full and reliable understanding of the Rayleigh-Taylor system.

Simulations of real Rayleigh-Taylor applications, as well as most turbulent flows, are challenged by the need to cover a vast dynamic range of scales. For example, the complete resolution of an exploding white dwarf star would require a computational grid spanning twelve orders of magnitude in scale. Rayleigh-Taylor instability is generated by small scale motions at the interface, which develop into large structures as the fluids mix. Therefore, subgrid-scale turbulence models must take into account the additional mixing dynamics beyond the generally accepted Kolmogorov energy cascade, where all turbulence is produced at large scales. Whereas large-eddy simulations have been successful at studying the self-similar growth of the instability [25], obtaining a detailed understanding of the physics of Rayleigh-Taylor instability lies in the use of direct numerical simulations. Recently, some of the largest direct numerical simulations of turbulent flows to date have been carried out in order to study Rayleigh-Taylor instability. These studies have shed new light on the important role Rayleigh-Taylor mixing plays in the violently expanding flame fronts of type Ia supernovae, which is critical to the luminosity variation observed here on Earth.

Most of the current research focuses on the incompressible Rayleigh-Taylor instability. However, most systems where Rayleigh-Taylor instability occurs naturally involve highly compressible fluids. When the compressive nature is overlooked, the simplified system is easier to deal with, but much of the physics is lost. When considering the compressible case, one must account for highly stratified flows, acoustic waves, and a wide range of physical scales. Direct numerical simulations of compressible Rayleigh-Taylor instability require the use of a specialized computational framework that efficiently handles all of these issues, which is the main focus of this dissertation.

1.2 Methodology

Simulations of an exploding star where all relevant scales of motion are resolved is not likely to occur anytime in the foreseeable future, but smaller Rayleigh-Taylor systems where the dynamical range cover many orders of scale magnitudes, offer crucial insight into the physics of the turbulent mixing. Due to the wide range of scales and three-dimensionality requirement intrinsic to turbulent flows, the need for reliable and computationally affordable predictions of Rayleigh-Taylor instability necessitates the use of inventive numerical methods. Since computing power, memory, and time are all scarce resources for the simulation of turbulent systems, the efficiency of a numerical methodology depends heavily on the grid used to represent the flow. Adapting the grid to match the local dynamical scales is specifically advantageous for systems where the important dynamics remain in localized regions of the flow, such as Rayleigh-Taylor instability. Adaptive mesh refinement techniques have been applied to the simulation of Rayleigh-Taylor instability [25], but the grid generation for these methods is often overly expensive or unrelated to the accuracy of the solution.

The use of wavelets in representing the evolution of flow variables offers a natural way to dynamically adapt the mesh as the flow evolves. Thus, the computational resolution matches the local structures within the system, with minimal extra cost associated with the grid adaptivity. The Parallel Adaptive Wavelet Collocation Method uses a wavelet representation of the relevant variables for the computation of partial differential equations, while retaining a direct accuracy

control, since the error is directly dependent upon the number of wavelets used to approximate the solution. Due to its efficient use of computational resources, the method has the potential to push the current limits on the leading direct numerical simulations of turbulent Rayleigh-Taylor flows.

1.3 Organization

The remainder of the dissertation is organized as follows. Chapter 2 has a thorough discussion on the background of Rayleigh-Taylor instability, including its role in relevant systems, a classical view of its growth, the physics and models that are used to represent its growth, and a summary of previous scientific advances. The numerical tools employed for this work are also introduced in Chapter 2. The advanced computational framework developed for performing direct numerical simulations of compressible Rayleigh-Taylor systems is presented in Chapter 3. This includes boundary conditions that efficiently handle acoustic waves with minimal wave reflection, consistent initialization derivations, and a presentation of efficient time integration schemes. The computational tools are then applied to a vast set of Rayleigh-Taylor instability simulations, and the results are presented in Chapter 4. The feasibility of the computational framework is tested by comparing the results in the incompressible limit with well established theoretical and computational work. The compressibility effects on the growth of Raleigh-Taylor instability are investigated, with a focus on the density stratification and the late-time vortex dynamics. The viscous and dimensionality effects on compressible Rayleigh-Taylor instability are also presented.

A brief introduction is given at the beginning of each chapter that includes a summary of the motivation and background information necessary for a complete understanding of the subject matter. The intent is to have chapters that can be read independently for a detailed look into a particular topic. Of course, the most thorough picture is painted with a full reading of the dissertation.

Chapter 2

Background

Lord Rayleigh was investigating the formation of cirrus clouds when he first considered the unstable situation of a light fluid supporting a heavy fluid. The unstable configuration had been occurring in the clouds long before Rayleigh first derived its motion in 1880. He considered the simplest case with two incompressible immiscible fluids in Earth's gravitational field, where the heavy fluid lies on top of the light fluid [69]. Then, in 1950, Sir G. I. Taylor extended the analysis for accelerations other than gravity [82]. As he speculated, light fluids had been pushing on heavy fluids all across the universe well before the instability was named after Rayleigh and Taylor, shown in Figure 2.1. Since then, scientists have discovered a world of wonders hidden in the dynamics of the seemingly simple interfacial instability. Numerous observations of Rayleigh-Taylor instability (RTI) occurring in real systems have broadened the scope of its importance, while countless experiments and simulations have deepened our understanding.

A complete background of the physics, models, and methods that are utilized in the following chapters is provided here. The general dynamics are presented first, including technically relevant Rayleigh-Taylor (RT) systems and a qualitative picture of its growth. Then, the governing equations are given, followed by a number of models for various flow regimes, including the early-time linear growth, transition to non-linear growth, and self-similar scaling. Next, the most influential numerical simulations and experiments of RTI are discussed. Lastly, applicable numerical techniques are presented, including an adaptive multiresolution method and characteristics-based boundary conditions.

(a) Lord Rayleigh (b) Sir G. I. Taylor

Figure 2.1: Rayleigh and Taylor, namesakes of the interfacial instability.

2.1 The Dynamics of Rayleigh-Taylor Instability

RTI occurs when a light fluid lies underneath and, thus, supports a heavier fluid in the presence of gravity. More generally, RTI develops whenever a light fluid pushes on a heavier fluid [12, 69, 82]. Small disturbances in the interface lead to vorticity generation and the growth of the instability. Turbulence and mixing ensue near the interface as the system seeks to reduce the combined potential energy of the two fluids. The lighter fluid penetrates into the heavier fluid in the form of bubbles, while a spike of heavier fluid falls into the lighter fluid. The bubble and spike terminology is used to signify the difference in the cross-sectional area occupied by the respective fluid structure. That is, the bubbles of light fluid rising encompasses a larger cross-sectional area than that of the falling spikes of heavy fluid. The relative difference in cross-sectional area is intensified as the density difference is increased. Since RTI results from such simple system configurations, that is fluids of differing densities within an accelerating field, it plays a major role and has vast consequences in many systems of technical relevance.

2.1.1 Rayleigh-Taylor Instability in Real Systems

RTI occurs in a wide-range of natural and human-engineered flows, from the largest systems in the universe, namely galaxies, to small-scale engineering applications, such as the turbulent mixing in inertial confinement fusion. On the galactic scale, magnetic fields and cosmic rays acting perpendicular to the plane of a galaxy can push dense interstellar gas into the ambient medium,

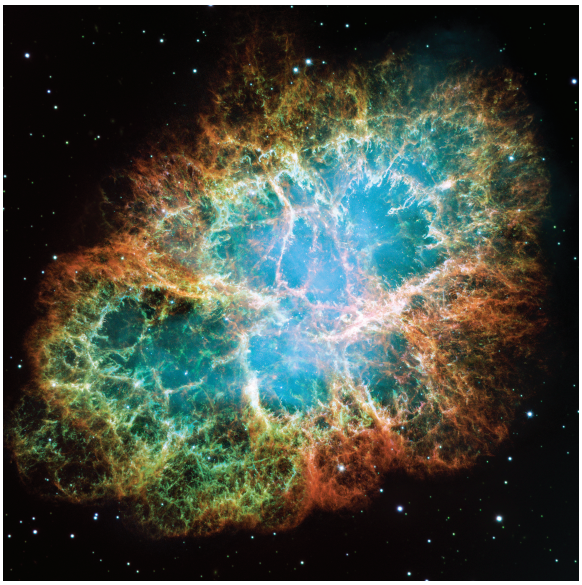

Figure 2.2: RT structures in the Crab Nebula.

resulting in the instability [100]. The spikes are visible as finger-like structures in the M83 galaxy. RTI has recently been found to play a dominant role is the thermonuclear flame acceleration in type Ia supernovae [28, 74, 78, 99]. A white dwarf accretes mass from its partner, a newly formed giant, until it reaches a critical mass of 1.38 solar masses at which it cannot sustain itself. Ignition occurs near the center of the star, triggering an expanding wave. As carbon and oxygen are fused into heavier elements, a violent explosion occurs, which irradiates a large and predictable amount of light. These "standard candles" are then used as cosmic rulers to measure distances across the universe, which are then used to investigate dark energy and the expansion of the universe. Uncertainties in the measurements arise due to slight variations in the brightness of type Ia supernovae. As the flame accelerates outward, the material behind the front has expanded and is much hotter than the surrounding gas. Thus, the hot, light fluid pushes on the cold, heavy fluid. The RT processes assist the churning of raw material inside the star and provide fresh fuel to the reaction, which leads to acceleration of the frame front. Again, the instability shows itself as finger-like structures, as observed in the Crab Nebula in Figure 2.2. In order to truly standardize these cosmic rulers, a detailed understanding of RTI is necessary.

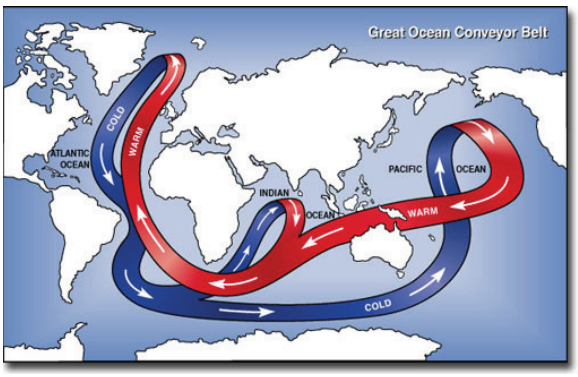

Figure 2.3: The Thermohaline Circulation (often referred to as the Great Ocean Conveyer Belt) is a large-scale ocean circulation driven by global density gradients.

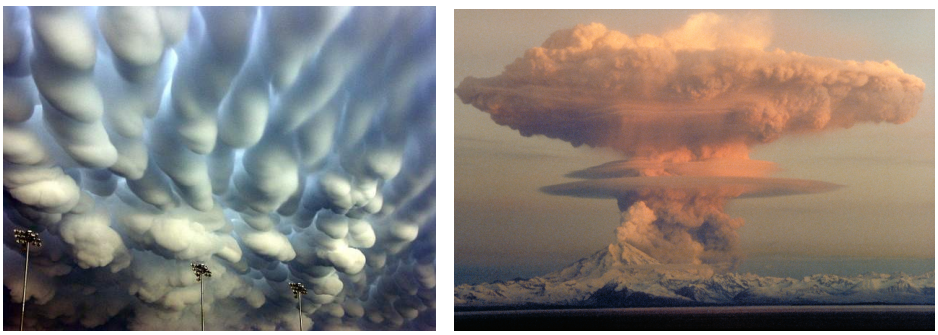

(a) Mammatus Cloud (b) Mushroom Cloud

Figure 2.4: Cloud formations caused by RTI.

RTI also occurs naturally in the Earth's oceans, atmosphere, and crustal rocks. The Thermohaline Circulation, shown in Figure 2.3, is a large-scale ocean circulation pattern that is party driven by descending plumes of heavy, salty water in the North Atlantic Ocean [19]. Strong winds from Greenland and Iceland drive evaporation in this reagion, leaving the upper layers of the ocean saltier and heavier. Due to the unstable configuration, the salty waters plummet to the depths of the ocean, driving the abyssal ocean circulation. The Thermohaline Circulation is responsible for carrying the warm waters north from the equator, keeping the climate in Europe rather mild [11]. Similarly, RTI occurs in the atmosphere whenever temperature inversions exist, which can explain the formation of mammatus and mushroom clouds, shown in Figure 2.4. Buoyancy is also the driving force in the formation of salt domes within the Earth's crust [91]. A salt dome occurs

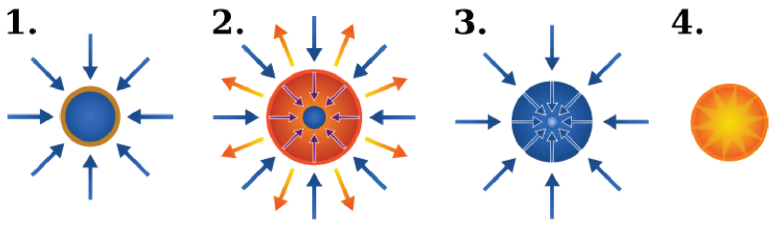

Figure 2.5: The process of inertial confinement fusion consists of (1) heating of the capsule surface, (2) surface blow-off and fuel compression, (3) ignition at the core, and (4) thermonuclear burn of the fuel.

when a layer of evaporite material, typically salt, becomes buried by increasingly denser sediment. Rock salt maintains a low density under high pressure. The density inversion leads to the rising plumes typical of an RT system.

All forms of nuclear fusion known to man are affected by RTI. Nuclear fusion requires a large amount of kinetic energy to overcome the electrostatic repulsion, known as the Coulomb barrier. In order to break the barrier and cause ignition, external energy must be confined efficiently. Gravitational confinement only occurs in stars, such as type Ia supernovae, due to the large amount of mass needed to achieve the energy confinement time requirement. The idea of inertial confinement fusion is to apply large amounts of energy uniformly over the surface of a fuel-filled capsule, causing a symmetric implosion, extreme heating, and a thermonuclear burn of the fuel. The process is shown in Figure 2.5. The fuel is often a deuterium-tritium mix. Laser beams uniformly impinge rapid bursts of energy on the capsule. The heated surface violently blows off, causing a rapid compression of the deuterium-tritium fuel. If the implosion remains spherically symmetric, the fuel reaches extremely high pressures and temperatures, and ignition occurs at the core. Ideally, the entire capsule undergoes a thermonuclear burn, offering a high energy gain, which can be cultivated as a sustainable civilian energy source. However, asymmetries in the compression can occur from various sources, such as uneven heating or capsule inconsistencies. These asymmetries will lead to RTI since the light, hot fluid pushes against the heavy, unburned fuel, resulting in a loss of energy [43, 44]. RTI plays a crucial role in the feasibility of utilizing nuclear fusion power for controlled civilian purposes.

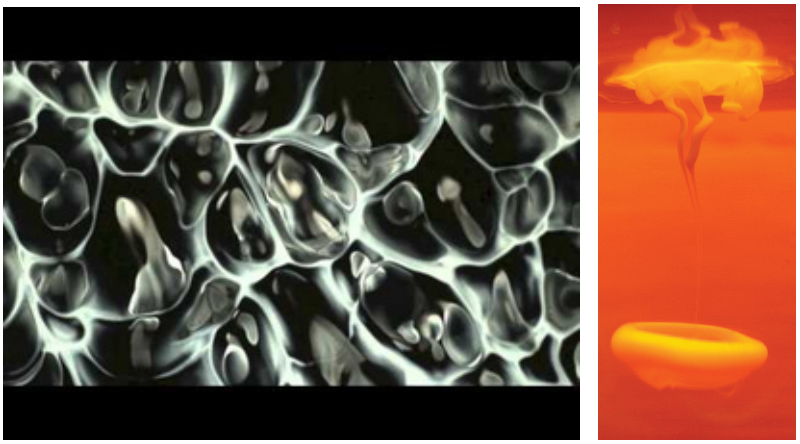

(a) Accidental Painting (b) Cream and Tea

Figure 2.6: The beauty of RTI. (The "Accidental Painting" image is borrowed from a movie created by Dr. Sandra Zetina and Dr. Roberto Zenit at the National Autonomous University of Mexico. The "Cream and Tea" image is borrowed from Chris Ostoich, taken as part of a Flow Visualization course at the University of Colorado.)

Rayleigh-Taylor instability also affects biological systems and occurs in everyday societal life. Sonoluminescence, a quirky physical phenomenon, is the creation of light bursts from imploding gas bubbles within a liquid, when the bubbles are excited with acoustic waves. The bubble eventually collapses due to instabilities at the interface. Thus, RTI limits the driving pressure for the occurrence of sonoluminescence [49]. Similarly, snapping shrimp (also referred to as pistol shrimp) get their name by rapidly shutting their claws, generating a water jet and a cavitation bubble that collapses due to RTI and gives off a snapping sound [87]. They use this mechanism to stun and capture small fish as prey.

As with almost any fluid phenomenon that occurs naturally and frequently, if visualized appropriately, RTI can lead to beautiful art, as offered in Figure 2.6. Artist David Alfaro Siqueiros first discovered the accidental painting technique in the 1930s, by pouring different color paints, which naturally have differing densities, onto a wooden panel and allowing the various colors to infiltrate one another. The result is a structure of Rayleigh-Taylor bubbles. Humans also observe RTI on a daily basis, such as simply pouring cream (heavy fluid) into coffee (light fluid).

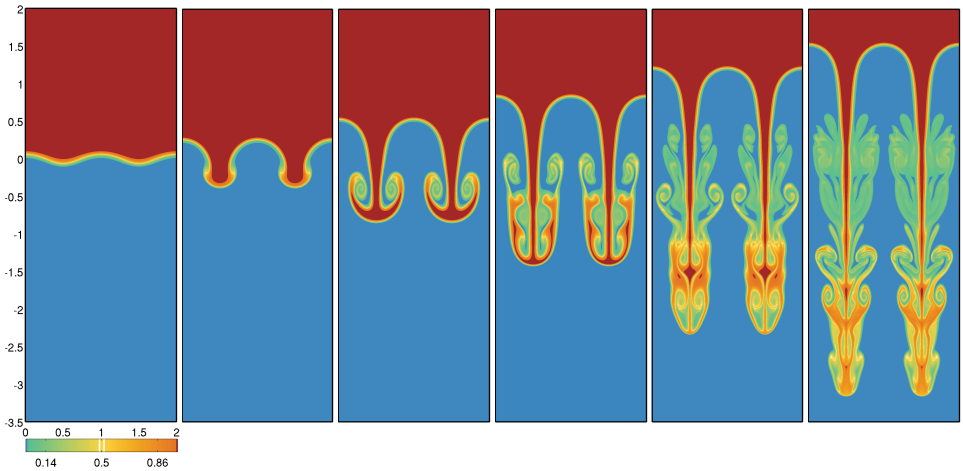

Figure 2.7: The growth of RTI from initial small-amplitude perturbations, through the linear growth stage, to the late-time nonlinear growth of the bubble and spike structures. The images result from the direct numerical simulations presented in Chapter 4.

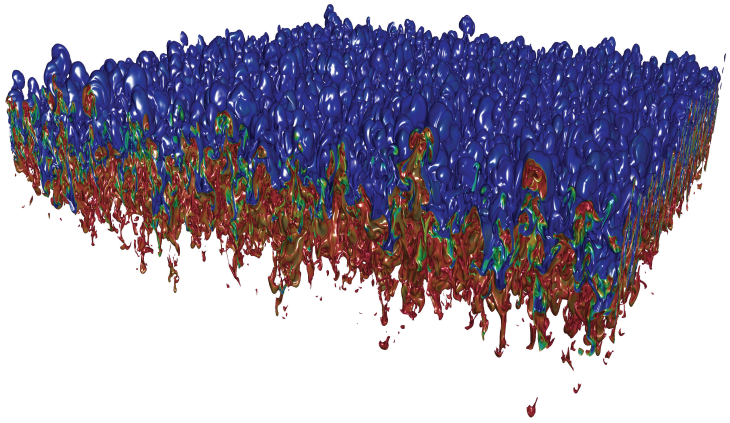

Figure 2.8: Bubbles and spikes evident in the largest RTI direct numerical simulation to date. The image, titled "Spikes and Bubbles in Turbulent Mixing: High Atwood Number Rayleigh-Taylor Instability," has been kindly provided by D. Livescu (LANL), M. R. Petersen (LANL), S. L. Martin (Ohio State University), and P. S. McCormick (LANL).

2.1.2 Classical Rayleigh-Taylor Instability

The evolution of RTI involves an early-time linear growth regime, late-time nonlinear growth of the bubble and spike structures, and a turbulent mixing layer [93]. The evolutionary stages of two-dimensional, miscible RTI growth are shown in Figure 2.7. Small perturbations of the interface experience linear growth until the amplitude reaches a significant fraction of the initial

perturbation wavelength. The linear growth rate is affected by viscosity, diffusion, compressibility, surface tension, and finite density gradients [27, 46, 53]. As the interface evolves, fluid structures evolve as the fluids interpenetrate each other. The molar mass ratio of the two fluids plays a major role in the shape and size of the structures. The Atwood number is a nondimensional quantity that represents the molar mass ratio, defined as

$$A = \frac{W_2 - W_1}{W_2 + W_1}, \tag{2.1}$$

where W_1 and W_2 are the molar masses for the bottom and top fluids, respectively. The requirement for instability is $W_1 < W_2$. For the incompressible case, the Atwood number is equivalently defined as

$$A = \frac{\rho_2 - \rho_1}{\rho_2 + \rho_1}, \tag{2.2}$$

where ρ_1 and ρ_2 are instead the densities of the bottom and top incompressible fluids, respectively. The Atwood number ranges from 0 to 1, and is a measure of the variable density effects in the flow. For high density differences where A is near 1, for example air interpenetrating helium, light fluid forms rounded bubbles with circular cross section, while the the heavy fluid penetrates the light fluid as spikes and curtains between the bubbles. A horizontal cross section of this instability has a honeycomb appearance. The bubble and spike formations are visible in Figure 2.8, which displays the density field obtained from the largest direct numerical simulation of RTI to date, with $A = 0.75$ on a $4096^2 \times 2304$ mesh. For small density ratios, A is close to 0, and the system is more symmetric with two sets of interpenetrating bubbles. In addition to variable density effects, the formation of these structures is also greatly affected by the dimensionality of the system. The evolution of structures with various characteristic sizes are affected by nonlinear interactions when the initial perturbation is multi-mode. For small amplitude initial perturbations, the nonlinear interaction between the smaller structures dominate the growth of the instability, and memory of the initial conditions is lost [15, 18, 75]. Bubble amalgamation occurs, where large bubbles absorb smaller bubbles, causing the larger structures to grow in size and accelerate. Secondary instabilities develop and affect the growth of the flow structures. The Kelvin-Helmholtz instability

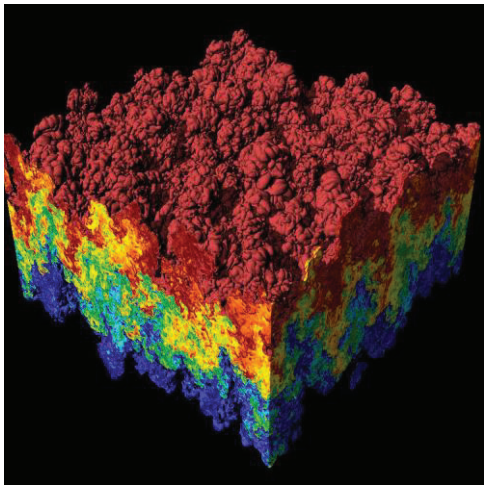

Figure 2.9: The mixing layer from a RTI simulation on a 3072^3 mesh with $A = 0.5$ [9].

is a shear force induced instability that forms along the side of the spikes as cat-eye structures. The tangential velocity variations near the tip of the spike apply additional drag forces and cause a Kelvin-Helmholtz type of mushrooming. Compressibility, diffusivity, and viscous effects on the late-time instability behavior is not currently fully understood. Throughout the growth of the instability, the majority of the system remains quiescent, since the flow structures remain localized in the relatively small mixing layer near the interface where the instability evolves and turbulence ensues.

2.1.3 Homogeneous Isotropic Turbulent Mixing

Turbulent flows that involve the mixing of fluids with different densities are classified as variable density (VD) flows. The fluids participating in VD flows are typically assumed incompressible such that the turbulent Mach number is small, and the motions within the flow remain relatively slow. However, the velocity field is not divergence free due to the change in the specific volume as molecular mixing occurs. VD flows are present in atmospheric, oceanic, and astrophysical systems, and play important roles in many combustion and chemical engineering applications [32]. RTI is a fundamental example of VD flows.

At late-times in the growth of RTI, the core of the turbulent mixing layer approaches statis-

tical homogeneity. The fluid near the edges of the layer experience inhomogeneous mixing, evident in the asymmetry of the bubble and spike structures. Once the flow has developed far enough such that little pure fluid reaches the centerline, the turbulent statistics become homogeneous [75]. Figure 2.9 shows the mixing region of a large direct numerical simulation of the instability. To investigate the turbulent processes within the mixing layer, homogeneous RT systems are studied, where the two fluids of differing molar masses are initialized as random blobs of pure fluid and are mixed by turbulent motions generated from a gravitational body force. Buoyancy effects cause the two fluids to move in opposite directions. At high Atwood numbers, asymmetric mixing due to RTI is apparent since the different structures appear on opposite sides of the mixing layer, that is spikes are formed on the light fluid side, and bubbles are formed on the heavy fluid side. Thus, the pure heavy fluid penetrates deeper into the pure light fluid than the light fluid penetration depth. However, the mixing is also asymmetrical for the homogeneous RT systems [54, 55]. For high molar mass ratios, the two pure fluids mix at different rates, with the pure heavy fluid lasting to later times than the pure light fluid. Previously, none of the mixing models used to study RT turbulence considered the faster mixing rate of the light fluid.

2.2 Conservation Laws and Analysis

The conservation of mass, momentum, energy, and species mass fraction govern the growth of RTI. In general, the instability is fully described by the compressible Navier-Stokes, energy, and species mass fraction transport equations. At early times, small perturbations grow consistent with linear stability theory, which provides analytical solutions for the growth of the instability. The linear growth rate depends on viscous, diffusive, compressibility, and finite density gradient effects, among others. For single-mode systems, analytical models predict asymptotic terminal velocities for the bubble and spike structures. Conversely, a multi-mode perturbation leads to the generation of larger and larger structures. At late times, the flow may forget the initial conditions and grow self-similarly.

2.2.1 Governing Equations

RT systems are governed by the compressible Navier-Stokes, energy, and species mass fraction transport equations, where, Y_1 corresponds to the mass fraction of the bottom fluid and Y_2 is the top fluid mass fraction. Along with an equation of state, such as the ideal gas law, $p = \rho RT$, the dimensional form of the governing equations are [90]

$$\frac{\partial \rho}{\partial t} + \frac{\partial \rho u_j}{\partial x_j} = 0, \tag{2.3}$$

$$\frac{\partial \rho u_i}{\partial t} + \frac{\partial \rho u_i u_j}{\partial x_j} = -\frac{\partial p}{\partial x_i} - \rho g_i + \frac{\partial \tau_{ij}}{\partial x_j}, \tag{2.4}$$

$$\begin{aligned} \frac{\partial \rho e}{\partial t} + \frac{\partial \rho e u_j}{\partial x_j} &= -\frac{\partial p u_i}{\partial x_i} - \rho u_i g_i + \frac{\partial \tau_{ij} u_i}{\partial x_j} \\ &\quad + \frac{\partial}{\partial x_j}\left(k \frac{\partial T}{\partial x_j}\right) + \frac{\partial}{\partial x_j}\left(D \rho c_{p_l} T \frac{\partial Y_l}{\partial x_j}\right), \end{aligned} \tag{2.5}$$

$$\frac{\partial \rho Y_l}{\partial t} + \frac{\partial \rho Y_l u_j}{\partial x_j} = \frac{\partial}{\partial x_j}\left(D \rho \frac{\partial Y_l}{\partial x_j}\right), \tag{2.6}$$

where ρ is the density, p is the pressure, T is the temperature, R is the gas constant, u_i is the velocity in the x_i direction, and the specific total energy is defined as

$$e = \frac{1}{2} u_i u_i + c_p T - \frac{p}{\rho}. \tag{2.7}$$

In the presentation of the governing equations, summation over repeated indices is assumed. The viscous stress, assuming Newtonian fluids, is defined as

$$\tau_{ij} = \mu \left(\frac{\partial u_i}{\partial x_j} + \frac{\partial u_j}{\partial x_i} - \frac{2}{3} \frac{\partial u_k}{\partial x_k} \delta_{ij} \right). \tag{2.8}$$

The gravitational acceleration is constant in the vertical, x_1, direction, that is $g_i = g\delta_{i1}$. Fluid properties, such as the dynamic viscosity, μ, heat conduction coefficient, k, specific heats at constant pressure and volume, c_p and c_v, and mass diffusion coefficient, D, are typically mass-averaged quantities, defined as linear combinations of the individual species' properties using the mass fractions. For example, the specific heat at constant pressure is defined as $c_p = c_{p_l} Y_l$, where summation over repeated indices is once again used. The RT system is composed of a heavy fluid lying on top of a lighter fluid in the vertical direction with the interface located at $x_1 = 0$. The requirement

for instability is for the top fluid molar mass to be greater than that for the lower fluid, that is $W_1 < W_2$. The gas constant for the mixture can be calculated as

$$R = R_l Y_l = \mathcal{R}\frac{Y_l}{W_l}, \tag{2.9}$$

where $\mathcal{R}$ is the universal gas constant.

2.2.2 Linear Stability Analysis

When small amplitude perturbations are applied to the interface between two superposed fluids, the disturbances grow exponentially for early times [12]. Linear stability theory assumes a base state, to which small amplitude perturbations are added. The small perturbation quantities allow analysis of the linearized equations. The flow variables are written as the sum of the base state and the perturbed field. For example, the pressure is defined as $p = p^0 + p'$, the density is defined as $\rho = \rho^0 + \rho'$, and the velocity is defined as $u_i = u_i^0 + u_i'$. For a given perturbation wavenumber k, the interface location is

$$\eta_I(x_2, x_3, t) = \eta_A \exp\left[i(k_2 x_2 + k_3 x_3) + nt\right], \tag{2.10}$$

where n is the linear growth rate, η_A is the initial perturbation amplitude, and the perturbation wavenumber has components only in the horizontal directions, k_2 and k_3, such that $k^2 = k_2^2 + k_3^2$. The growth rate for the incompressible case has the simplest form,

$$n_{\text{inc}} = \sqrt{Agk}. \tag{2.11}$$

where the 'inc' subscript stands for 'incompressible.' An expanded linear stability analysis, which derives an upper bound for the growth rate including the effects of viscosity and diffusivity for the incompressible case, gives

$$n_{\text{vd}} = \left(\frac{Agk}{\psi} + \nu^2 k^4\right)^{1/2} - (\nu + D)k^2, \tag{2.12}$$

where ν is the kinematic viscosity and $\psi = \psi(A, k, \delta)$ has an empirical relationship with A, k, and the initial diffusion thickness of the interface δ [27]. The subscript 'vd' stands for 'viscous' and

'diffusion.' Viscosity and diffusivity inhibit growth for high wavenumbers. Thus, a most unstable wavenumber, k_u, corresponding to a most unstable wavelength λ_u, grows faster than all other wavenumbers. Also, diffusion effects prevent instability growth above a critical wavenumber, k_c, with associated wavelength λ_c. Since most theoretical and computational work on RTI focuses on the incompressible case, these are commonly used relationships for comparing simulations with the growth predicted from linear theory.

In order to extend the analysis to include compressibility effects, it is convenient to assume immiscible, inviscid fluids without surface tension effects [53]. For immiscible fluids, $D = 0$, and the system can be analyzed within each pure fluid separately. The governing equations reduce to

$$\frac{\partial \rho}{\partial t} + \frac{\partial \rho u_j}{\partial x_j} = 0, \tag{2.13}$$

$$\frac{\partial \rho u_i}{\partial t} + \frac{\partial \rho u_i u_j}{\partial x_j} = -\frac{\partial p}{\partial x_i} - \rho g_i, \tag{2.14}$$

$$\frac{\partial p}{\partial t} + \frac{\partial p u_j}{\partial x_j} = (1-\gamma) p \frac{\partial u_j}{\partial x_j}. \tag{2.15}$$

The steady base state consists of the two pure fluids at rest ($u_i^0 = 0$) with a completely flat interface. The governing equations require

$$\frac{\partial p^0}{\partial x_1} = -\rho^0 g, \tag{2.16}$$

which represents hydrostatic equilibrium. The base state superscript is replaced with 'H' to denote the hydrostatic background state. That is, $\rho^0 \rightarrow \rho^H$ and $p^0 \rightarrow p^H$. Since the fluids are in thermodynamic equilibrium, the base state temperature is constant ($T^H = T_0$), and the base state density and pressure are given by

$$\rho_m^H = \frac{P_I}{R_m T_0} \exp\left(-\frac{g x_1}{R_m T_0}\right), \tag{2.17}$$

$$p_m^H = P_I \exp\left(-\frac{g x_1}{R_m T_0}\right), \tag{2.18}$$

where P_I is the unperturbed pressure at the interface, and m denotes the fluid species.

A single-mode perturbation is applied to the interface described in (2.10). Solutions for the

perturbed quantities, ρ', p', and u_i, have similar dependencies on x_2, x_3, and time, that is

$$\rho' = \tilde{\rho}(x_1)\exp\left[i(k_2x_2+k_3x_3)+nt\right], \tag{2.19}$$

$$p' = \tilde{p}(x_1)\exp\left[i(k_2x_2+k_3x_3)+nt\right], \tag{2.20}$$

$$u_i = \tilde{u}_i(x_1)\exp\left[i(k_2x_2+k_3x_3)+nt\right]. \tag{2.21}$$

The resulting linearized equations are

$$n\tilde{\rho} = -\rho^H(D_x\tilde{u}_1+ik_2\tilde{u}_2+ik_3\tilde{u}_3)-\tilde{u}_1D_x\rho^H, \tag{2.22}$$

$$n\rho^H\tilde{u}_1 = -D_x\tilde{p}-\tilde{\rho}g, \tag{2.23}$$

$$n\rho^H\tilde{u}_2 = -ik_2\tilde{p}, \tag{2.24}$$

$$n\rho^H\tilde{u}_3 = -ik_3\tilde{p}, \tag{2.25}$$

$$n\tilde{p} = -\gamma p^H(D_x\tilde{u}_1+ik_2\tilde{u}_2+ik_3\tilde{u}_3)+\tilde{u}_1\rho^Hg, \tag{2.26}$$

where D_x denotes d/dx_1. The speed of sound $c=\sqrt{\gamma p^H/\rho^H}$ is constant within each of the pure fluid species. An equation for $\tilde{u}_1$ on each side of the interface can then be obtained as

$$D_x^2\tilde{u}_{1_m}-\frac{\gamma_m g}{c_m^2}D_x\tilde{u}_{1_m}-\left(k^2+\frac{n^2}{c_m^2}+\frac{(\gamma_m-1)g^2k^2}{n^2c_m^2}\right)\tilde{u}_{1_m}=0. \tag{2.27}$$

The perturbation solution has the form

$$\tilde{u}_{1_m}=A_m\exp(\lambda_m^+x_1)+B_m\exp(\lambda_m^-x_1), \tag{2.28}$$

where

$$\lambda_m^{\pm}=\frac{\gamma_m g}{2c_m^2}\pm k\sqrt{1+\frac{n^2}{k^2c_m^2}+\frac{(\gamma_m-1)g^2}{n^2c_m^2}+\frac{\gamma_m^2g^2}{4k^2c_m^4}}. \tag{2.29}$$

The coefficients A_m and B_m are determined from the conditions that $\tilde{u}_1$ vanishes at the boundaries or at $\pm\infty$, $\tilde{u}_1$ is continuous across the interface, and from the initial perturbation amplitude, since

$$\frac{\partial\eta_I}{\partial t}=[u_1]_{(x_1=0)}, \tag{2.30}$$

or, equivalently,

$$n\eta_A=\tilde{u}_1(0). \tag{2.31}$$

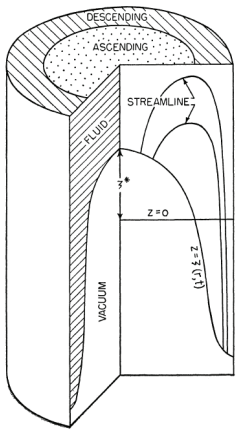

Figure 2.10: Illustration of the cylindrical model for the RT bubbles with $A = 1$ [47].

The linear growth rate with compressibility effects is obtained by applying a proper jump condition and assuming an infinite domain,

$$n_{\text{com}}^2 = k^2 g \left[\frac{\gamma_2 \left(k^2 c_1^2 + n_{\text{com}}^2\right) - \left(k^2 c_2^2 + n_{\text{com}}^2\right) \gamma_1}{\lambda_1^+ \gamma_1 \left(k^2 c_2^2 + n_{\text{com}}^2\right) - \left(k^2 c_1^2 + n_{\text{com}}^2\right) \gamma_2 \lambda_2^-} \right], \tag{2.32}$$

where the 'com' subscript stands for 'compressible.' All of the growth rate formulas have two roots, $\pm n$, such that the solutions have both growing and decaying parts. The perturbation fields for the other quantities can then be obtained from (2.22)-(2.26).

2.2.3 Early Nonlinear Stage

The transition from the early linear stage to the late-time nonlinear regime of RTI growth has received and continues to receive much attention from researchers in the field. A detailed understanding of the temporal evolution of the mixing layer for general RT systems not only has crucial significance for real systems, but also for testing the ability of models to predict the instability growth and the accuracy of numerical simulations. The structures in single-mode systems are not subject to the mode coupling and competition that are present when a broadband spectrum perturbation is applied. Thus, the late-time dynamics vary drastically, depending on the initial perturbation spectrum. Simulations that apply a single-mode perturbation are not direct representations of real RT systems. However, analysis of the single-mode case gives an upper bound for

the growth rates observed in the multi-mode systems. Furthermore, the dominant wavelength in a multi-mode system that is horizontally bounded inevitably fills the domain. Thus, these systems act like single-mode RTI at late-times.

For systems with single-mode periodic perturbations, an array of identical bubbles grow consistently with linear stability theory at early times. In the early nonlinear stages, the vorticity is still small and the instability can be described using potential flow theory or a simple buoyancy-drag model [36, 61]. These types of analyses obtain a late-time terminal velocity for the bubble and spike structures, since the speeds are large enough where the drag forces offset the buoyancy forces [66, 88]. This phenomenon was first reported by Layzer, who investigated the $A = 1$ limit, where the light fluid is a vacuum, and the heavy fluid is assumed inviscid and incompressible [47]. The model was developed for two-dimensional planar and three-dimensional cylindrical RT bubbles. An illustration of the tubular geometry is shown in Figure 2.10, for which the analysis can easily be extended to an array of bubbles where the cells are hexagonal, and the boundaries are replaced by planes of symmetry [38]. The system is analyzed with potential flow theory. Thus, the velocity is represented by a velocity potential, where $\mathbf{u} = \nabla\phi$. For this analysis, the gravitational acceleration acts in the vertical x-direction, and the components of velocity in the x, y, and z directions are u, v, and w, respectively.

For the planar instability, the bubble tip coordinates are $[\eta_0(t), y_0(t)]$, and the interface location near the tip is defined, to second order, by

$$x = \eta_I(y,t) = \eta_0(t) + \eta_2(t)(y - y_0)^2, \tag{2.33}$$

where the radius of curvature is $R = -1/2\eta_2$. The kinematic equation, which requires that the interface moves with the fluid, is

$$u_I - \dot{\eta}_0 - \dot{\eta}_2(y - y_0)^2 - 2\eta_2(y - y_0)(v_I - \dot{y}_0) = 0, \tag{2.34}$$

where the dot represents a time derivative and the velocity components of the interface are u_I and v_I. The velocity of the interface is derived from the pure fluid velocity solution taken at

the interface location. That is, $u_I = [u]_{(x=\eta_I)}$ and $v_I = [v]_{(x=\eta_I)}$. The flow is also governed by Bernoulli's equation,

$$\frac{\partial \phi}{\partial t} + \frac{1}{2}(u^2 + v^2) + gx = C, \tag{2.35}$$

where the constant, C, is the same everywhere on the interface. The velocity potential is of the form

$$\phi(x, y, t) = a(t)\cos[k(y - y_0)]e^{-k(x-\eta_0)}, \tag{2.36}$$

where $k = 2\pi/\lambda$, and λ is the perturbation wavelength. With the imposed form of the velocity potential, the kinematic equation, to zeroth and second orders of the horizontal displacement from the bubble tip $(y - y_0)$, and the second order Bernoulli's equation on the interface are

$$ak + \dot{\eta}_0 = 0, \tag{2.37}$$

$$ak^2\left(\eta_2 + \frac{k}{2}\right) - \dot{\eta}_2 + 2ak^2\eta_2 = 0, \tag{2.38}$$

$$\dot{a}k\left(\eta_2 + \frac{k}{2}\right) - \frac{a^2k^4}{2} - g\eta_2 = 0. \tag{2.39}$$

This can easily be rearranged to give the following set of ordinary differential equations:

$$\dot{\eta}_0 = -ak, \tag{2.40}$$

$$\dot{\eta}_2 = \left[\frac{ak^2}{2}\right][k + 6\eta_2], \tag{2.41}$$

$$\dot{a} = \frac{1}{k}\left[\frac{2g\eta_2 + a^2k^4}{k + 2\eta_2}\right]. \tag{2.42}$$

In order to check consistency with the linear regime, the equations are linearized for small values of a, η_0, and η_2, which gives the early evolution of the instability as

$$\dot{\eta}_0 = -ak, \tag{2.43}$$

$$\dot{\eta}_2 = \frac{ak^3}{2}, \tag{2.44}$$

$$\dot{a} = \frac{2g\eta_2}{k^2}. \tag{2.45}$$

Taking a time derivative of (2.45) gives the relationship, $\ddot{a} = gka$. The growth rate derived here, $n = \sqrt{gk}$, is equivalent to the results from linear stability analysis with $A = 1$.

In the late time asymptotic limit using this potential flow analysis, the bubble reaches a terminal velocity, defined as

$$V_b = \left[\frac{\partial \phi}{\partial x}\right]_{(x=\eta_0, y=y_0)} = -ak. \tag{2.46}$$

The evolution of the bubble height and curvature can be related by combining equations (2.40) and (2.41) as

$$\dot{\eta}_0 = -\left[\frac{2}{k(k+6\eta_2)}\right]\dot{\eta}_2, \tag{2.47}$$

which has the solution

$$\eta_0(t) = -\left[\frac{1}{3k}\right]\ln[k+\eta_2(t)] + C. \tag{2.48}$$

The integration constant is found by considering a small initial sinusoidal perturbation with amplitude $\eta_0(0)$. The solution is

$$\eta_2(t) = -\frac{k}{6} + \left[\frac{k}{6} - \frac{k}{2}\eta_0(0)\right] e^{-3k[\eta_0(t)-\eta_0(0)]}. \tag{2.49}$$

In the asymptotic limit of $\eta_0 \to \infty$, the solution converges to $\eta_2 \to -k/6$. Thus, the asymptotic radius of curvature is $R_{2D} = 3/k$. The terminal velocity formula, which is achieved by combining equations (2.40) and (2.42) and plugging in the asymptotic relationships, is $V_{b_{2D}} = \sqrt{g/3k}$.

The extension to three-dimensional, cylindrical RT bubbles makes obvious the dimensionality effect on the growth of Raylieh-Taylor instability. The bubble tip coordinates are $[\eta_0(t), \mathbf{r}_0(t)]$, where $\mathbf{r}_0 = (y_0, z_0)$. The second order formula for the location of the interface near the tip is

$$\eta_I(\mathbf{r}, t) = \eta_0(t) + \eta_2(t)\left|\mathbf{r} - \mathbf{r}_0\right|^2. \tag{2.50}$$

The velocity potential has the form

$$\phi(x, y, z, t) = a(t)\cos\left[\frac{k(y-y_0)}{\sqrt{2}}\right]\cos\left[\frac{k(z-z_0)}{\sqrt{2}}\right] e^{-k(x-\eta_0)}, \tag{2.51}$$

which gives the zeroth and second order kinematic equations, and the second order Bernoulli equation, for the three dimensional system, as

$$ak + \dot{\eta}_0 = 0, \tag{2.52}$$

$$ak^2\left(\eta_2+\frac{k}{4}\right)-\dot{\eta}_2+ak^2\eta_2=0, \tag{2.53}$$

$$\dot{a}k\left(\eta_2+\frac{k}{4}\right)-\frac{a^2k^4}{8}-g\eta_2=0. \tag{2.54}$$

The set of ordinary differential equations is

$$\dot{\eta}_0 = -ak, \tag{2.55}$$

$$\dot{\eta}_2 = \left[\frac{ak^2}{4}\right]\left[k+8\eta_2\right], \tag{2.56}$$

$$\dot{a} = \frac{1}{2k}\left[\frac{8g\eta_2+a^2k^4}{k+4\eta_2}\right], \tag{2.57}$$

which is linearized as

$$\dot{\eta}_0 = -ak, \tag{2.58}$$

$$\dot{\eta}_2 = \frac{ak^3}{4}, \tag{2.59}$$

$$\dot{a} = \frac{4g\eta_2}{k^2}. \tag{2.60}$$

The linear growth rate here is $n=\sqrt{gk}$, which is equivalent to the linear stability analysis of the planar bubble. This is an expected result since the linear growth is independent of dimensionality. In the asymptotic terminal velocity limit, the radius of curvature is $R_{3D}=4/k$, since $\eta_2\to -k/8$. The three-dimensional terminal bubble velocity is $V_{b_{3D}}=\sqrt{g/k}$. The velocity increase from two to three dimensions is due to the reduced drag per unit volume in three dimensions.

A buoyancy-drag model can be used to extend the terminal bubble velocity analysis to general Atwood number [61]. The model considers the balance of the inertial, buoyancy, and Newtonian drag forces for both the bubble and spike regions, which is consolidated by the equation

$$\left[(\rho_{\text{in}}+C_a\rho_{\text{out}})\frac{dV}{dt}-\beta(\rho_{\text{out}}-\rho_{\text{in}})g\right]\left[\text{Volume}\right]=-C_d\rho_{\text{out}}V\left|V\right|\left[\text{Area}\right], \tag{2.61}$$

where $V=dh/dt$ is the velocity of the spike ($\rho_{\text{in}}=\rho_2$ and $\rho_{\text{out}}=\rho_1$) or bubble ($\rho_{\text{in}}=\rho_1$ and $\rho_{\text{out}}=\rho_2$), and h is the amplitude of penetration into the outer fluid [20]. The coefficient C_a represents an added mass effect since the fluid being penetrated is displaced by the motion. In general, the coefficient depends on the shape and volume fraction of the penetrating objects. A

reduction in the effect of buoyancy due to finite density gradients from the fluid mixing is applied through the factor $\beta < 1$. The drag coefficient, C_d, also depends on the shape of the bubble and spike structures. Since the inertial and buoyancy forces are proportional to the volume of the structures, whereas the drag is proportional to the cross-sectional area, longitudinal length scales, L, are introduced representing the ratio of the volume to the cross-sectional area.

In the asymptotic limit of the buoyancy-drag model, the bubbles and spikes reach terminal velocities, that is, as $t \to \infty$, $V_1 \to V_s$ and $V_2 \to V_b$. The simplest model treats the bubbles and spikes as independent tubes, with $L = h$. The structures approach terminal velocity once the amplitudes h become comparable to the wavelength, λ, so the height of the tubes is taken to be equal to the perturbation wavelength, that is $L = \lambda$. For the case of immiscible fluids, $\beta = 1$, and (2.61) becomes

$$(\rho_2 - \rho_1)g = \frac{C_d}{\lambda}\rho_{\text{out}} V_m^2. \tag{2.62}$$

Thus, the Atwood number dependent formula for the bubble and spike terminal velocities is

$$V_{b/s} = \left[\frac{2A}{(1 \pm A)}\frac{g\lambda}{C_d}\right]^{1/2}. \tag{2.63}$$

The drag coefficient is determined from the bubble terminal velocity relationships for the $A = 1$ limit, which gives $C_{d_{2D}} = 6\pi$ and $C_{d_{3D}} = 2\pi$. The added mass coefficients can also be determined from the $A = 1$ case as $C_{a_{2D}} = 2$ and $C_{a_{3D}} = 1$. The compressibility, viscous, diffusion, and surface tension effects on the terminal velocities are not fully understood.

There have also been many studies attempting to extend Layzer's potential flow analysis to general Atwood number and to both the bubble and spike. One such study uses observations of the velocity field near the tip of the bubble from simulations to set the form of the velocity potential [36]. During the early stages, the velocity takes on a maximum value at the interface and decays exponentially toward both the top and bottom of the domain. At later times in the bubble growth, the velocity continues to decay in the heavy outer fluid. However, the velocity profile of the light fluid inside the bubble is well approximated by a constant in the vertical direction and zero in the

horizontal. This motivates the application of the following form for the velocity potential:

$$\phi^h(x,y,t) = a_1(t)\cos[k(y-y_0)]e^{-k(x-\eta_0)}, \tag{2.64}$$

$$\phi^l(x,y,t) = b_1(t)\cos[k(y-y_0)]e^{k(x-\eta_0)} + b_0(t)x. \tag{2.65}$$

The kinematic condition remains unchanged. The dynamic condition, that pressure is continuous across the interface, is applied by setting the pressure terms in the pure fluid Bernoulli equations equal to one another. The resulting equation,

$$\left[\frac{\partial\phi}{\partial t} + \frac{1}{2}(u^2+v^2) + gx\right]^h_{(x=\eta_I)} - \left[\frac{\partial\phi}{\partial t} + \frac{1}{2}(u^2+v^2) + gx\right]^l_{(x=\eta_I)} = f(t), \tag{2.66}$$

introduces a time-dependent arbitrary integration constant, $f(t)$, whose solution requires the use of the zeroth order terms ($y = y_0$) of the combined Bernoulli equation. Thus, only the second order in $(y - y_0)$ equation can be used to round out the system of equations for solving the time-dependent parts of the velocity potentials. The combined Bernoulli equation is essentially an integration of the momentum equations from an arbitrary location in space to the interface. The momentum equations cannot be integrated from $x \to -\infty$ due to the assumed form of the light fluid velocity potential. The lack of a definitive integration results in the arbitrary integration constant, which represents a loss of physical information about the flow that is intrinsic to the analysis.

The resulting set of ordinary differential equations is

$$\dot{\eta}_2 = -\dot{\eta}_0\frac{k}{2}(k+6\eta_2), \tag{2.67}$$

$$\ddot{\eta}_0\left[\frac{k^2 - 4Ak\eta_2 - 12A\eta_2^2}{2(k-6\eta_2)}\right] + (\dot{\eta}_0 k)^2\left[\frac{(4A-3)k^2 + 6(3A-5)k\eta_2 + 36A\eta_2^2}{2(k-6\eta_2)^2}\right] + Ag\eta_2 = 0. \tag{2.68}$$

The form of the ordinary differential equation matches a drag-buoyancy model, where the first term corresponds to the acceleration, the second term represents the drag, and the final term is due to buoyancy. In the limit of small perturbations, the potential flow model converges to the exponential growth predicted from linear stability theory, with the correct growth rate $n_{\text{inc}} = \sqrt{Agk}$. In the asymptotic limit of $t \to \infty$, the analysis is consistent with the drag-buoyancy model. That is, $\eta_2 \to -k/6$ and

$$V_{b_{2D}} = \left[\frac{2A}{(1+A)}\frac{g}{3k}\right]^{1/2}. \tag{2.69}$$

In addition to providing an asymptotic terminal velocity, this analysis also offers a model for the evolution of the bubble height from the early linear growth stage to the constant velocity observed at later times. Despite the inconsistencies in the integration of the momentum equations, this model is able to successfully predict the evolution of the bubble height for small to moderate Atwood numbers. The model for the bubble evolution breaks down at high A.

The potential flow analysis is extended to the spike side of the interface by applying the following form of the pure fluid velocity potentials:

$$\phi^h(x,y,t) = a_1(t)\cos[k(y-y_0)]e^{-k(x-\eta_0)} + a_0(t)x, \tag{2.70}$$

$$\phi^l(x,y,t) = b_1(t)\cos[k(y-y_0)]e^{k(x-\eta_0)}. \tag{2.71}$$

The analysis is similar to the bubble side and gives an asymptotic terminal velocity as

$$V_{s_{2D}} = \left[\frac{2A}{(1-A)}\frac{g}{3k}\right]^{1/2}, \tag{2.72}$$

which matches the drag-buoyancy model result. At low Atwood numbers ($A = 0.1$), the evolution of spike is well predicted by the potential flow analysis. The model does not match the growth of the spike for moderate to high A, where a terminal velocity may never occur. At later times, observations from simulations show that the velocity profiles near the tips of the spikes do not reach a constant value as occurs within the bubbles. This is not consistent with the chosen form of the velocity potential and could be the reason for the limited success of the model. There is no consistent behavior of the velocity within the spikes at late times, mostly due to the induced motion from the vortices created near the tips of the spikes.

Until recently, the asymptotic behavior of the potential flow and buoyancy-drag models was called the terminal velocity or saturation behavior, since it was believed to describe the late time behavior of single-mode RTI [34]. However, as vorticity is generated by the Kelvin-Helmholtz instability on the sides of the bubbles and spikes, such a description becomes inadequate [89]. The late time growth varies considerably from the potential flow description. Upon reaching the asymptotic velocity, the bubble and spikes decelerate slightly, followed by a reacceleration region. During the

creation of the Kelvin-Helmholtz vortices, the friction drag is increased due to the increased surface area, which causes the deceleration in the flow. After the vortices are fully developed, the structures reaccelerate since the rolling motion acts to reduce to the friction drag between the bubbles and spikes. Additionally, the induced flow from the vortices creates a momentum jet that further propels the bubbles forward. The structures reach speeds well beyond the analytical terminal velocities. The true asymptotic behavior beyond the reacceleration region is not fully understood.

2.2.4 Self-Similarity

In practice, RTI develops from a wide range of unstable scales. In most cases, the individual structures never reach the asymptotic constant velocities present in the single-mode system due to the interactions among the various bubble and spike formations. If the initial perturbation spectrum is broad, successively larger and faster bubbles rise to the top of the mixing layer [16]. This occurs due to nonlinear mode-coupling, where short wavelength perturbations merge to form bubbles with larger diameters, and bubble competition, where long wavelength modes dominate once shorter wavelength bubbles begin to decelerate at speeds near the terminal velocity. Thus, long wavelength initial perturbations have a long lasting effect on the growth of the mixing layer.

At sufficiently late times and for idealized conditions, the flow may forget the initial conditions, due to the creation of larger bubbles from the nonlinear merging of smaller diameter bubbles. This occurs once the dominant wavelength in the flow, λ_d, becomes significantly larger than the maximum wavelength perturbation present in the initial conditions, λ_M. Since memory of the initial conditions has been lost, the width of the mixing layer depends only on the densities of the fluids, the gravitational acceleration, and time. Thus, gt^2 is the only length scale of importance. The bubbles grow self-similarly, meaning that the mixing layer height grows proportionally with the wavelength of the dominant bubbles. Dimensional arguments give

$$h_b = f(A)gt^2, \tag{2.73}$$

where h_b is the amplitude of the dominant bubbles with wavelength λ_b, and the functional rela-

tionship for the Atwood number needs to be determined. The similarity solution requires that the bubble diameter, which is approximately equivalent to the dominant wavelength, scales with the bubble height, that is $D_b \propto \lambda_b \propto h_b$. The Atwood number dependence is obtained by assuming that the time for a particular wavelength to become dominant, t_b, is a constant number of linear growth periods, N_b. That is,

$$n_b t_b = N_b, \tag{2.74}$$

where $n_b = \sqrt{2\pi Ag/\lambda_b}$ is the incompressible growth rate derived from linear stability theory associated with the dominant wavelength. At any given time the dominant wavelength scales as

$$\lambda_b \propto Agt^2. \tag{2.75}$$

Thus, the self-similar growth of the dominant bubbles is

$$h_b = \alpha Agt^2, \tag{2.76}$$

where α is a dimensionless growth parameter [1, 3]. For small Atwood numbers, the spikes have a very similar evolution. As A approaches unity, the spikes become narrow, reducing the drag drastically, and the motion approaches free fall, with $h_s \approx gt^2/2$.

Historically, the quadratic growth relationship, (2.76), derived from dimensional arguments, has been the widely accepted form for the mixing layer evolution. The growth factor is presumed constant during the self-similar growth of the instability, and can be solved for as

$$\alpha = \frac{h}{Agt^2}. \tag{2.77}$$

Many experimental [4, 24, 57, 70, 94] and computational [2, 5, 13, 16, 21, 24, 31, 33, 35, 37, 39, 41, 48, 50, 58, 61, 92, 93, 94, 95, 96] studies have attempted to determine the correct value for α by fitting a line to h versus Agt^2 once the self-similar region is believed to have begun. The difficulty in obtaining a single, correct growth parameter lies in the flow requirements necessary to apply the formula. First, to ensure that all memory of the initial conditions has been lost, the initial perturbation spectrum must be band limited, where the maximum perturbation wavelength is λ_M.

Otherwise, the exponential growth in (2.10) of the long wavelength perturbations will dominate the quadratic self-similar growth. The initial conditions are felt by the flow until $h \gg \lambda_M$, where h is the mixing layer width. Furthermore, the unstable spectrum must also be peaked near the most unstable linear growth mode (k_u), in order to prevent the exponential growth of the fastest linear mode from competing with the quadratic growth. The dominant initial perturbation wavelength, λ_0, corresponding the the peak of the wavenumber spectrum (k_0), must be approximately equal to the most unstable wavelength, λ_u. Second, boundaries must not effect the evolution of the growth controlling eddies, both horizontally and vertically. The bubble merging process halts when the dominant wavelength approaches the domain width ($\lambda_d \approx L_h$) or the height of the mixing layer approaches the domain height, ($h \approx L_v$). Additionally, as the dominant wavelength grows, the number of modes within the domain decreases, reducing the reliability of the mixing statistics. Third, diffusive and viscous effects must be negligible. The length scales associated with diffusion and viscosity must be much smaller than the mixing layer width. The viscous requirement is given by the Kolmogorov scale,

$$\eta = \left(\frac{\nu^3}{\varepsilon}\right)^{1/4}, \tag{2.78}$$

where ν is the kinematic viscosity and ε is the turbulent kinetic energy dissipation. The diffusion length scale, referred to as the Batchelor scale, is defined as

$$l_B = \frac{\eta}{Sc^{1/2}} = \left(\frac{\nu D^2}{\varepsilon}\right)^{1/4}, \tag{2.79}$$

where the Schmidt number, Sc, represents the ratio of viscous to diffusivity effects. Therefore, the Reynolds and Schmidt numbers for the flow must be sufficiently large. A summary of the requirements for the application of (2.76) is [15]

$$\lambda_0 \approx \lambda_u < \lambda_M \ll h, \;\; L_v \gg h, \;\; L_h \gg h, \;\; l_B \ll h, \;\; \eta \ll h. \tag{2.80}$$

The α conflict arises because experiments and numerical simulations each have their own difficulties in meeting all of these requirements. It is easy to achieve the high Reynolds number requirement in experiments, but it is extremely difficult to have complete control over the initial conditions.

Uncontrolled perturbations have a naturally broad spectrum. Large wavelength initial perturbations are almost always inevitable. In order for the flow to forget the initial conditions, which is a crucial aspect of self-similar growth, there must be no significant energy in the the low to moderate wavenumbers. Conversely, the initial conditions are easily controlled in a simulation, but there are resolution limitations, which restrict the range of possible Reynolds and Schmidt numbers. Viscosity and diffusion introduce additional length and time scales, which affects the self-similar growth.

A better model for the self-similar evolution of the mixing layer width can be derived using a similarity assumption [75] or a mass flux and energy balance argument [15]. The former derivation expresses the solutions to the moment equations as the product of a spatial similarity function and a temporal scaling function. The latter derivation uses the mass flux through the midplane to set the layer growth rate, and considers the terminal velocity of a falling sphere of diameter h to model the vertical velocity fluctuations. The improved formula is

$$\dot{h} = 2(\alpha A g h)^{1/2}, \tag{2.81}$$

which gives a new relationship for the dimensionless growth factor as

$$\alpha = \frac{\dot{h}^2}{4Agh}. \tag{2.82}$$

The solution for the mixing layer width is

$$h(t) = \alpha A g (t - t_0)^2 + 2(\alpha A g h_0)^{1/2}(t - t_0) + h_0, \tag{2.83}$$

where h_0 is the thickness of the layer when the flow enters self-similar growth, at time $t = t_0$. An approximate solution for the growth factor is

$$\alpha = \frac{\left[\sqrt{h(t)} - \sqrt{h(t_0)}\right]^2}{(Ag)(t - t_0)^2}. \tag{2.84}$$

The additional terms in (2.83) that are not present in the original model for the mixing layer width given in (2.76), dictate that the growth of the instability has both linear and quadratic behavior. The persistence of the linear term, and thus the accuracy of the original model, is again determined by the initial perturbation spectrum.

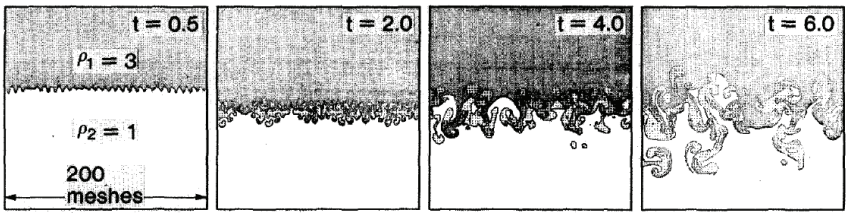

(a) Mode coupling

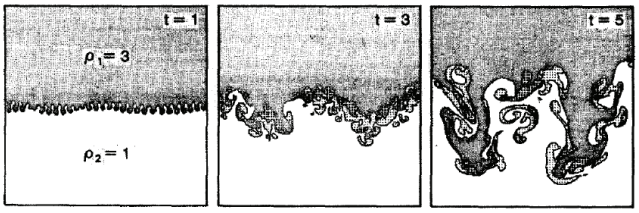

(b) Mode competetion

Figure 2.11: Multi-mode simulations of RTI showing the difference in late-time behavior due to mode coupling and mode competition [93].

2.3 Current Research of Rayleigh-Taylor Instability

Obtaining a detailed understanding of the growth of RTI has vast consequences in numerous technical applications, specifically those discussed in Section 2.1.1. For example, investigations into the effect that mixing has on the growth rate will give a better picture of what drives the flame front acceleration in type Ia supernovae, which is crucial for understanding dark energy and the fate of the universe. The shock waves created by RT unstable flame fronts is a possible detonation mechanism [60]. There has been other recent progress with compressible RTI, yet most of the focus is on incompressible systems. Investigations into the self-similar nature of the flow leave many questions unanswered. The dependence of the late-time behavior on the initial perturbations is not fully understood. Even if all memory of the initial conditions is lost, it is unknown if the flow truly ever reaches self-similarity. In addition, there is a discrepancy between experiments and computations when it comes to determining the self-similar growth factor α. Numerical simulations typically initialize the flow with a spectrum of short wavelength perturbations. The simulations rely on mode coupling to obtain larger structures that are independent of the initial conditions, thus making the growth universal. In experiments of RTI, the initial spectrum necessarily includes low wavenumber

perturbations, due to the broad nature of uncontrolled disturbances. Experiments are, at least partially, driven to self-similarity by mode competition [21, 23, 67]. The results from simple two-dimensional simulations are shown in Figure 2.11, which compares the late-time structures when mode coupling and mode competition drive the flow to self-similarity [93]. The mode coupling simulation has short wavelength perturbations only. The mode competition simulation has an additional long wavelength disturbance, which dominates the flow even to late-times. The current state-of-the-art numerical simulations and experiments of RT systems are discussed in the next sections.

2.3.1 Numerical Simulations of Rayleigh-Taylor Systems

Numerical experiments of RTI have proven to be an essential compliment to observations in nature and in the lab. Due to uncontrolled disturbances in every experimental apparatus, computational studies are necessary to calibrate or validate engineering models before they are applied to real problems [65]. Simulations of Rayleigh-Taylor systems have historically been crucial in resolving many previously unsettled issues, including dimensionality and Atwood number effects on the late-time growth of the bubble and spike structures [10, 92]. At the same time, many doors have been opened to new unexplained physics, especially regarding the self-similar growth. Most large simulations calculate α to be much lower than experimental results, but this may be a consequence of mode competition in the lab. Simulations use band-limited initial conditions, which is not possible in experiments. The difficulty for numerical simulations is the cost of resolving the dynamics on a large enough domain to avoid unwanted boundary effects. Performing direct numerical simulations (DNS), where all relevant scales of motion are resolved, on uniform grids puts a heavy restriction on the resolvable Reynolds number, even with the most powerful computers in the world. The requirement for self-similarity states that the Reynolds number must be high enough for the mixing to be insensitive to viscosity and diffusivity. Large-eddy simulations (LES), where the effect of subgrid-scale motions are modeled, also have difficulties since the nature of RTI involves small scale perturbations growing and merging into larger structures. LES models assume

a Kolmogorov energy spectrum, where the turbulent energy cascades from large to small scales. The advantage of LES comes from resolving only the large scale self-similar growth, which must occur at scales well above the initial perturbations based on the requirements in (2.80). Thus, the relatively coarse grid associated with LES methodology will not accurately capture the inverse cascade of the kinetic energy generated at the perturbation length scales. Furthermore, the efficacy of applying a Reynolds-averaged Navier-Stokes (RANS) approach, where all fluctuating quantities are modeled in order to solve for the mean flow, is unreliable since turbulent diffusion models must be modified to provide the quadratic self-similar growth. Simulations of RT systems most commonly apply DNS and LES methodologies. As computational resources continue to grow more powerful, the prospect for numerical simulations to drastically alter the human understanding of RTI becomes ever more influential and promising.

Attempting to accurately measure the universal self-similar growth factor for RT flows has been a pressing issue among scientists for decades. The common approach is to find a portion of the flow where h grows linearly with Agt^2. The slope is then assumed to be α. The first numerical simulations of RTI considered both two and three dimensional systems [5, 37, 93, 94, 95, 96]. The range of the growth factors was $0.03 < \alpha < 0.05$. Later simulations attempted to reduce the amount of numerical diffusion by utilizing front-tracking techniques, which gave $0.05 < \alpha < 0.08$ [2, 29, 31, 33, 35, 39, 48, 61]. Whereas these studies were unable to agree on a growth factor, the importance of initial conditions and late-time bubble entrainment on the mixing layer growth was made evident.

2.3.1.1 Incompressible Single-Mode Simulations

The growth stages for single-mode incompressible RTI have been studied in detail for the low Atwood number ($A = 0.04$) case [89]. When the viscous effects are small, the instability undergoes the following range of development stages: diffusion growth (DG), exponential growth (EG) consistent with linear stability theory, potential flow growth (PFG), reacceleration (RA), and chaotic development (CD). The evolution of the bubble velocity and height during all stages of the growth

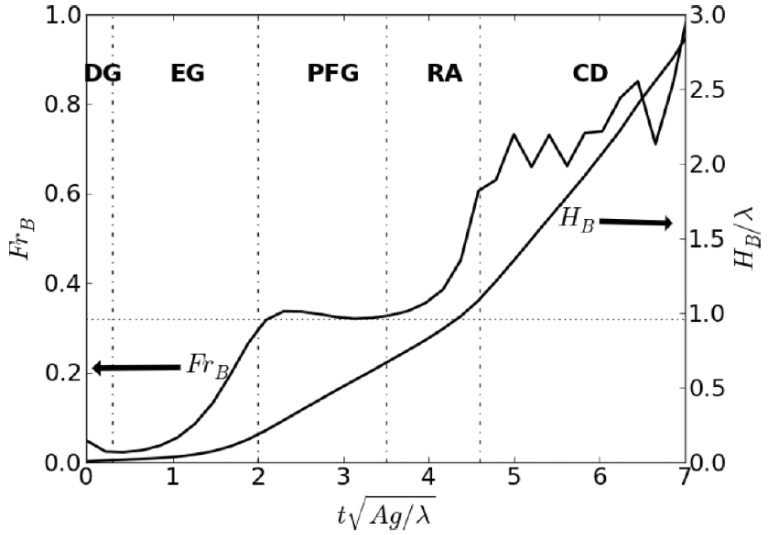

Figure 2.12: The stages of single-mode RTI, where Fr_B is a nondimensional measure of the instantaneous bubble velocity, and H_B is the bubble height [89].

of the instability are shown in Figure 2.12. During the early stages (DG, EG, and PFG), vorticity is generated but has negligible effect on the growth of the instability. During the RA stage, vortices appear near the centerline of the instability. The late-time growth of single-mode RTI, namely the CD stage, consists of random acceleration and deceleration phases due to complex vortical interactions and induced motion. These random variations act on a quadratically growing background state since the mean acceleration of the bubble is constant. This differs from the long-held belief that the late-time instability growth is characterized by a constant velocity, which is only accurate if the PFG stage extends to late-times. The growth coefficient, α, can be calculated from the late-time mean quadratic growth for the single-mode case and compared with the multi-mode self-similar growth factor.

The viscous and diffusion effects are quantified by introducing a perturbation Reynolds number,

$$Re_p = \sqrt{\frac{Ag\lambda^3}{(1+A)\nu^2}}, \tag{2.85}$$

with a Schmidt number held at unity. Whereas all growth stages occur at high Re_p, as the value is lowered, the later stages of the instability development are suppressed or eliminated outright.

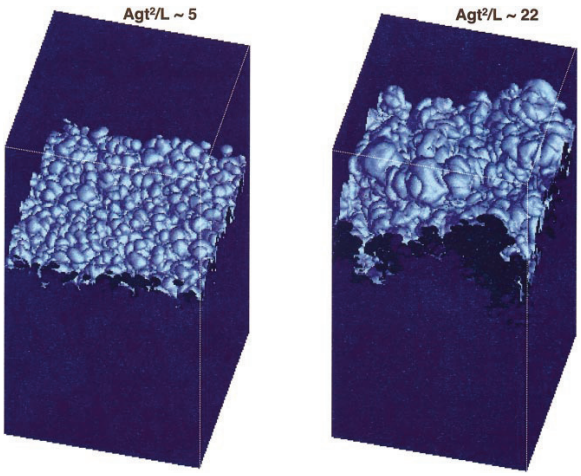

Figure 2.13: Isosurfaces of the heavy fluid mass fraction at two times showing the self-similar growth of the bubbles [25].

Furthermore, the nature of the early stages change with Re_p, such as the viscous effects of the linear growth rate during the EG stage, as discussed in Section 2.2.2. None of the early investigations of single-mode RTI have achieved the CD stage due to short development times or high viscous and diffusion effects.

2.3.1.2 The Alpha-Group Monotone-Integrated Large-Eddy Simulations

A recent collaboration, aptly called the Alpha-Group, consisting of five organizations (Atomic Weapons Establishment, University of Chicago, Lawrence Livermore National Laboratory, Texas A & M, and Sandia National Laboratory) and utilizing seven various numerical codes (TURMOIL3D, FLASH, WP/PPM, NAV/STK, RTI-3D, HYDRA, and ALEGRA) performed a series of RTI simulations in an attempt to improve the previous measures of the growth factor α [25]. The focus was on the mixing of miscible fluids (low Schmidt numbers) at high Reynolds numbers, such that there is significant dissipation within a Kolmogorov energy spectrum. The systems are driven to self-similarity by generating long wavelength bubbles through the mode coupling of multi-mode initial short wavelength perturbations, in order to make the growth independent of the initial conditions. Figure 2.13 shows isosurfaces of constant mass fraction for the heavy fluid ($Y_2 = 0.99$) at two times within the self-similar regime. The dominant bubble diameter increases proportionally

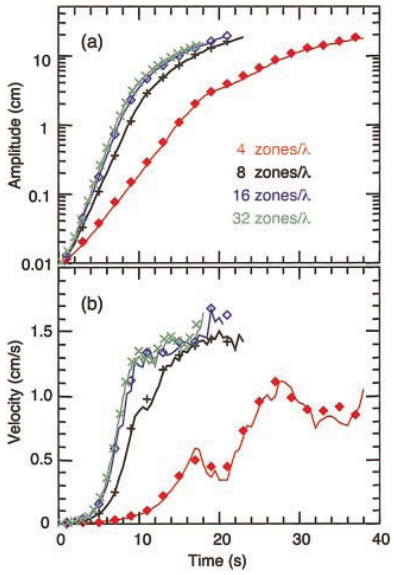

Figure 2.14: Convergence test for the bubble height and velocity, using the HYDRA code, with (lines) and without (symbols) interface reconstruction [25].

with the layer growth. All but one of the codes are compressible solvers run in the incompressible limit. Interface reconstruction is used to test the effect that mixing has on late-time entrainment due to the associated numerical diffusion. The simulations solve the Euler equations and rely on numerical diffusion to stabilize the problem, which reduces the reliability of the results. All of the codes are forms of monotone-integrated LES (MILES), which is a total variation diminishing LES approach [97]. MILES techniques are therefore able to handle the initial density discontinuity without introducing unphysical oscillations. Some of the codes use a Lagrangian advection phase that introduces enough dissipation in kinetic energy to make an explicit subgrid-scale model unnecessary. This is done at the expense of the trustworthiness of the findings, since the computations may misrepresent the dynamics of the flow.

Single-mode calculations are performed in order to compare the small amplitude exponential growth rates with the theoretical values from linear stability theory including viscous and diffusion effects. The effective numerical viscosity is inferred from the difference. At later times, the terminal bubble velocities are calculated and compared with the potential flow formulas. The bubble shape modifies the drag it experiences, which accounts for the variations found in the terminal velocities.

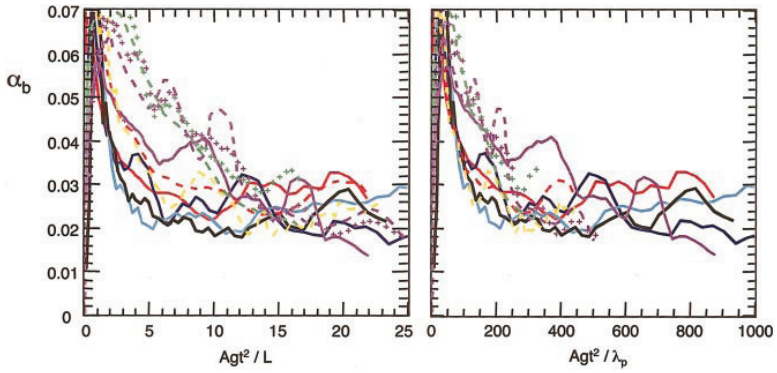

Figure 2.15: The evolution of the growth factor, α_b, is obtained by differentiating h_b with respect to Agt^2, and is plotted for two normalizations of time [25].

These differences have a direct relevance on the self-similar growth factor α. The bubble height and velocity for a sample single-mode case are shown in Figure 2.14. The observed linear growth rates are typically 80% or more of the values obtained from linear stability theory. The measured terminal velocities are found to be within 90% of that predicted by potential flow theory.

Results for the multi-mode simulations are displayed in Figure 2.15. The growth factor α is calculated by differentiating h with respect to Agt^2, which is normalized by the horizontal length of the domain, $L = L_h$, and the most unstable wavelength. The dotted lines are simulations on a $128 \times 128 \times 256$ grid, and the solid lines use a $256 \times 256 \times 512$ grid. When the most unbstable wavelength is used, all of the simulations enter the self-similar region when $Agt^2/\lambda_0 \approx 250$. The steady state growth factor is measured as $\alpha \approx 0.025$, which is about 40% lower than the average value obtained in experiments, $\alpha \approx 0.057$. The disparity is attributed to the absence of long wavelength initial perturbations in the simulations. Thus, the value obtained for α is the contribution from mode coupling and represents a lower bound for observations in the lab. The Alpha-Group also show that the simulations exhibit Kolmogorov power spectra with an inertial subrange above the dominant bubble wavelength, λ_b. The dissipation scale is proportional to the grid size, but the total amount of dissipation remains constant and proportional to the converted potential energy, which agrees with DNS results. Due to the introduction of numerical dissipation, the effects of fine scale mixing and entrainment on the simulations are unknown. The use of DNS to fully resolve

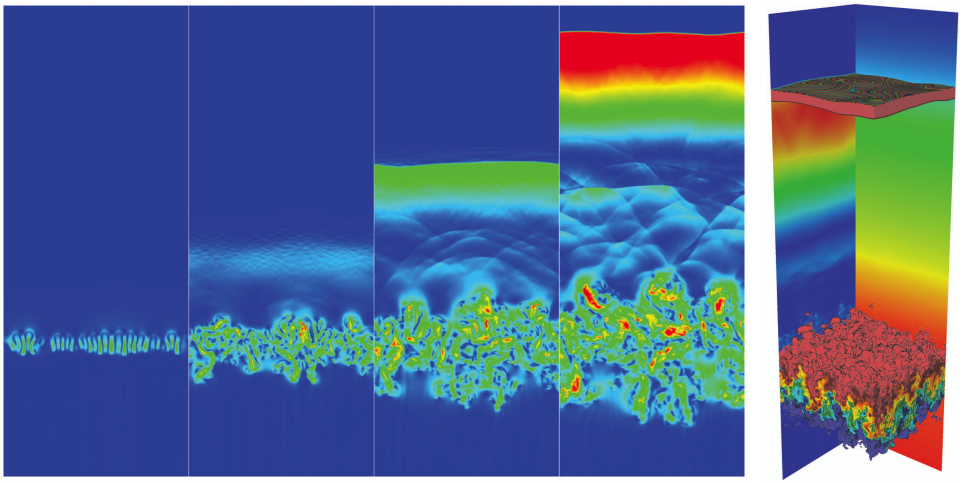

(a) 2D (b) 3D

Figure 2.16: The two and three dimensional LES of a highly compressible RTI system, which show the presence of a shock wave launched from the unstable interface into the upper fluid [60].

RTI may extend the progress achieved by the Alpha-Group.

2.3.1.3 Rayleigh-Taylor Shock Waves

The majority of simulations and experiments of RTI have been performed in the incompressible limit at low Mach numbers. Little is known about the effects of compressibility and hydrostatic density gradients on the late-time growth of RTI and the development of RT turbulence. The only numerical study to date that focuses on the compressive nature of RTI has discovered the presence of RT shock waves [60]. The results from both a two and three dimensional LES for a system with high compressibility effects are shown in Figure 2.16. The images show that the rising bubbles act like pistons, compressing the heavy fluid above the interface, which generates shocklets. The shocklets are continuously generated on the bubble side of the interface, propagate into the upper fluid, and coalesce into a strong shock wave. The simulations discredit the idea that RTI is solely an incompressible phenomenon since RT shock waves could play an important role in the flame front acceleration of type Ia supernovae.

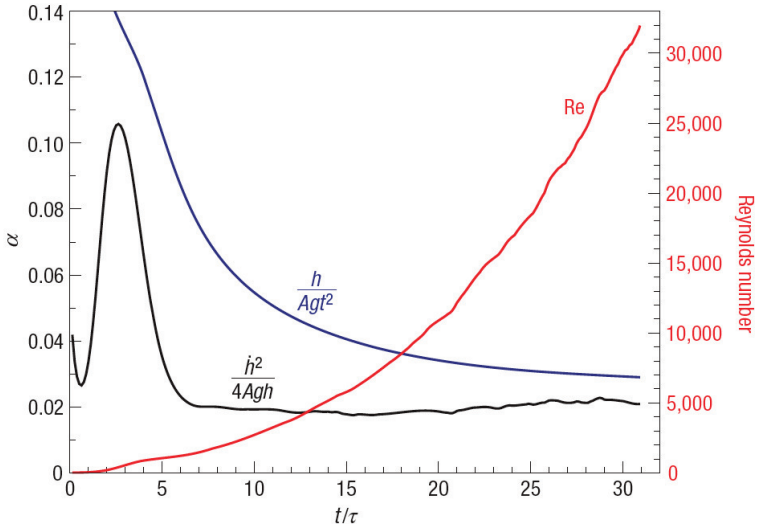

Figure 2.17: A comparison of the two formulas for α [9].

2.3.1.4 State-of-the-Art Direct Numerical Simulations

Cabot and Cook recently ran the largest, at that time, numerical simulation of RTI, and the findings have the potential to drastically alter flame propagation models for type Ia supernovae [9]. A direct numerical simulation was performed on a $3,072^3$ grid, which ran on one of the fastest computers in the world for two weeks. The system included two incompressible miscible fluids with $A = 0.5$. A plot of the mixing layer at the end of the simulation is shown in Figure 2.9. The simulation acheived Reynolds numbers that far exceed any previous computation of the instability. The simulation achieved $Re = 32,000$, well above the requirement $Re > 10^4$ for turbulent flows to reach an asymptotic state [26]. The definition of the bulk Reynolds number is

$$Re \equiv \frac{H\dot{H}}{\nu}, \tag{2.86}$$

where H is the visual layer width, defined as the range in the vertical direction for which $0.01 \leq \langle X \rangle \leq 0.99$ and $\langle X \rangle$ is the horizontal planar average of the molar mass fraction. With such a large computational domain, all of the requirements for self-similarity in (2.80) are easily satisfied even to late-times. A comparison of the two methods for measuring the growth factor α, given in relationships (2.77) and (2.82), explains why previous simulations, including the Alpha-Group's efforts,

gave a decreasing α as the resolution and Re are increased. As shown in Figure 2.17, the original model for the growth factor, which does not include the linear growth term for the mixing layer width, gives a decreasing value for α with time and Re. The improved formula gives a nearly constant $\alpha \approx 0.02$ at moderate Re. Thus, self-similar predictions are valid after $t/\tau \approx 6$, where

$$\tau = \left(\frac{\lambda_0}{Ag}\right) \tag{2.87}$$

is the RTI timescale. Even though the lower order terms in the self-similar relations should become negligible at very late times, these terms remain important throughout the simulation. It was discovered that the ratio of kinetic energy to released potential energy has a weak Reynolds number dependence, instead of remaining constant as previously thought. This is evident as a slight increase in α at higher Re. A further analysis of the results from this very large simulation have shown that the typical turbulent eddy viscosity, $\nu_t \sim k_t^2/\varepsilon$, is unable to capture the turbulent transport in the flow. The model breaks down due the the buoyancy production and its effects on the energy spectrum [56].

An even larger RTI direct numerical simulation has been performed by Livescu, Petersen, Martin, and McCormick. The simulation is performed using a $4096^2 \times 2304$ grid with $A = 0.75$. The results have not been published, but an image was kindly offered for presentation in Figure 2.8.

2.3.1.5 Classical Adaptive Mesh Refinement Methods

Solving the Rayleigh-Taylor problem on an adaptive mesh is a promising approach since the small scale structures remain localized near the interface. Using a full structured grid wastes a large amount of computational resources, since most of the domain is quiescent, especially at early-times. Some of the codes in the Alpha-Group, such as FLASH, use an adaptive mesh refinement (AMR) tool, called PARAMESH, to set the local resolution of the simulation [8]. In classical AMR, the refinement criteria may be user-specified. For example, the user may require that the mass in any given cell remains constant, up to a specified threshold. Thus, the grid is adapted based on the

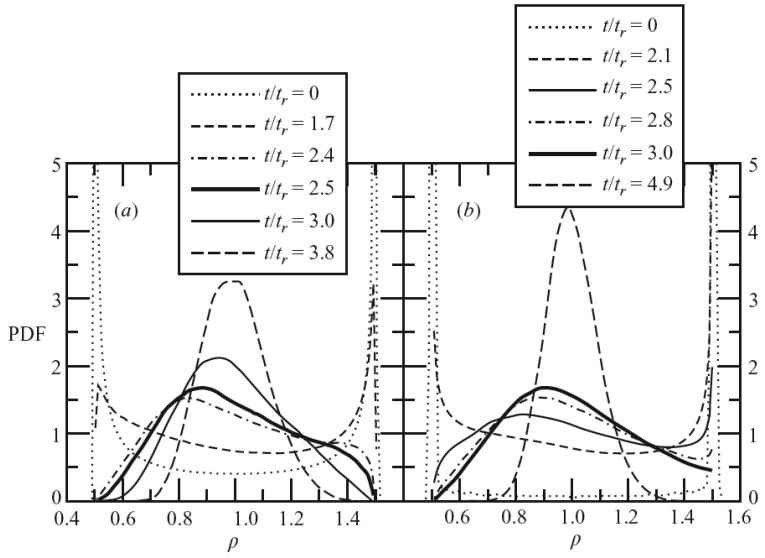

Figure 2.18: The evolution of the density PDF for a homogeneous RT system at $A = 0.5$ and two different resolutions: (a) 256^3 and (b) 512^3 [55].

density distribution, and the method has no control on the error due to grid adaptation. The refinement criteria may also be set based on an approximation of the local truncation error. One common method uses Richardson extrapolation, which estimates the truncation error by comparing the solutions using various temporal and spatial step sizes. The grid is locally refined where the approximated error is above a specified threshold. Whereas classical AMR techniques are successfully used to solve RTI on structured and unstructured grids, increased data compression rates in smooth regions of the solution can be achieved using adaptive multiresolution methods, one of which is discussed in Section 2.4.1. Additionally, adaptive multiresolution methods have a direct control of the grid adaptation error, without the extra computations required in AMR methodology.

2.3.1.6 Homogeneous Rayleigh-Taylor Simulations

Interest in VD flows is driven by the need to obtain a thorough understanding of the turbulent mixing processes between fluids of different densities, such that accurate models can be applied to technical problems. Of crucial importance is obtaining a model for RT mixing and the ensuing tran-

sition to turbulence, which has been investigated through numerical simulations of homogeneous RT systems. Early studies of buoyancy-driven turbulence applied the Boussinesq approximation, where the densities of the species are assumed similar, such that variations of density only affect the conservation of momentum through the buoyancy force [7]. For true VD flows, where the density differences can be large, the mixing dynamics have been explored through statistical analysis of the hydrodynamics [76, 77], the fluctuating velocity field [16, 54, 75], and the scalar field [55].

The largest simulation of a homogeneous RT system was performed on a 1024^3 grid [54, 55]. The study initialized random blobs of pure incompressible fluids within a triply periodic domain. The initial probability density function (PDF) for density is equally peaked at the two pure fluids, such that the heavy and light fluid are equally prevalent throughout the domain. Thus, density is initialized as a double-delta PDF. The fluids are subjected to buoyancy-driven turbulence as the two fluids move in opposite directions. The fluids eventually mix due to molecular diffusion and the turbulence dies out. The study investigated parameters in the ranges of $250 \leq Re \leq 1667$, $0.05 \leq A \leq 0.5$, and grid resolutions from 256^3 to 1024^3. For high Atwood numbers, the heavy fluid is found to experience less stirring and molecular mixing than the light fluid. This effect is evident in the density PDF evolution in Figure 2.18. The PDF is skewed toward the heavy fluid as mixing occurs, eventually leading to an approximately Gaussian distribution. Therefore, the light fluid mixes faster than the heavy fluid. This result is crucial for obtaining an appropriate model for the mixing layer in RTI, since different amounts of molecular mixing occur on the two sides of the layer, which could explain why the spikes have higher growth rates than the bubbles.

Another numerical study of a homogeneous RT system attempts to simulate statistically stationary buoyancy-driven turbulent mixing [14]. The simulation has fringe regions at the top and bottom of the domain, which supplies the flow with unmixed fluids. The domain is triply periodic with gravity applied as normal. The injected fluid is always pure and contributes to an unstable configuration, such that heavy fluid is injected from the top and light fluid from the bottom. Within each fringe region, the injected fluid is introduced at the exact same mass rate as the fluid that is removed from that layer such that the conservation laws remain satisfied. DNS are performed

for parameters in the ranges of $260 \leq Re \leq 478$, $0.5 \leq A \leq 0.75$, and grid resolutions from 256^3 to $384^2 \times 768$. In addition, LES are used to test a mixing model. The parameters for LES are $Re = 478$, $A = 0.5$, and grid resolutions from $32^2 \times 64$ to $384^2 \times 768$.

2.3.2 Experiments of Rayleigh-Taylor Instability

Despite the difficulties presented to the experimentalist trying to study Raleigh-Taylor instability, great amounts of ingenuity have led to the development of numerous disparate ways of creating instability in the lab. Many experiments have proven to be repeatable and successful for the validation of mixing layer growth models. Obtaining a reliable approximation of the growth factor α has been an important but difficult task, since the applicability of equation (2.82) breaks down if the criteria in (2.80) are not met. Not only are the initial perturbations impossible to fully characterize in the lab, but also the finite domains of the experimental setup often lead to unwanted influence of the boundaries deep into the flow, polluting the natural growth of the instability. These difficulties have spurred the use of inventive techniques in the lab, which have proven useful for comparison with numerical simulations.

Self-similar analysis must be applied with caution to experimental data. Most experiments measure a growth factor in the wide range $0.03 < \alpha < 0.08$. One strategy is to accelerate a tank of stable fluids, with the light fluid above the heavy fluid, downward, overcoming the gravitational acceleration. The "rocket rig" experiment achieved an acceleration of $30g$ and measured $\alpha \approx 0.063$ for a variety of immiscible fluids at various Atwood numbers [70, 94]. A different study used the Linear Electric Motor to achieve accelerations greater than $100g$, which gave $\alpha \approx 0.05$, independent of A [21, 22, 24]. When the surface tension is increased by a factor of 50 in an attempt to reduce the effect of late-time bubble entrainment, the growth factor increases to $\alpha \approx 0.06$. Another technique involves overturning a tank that is initially stable, light over heavy. One such experiment found $\alpha \approx 0.07$ for small Atwood number systems [4]. Systems in the lab often begin with an unstable configuration (heavy fluid lying on top of the light fluid), where a separating plate or membrane is withdrawn carefully [17]. In one case, a membrane is ruptured using electronics, which gives

$\alpha \approx 0.063$ for $A = 0.5$ and $A = 0.9$ [45]. Other experiments use magnetic fields to levitate heavy ferrofluids, which become polarized in the presence of a magnetic field, above light fluids that are not paramagnetic [40, 62]. Another idea replaces the time evolution of the instability with the spatial progression of two fluids (heavy over light) flowing past a splitter plate with equivalent velocities [59, 64]. The variations in growth factors among experiments and in comparison with simulations prove that the mixing layer growth is heavily dependent upon initial conditions and late-time bubble entrainment.

2.4 Numerical Tools

Large computational domains are necessary for performing simulations of RTI to late times. Conversely, near the interface, small grid spacings are required for high Reynolds number flows. Due to the nature of RTI, a wide range of scales needs to be resolved in order to perform accurate computations. One promising approach to this issue is the use of an adaptive method, where the resolution of the computational grid matches the local scale of the flow dynamics. The Parallel Adaptive Wavelet Collocation Method naturally adapts the mesh to moving structures in the flow, while retaining a direct control on the error. The top and bottom boundaries must be treated carefully in compressible RT flows, since acoustic waves are generated at the interface. The initial instability and resulting turbulent mixing are heavily sensitive to acoustic waves. In order to isolate the instability, the boundaries of the numerical domain must minimize wave reflections. Typical wall conditions are not sufficient for the RTI case. Using a characteristic-based representation of the flow near the boundaries allows for the application of slip walls and non-reflecting inflow and outflow boundary conditions.

2.4.1 Parallel Adaptive Wavelet Collocation Method

The Parallel Adaptive Wavelet Collocation Method (PAWCM) is an adaptive multiresolution method, which utilizes wavelets to locally adapt the numerical resolution during the evolution of complex flows [84, 85, 86]. Thus, localized structures are well-resolved while optimizing the use

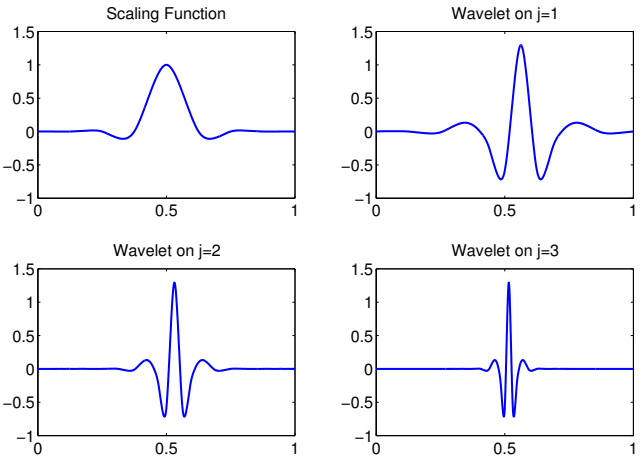

Figure 2.19: Since scaling and wavelet interpolating functions are localized, they provide information about the dynamics of a system at the local scale and position. The wavelets are shown for various levels of resolution, j.

of computational resources. Unlike classical AMR techniques, PAWCM has the advantage of a threshold parameter that directly controls the error associated with the grid adaptation [79]. In order to simplify the computation of nonlinear terms, a wavelet collocation method is used, which ensures a one-to-one correspondence between grid points and wavelets.

PAWCM uses a wavelet representation of flow variables to dynamically adapt the grid to the local scale of structures within the flow. Wavelets are functions that are localized in both wavenumber and physical space, which are used as a set of basis functions to represent the flow in terms of wavelet coefficients. In this sense, wavelets provide both frequency and position information about the flow. An array of wavelet interpolating functions at varying levels of resolution and a scaling function are shown in Figure 2.19. PAWCM uses wavelet decomposition to determine those wavelets that are insignificant for representing the solution while maintaining a direct error control. Once scaling functions, $\phi^j_{\mathbf{k}}(\mathbf{x})$, and wavelet interpolating functions, $\psi^{\mu,j}_{\mathbf{l}}(\mathbf{x})$, are constructed [84], a function $u(\mathbf{x})$ can be decomposed as

$$u(\mathbf{x}) = \sum_{\mathbf{k}} c^0_{\mathbf{k}} \phi^0_{\mathbf{k}}(\mathbf{x}) + \sum_{j=0}^{+\infty} \sum_{\mu=1}^{2^n-1} \sum_{\mathbf{l}} d^{\mu,j}_{\mathbf{l}} \psi^{\mu,j}_{\mathbf{l}}(\mathbf{x}). \tag{2.88}$$

A wavelet coefficient, $d^{\mu,j}_{\mathbf{l}}$, will have a small value unless the function varies significantly on the

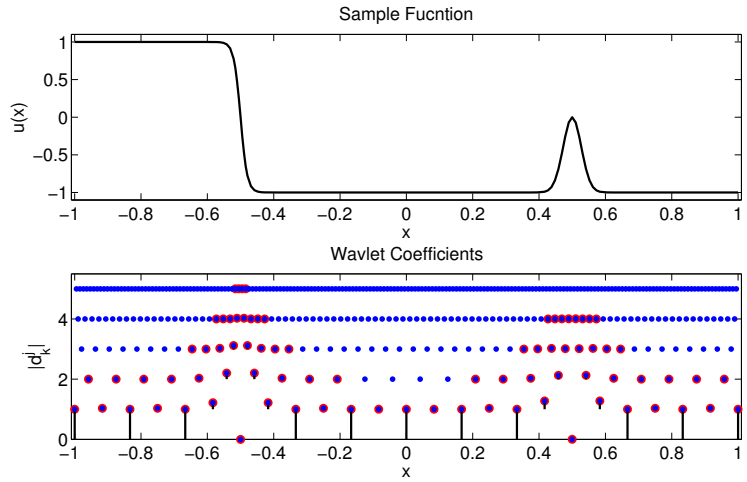

Figure 2.20: The wavelet decomposition of a one-dimensional function with two regions of sharp transition. The grid is displayed by level of resolution. The points circled in red are deemed significant since their wavelet coefficients have values above the threshold.

scale j in the immediate vicinity of the wavelet $\psi_{\mathbf{l}}^{\mu,j}(\mathbf{x})$. Figure 2.20 shows a sample function with two regions of sharp transition that is decomposed into its wavelet coefficients. The complete grid is given in blue, displayed at various levels of resolution, j, along the y-axis. The relative magnitude of the wavelet coefficients at each location is given by the black stems. For fields with isolated structures on a large-scale quiescent background, most of the wavelet coefficients are small. The wavelets associated with coefficients less than a prescribed threshold parameter, ϵ, can be discarded in representing the solution, while retaining an approximation with an error that is $O(\epsilon)$. Thus, wavelets are deemed significant if $|d_k^j| \geq \epsilon \|u\|$. The significant wavelets are shown in red, since their scaled coefficients are greater than the prescribed threshold $\epsilon = 10^{-2}$. Since the grid adapts to localized structures, high resolution is required only in the locations where the small-scale structures exist. A small percentage of the full nonadaptive grid points are needed to represent the function accurately, due to the coarse grid where the function remains constant.

To obtain the error associated with using a wavelet-based adaptive approximation for a function, the wavelet representation given in (2.88) can be split into wavelets whose coefficients are

above and below the threshold parameter ϵ,

$$u(\mathbf{x}) = u_{\geq}(\mathbf{x}) + u_{<}(\mathbf{x}), \tag{2.89}$$

where

$$u_{\geq}(\mathbf{x}) = \sum_{\mathbf{k}} c^0_{\mathbf{k}} \phi^0_{\mathbf{k}}(\mathbf{x}) + \sum_{j=0}^{+\infty} \sum_{\mu=1}^{2^n-1} \sum_{\substack{\mathbf{l} \\ |d^{\mu,j}_{\mathbf{l}}| \geq \epsilon \|u\|}} d^{\mu,j}_{\mathbf{l}} \psi^{\mu,j}_{\mathbf{l}}(\mathbf{x}), \tag{2.90}$$

$$u_{<}(\mathbf{x}) = \sum_{j=0}^{+\infty} \sum_{\mu=1}^{2^n-1} \sum_{\substack{\mathbf{l} \\ |d^{\mu,j}_{\mathbf{l}}| < \epsilon \|u\|}} d^{\mu,j}_{\mathbf{l}} \psi^{\mu,j}_{\mathbf{l}}(\mathbf{x}), . \tag{2.91}$$

The representation of a sufficiently smooth function by only the significant wavelets has an error that is bounded as

$$\|u(\mathbf{x}) - u_{\geq}(\mathbf{x})\| \leq C_1 \epsilon \|u\|, \tag{2.92}$$

where C_1 is a constant. The number of significant wavelets, $\mathcal{N}$, required for the representation is bounded as

$$\mathcal{N}^{1/n} \leq C_2 \epsilon^{-1/p}, \tag{2.93}$$

where n is the dimension of the problem, $p-1$ is the order of the wavelet interpolation, and C_2 is a constant. The error bound in terms on the number of significant wavelets is therefore

$$\|u(\mathbf{x}) - u_{\geq}(\mathbf{x})\| \leq C_3 \mathcal{N}^{-p/n} \|u\|, \tag{2.94}$$

where C_3 is a constant. Derivatives are calculated at the corresponding local resolution using finite differences. Second-generation wavelets are used, which allow the order of the wavelets, and, thus, the order of the finite differences, to be easily varied [81].

When solving evolution problems, such as the growth of RTI, an adjacent zone is added to the points associated with wavelets whose coefficients are significant. By adding the nearest neighbors of the significant wavelet coefficients in both position and scale, the computational grid contains points that could become significant during a time advancement step. A reconstruction check is also performed, ensuring that all the points required to perform the wavelet transforms are

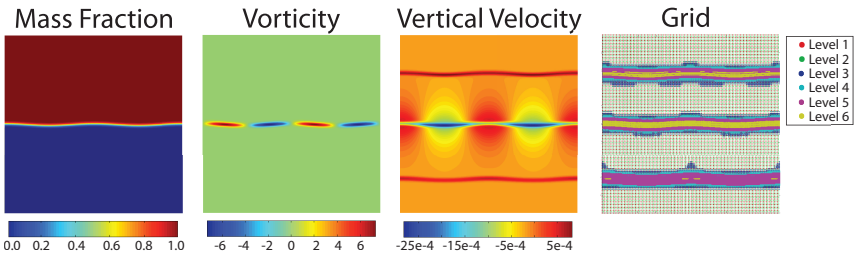

Figure 2.21: Mass fraction, vorticity, vertical velocity, and the associated adaptive grid for the early-time exponential growth, consistent with linear stability theory. The images result from the direct numerical simulations presented in Chapter 4.

included on the mesh. When spatial derivatives are taken, ghost points are also added to the grid to maintain the desired order of the method. The additional computational cost per grid point of PAWCM is currently three to five times greater than a standard non-adaptive method. The extra cost per grid point is negated in systems where small-scale structures occur in a small fraction of the domain. Applying PAWCM to simulations of RTI is a prime example where the compression of the grid is very high, since the mixing layer remains localized well into the nonlinear growth stage. Also, since a small percentage of the grid points are necessary to achieve high effective global resolutions, memory resources are used efficiently. The dynamic grid adaptation allows the efficient use of computational resources to resolve a wide range of scale structures as they evolve.

A typical dynamically adapted grid is shown in Figure 2.21 for a RTI simulation during the early-time exponential growth regime. Acoustic waves are created at the interface from the initial perturbations. PAWCM dynamically adapts to the waves as they propagate away from the interface. The effective global resolution is 10241×1024, yet only 1.9% of the points are used ($199,593$ points, 98.1% compression). Even at late-times, when the mixing layer has filled the majority of the domain, PAWCM is able to compress the data by 96.4%, as shown in Figure 2.22. Only $380,166$ points, 3.6% of the non-adaptive grid, are required to represent the flow.

The largest challenge in parallelizing PAWCM lies in applying an effective load balancing procedure. Due to the dynamically adapting grid, using a geometric decomposition of the domain will inevitably lead to overloaded processors that act as a bottleneck for the entire simulation.

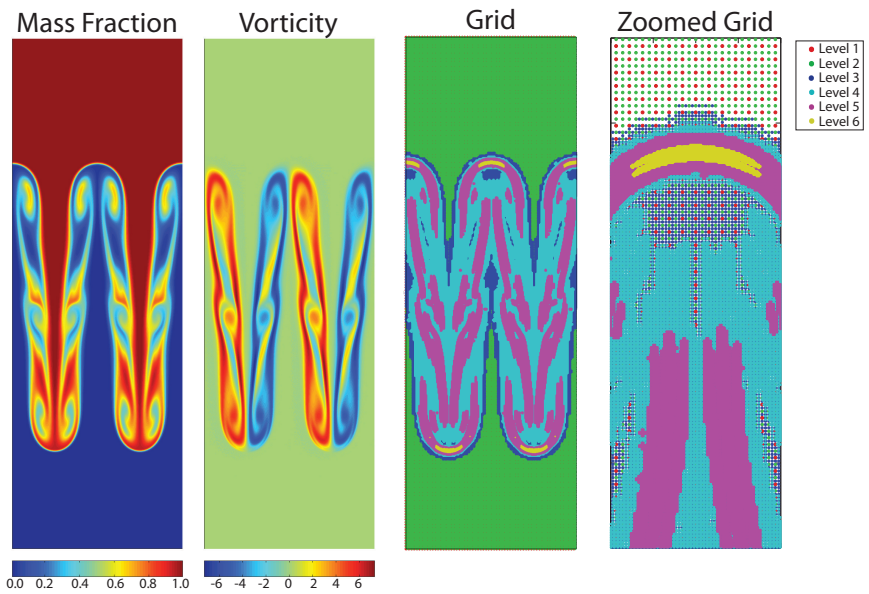

Figure 2.22: Mass fraction, vorticity, and the associated adaptive grid for the late-time instability growth. The images result from the direct numerical simulations presented in Chapter 4.

The data are stored using a tree-like structure with tree roots starting at a sufficiently large level of resolution to shorten the tree traversing path and to minimize the size of the trees for data migration. Both static and dynamic domain partitioning approaches have been developed. For dynamic domain partitioning, the trees are considered to be the minimum quantum of data to be migrated between the processors. This allows for the efficient and fully automated handling of a non-simply connected partitioning of a computational domain. Dynamic load balancing is achieved through domain repartitioning during the grid adaptation step by reassigning trees to the appropriate processors to ensure approximately the same number of nodes on each processor.

Dynamical load balancing is performed using the Zoltan library, which can refine or repartition the domain once a specified imbalance threshold is met. For PAWCM, the system is deemed imbalanced once $\min_p(N_{wlt_p})/\max_p(N_{wlt_p})$ falls beneath a given threshold parameter, where N_{wlt_p} is the number of active wavelets on the p^{th} processor. The dynamical load balancing procedures using the Zoltan library can easily handle non-simply connected domains. Sample domain decompositions for the solution of RTI and the associated adaptive grid in Figure 2.22 are shown in

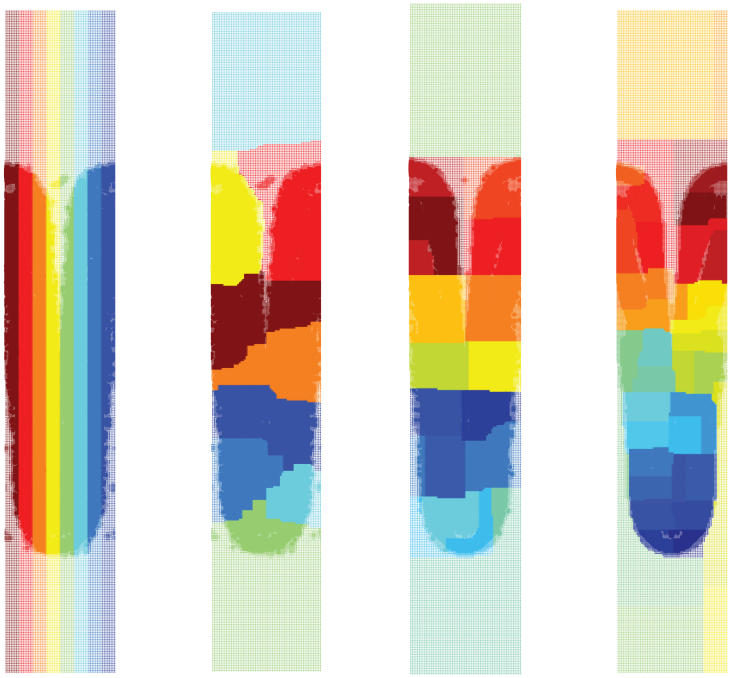

(a) Geom. 8 (b) Zol. 8 (c) Zol. 16 (d) Zol. 32

Figure 2.23: Domain decompositions associated with the solution and grid in Figure 2.22. The decomposition type and processor number are specified, where 'Geom.' signifies geometrical decomposition, and 'Zol.' represents use of load balancing through the application of the Zoltan library. The images result from the direct numerical simulations presented in Chapter 4.

Figure 2.23. The geometric decomposition for eight processors uses vertical strips, which leads to overloaded processors at late times. The domain decomposition using the Zoltan partitioning for eight, sixteen, and thirty-two processors are also presented.

2.4.2 Characteristics-Based Boundary Conditions

Simulations of systems lacking periodicity often require creative approaches near the computational boundaries in order to maintain high-order approximations and stability in the solution. Simulations of compressible flows require an accurate control of wave reflections at the boundaries. It is also often desirable to remove waves at the boundaries. Poinsot and Lele developed a set of Navier-Stokes Characteristic Boundary Conditions (NSCBC) by analyzing the characteristic lines crossing the boundaries for the associated hyperbolic system, namely the Euler equations [63]. By considering the well-posedness of the Navier-Stokes equations, the method is extended

to the full system of equations, including viscous terms. Thus, the propagation of waves from the Navier-Stokes equations are assumed to be associated only with the hyperbolic part. Since most simulations are performed for high Reynolds numbers, the approximation is well justified. A distinction is made between a physical boundary condition, one in which the condition specifies a known physical behavior, and a soft boundary condition, which is required by the numerical method without being an explicit physical attribute. The number of physical boundary conditions required for the well-posedness of the Navier-Stokes equations depends on the nature of the flow, whether subsonic or supersonic, and the type of boundary, such as a wall, inflow, or outflow. The proposed numerical implementation requires additional soft boundary conditions for the associated flow type to keep the system well-posed.

The full system of equations governing the flow of compressible viscous fluids of N_s species is

$$\frac{\partial \rho}{\partial t} + \frac{\partial \rho u_j}{\partial x_j} = 0, \tag{2.95}$$

$$\frac{\partial \rho u_i}{\partial t} + \frac{\partial \rho u_i u_j}{\partial x_j} = -\frac{\partial p}{\partial x_i} - \rho g_i + \frac{\partial \tau_{ij}}{\partial x_j}, \tag{2.96}$$

$$\begin{aligned} \frac{\partial \rho e}{\partial t} + \frac{\partial \rho e u_j}{\partial x_j} &= -\frac{\partial p u_i}{\partial x_i} - \rho u_i g_i + \frac{\partial \tau_{ij} u_i}{\partial x_j} \\ &\quad - \frac{\partial q_j}{\partial x_j} + \frac{\partial c_{p_l} T s_{jl}}{\partial x_j}, \end{aligned} \tag{2.97}$$

$$\frac{\partial \rho Y_l}{\partial t} + \frac{\partial \rho Y_l u_j}{\partial x_j} = \frac{\partial s_{jl}}{\partial x_j}, \tag{2.98}$$

where $l = 1, 2, ..., N_s$, the heat flux is defined as

$$q_j = -k \frac{\partial T}{\partial x_j}, \tag{2.99}$$

the viscous stress, assuming Newtonian fluids, is defined as

$$\tau_{ij} = \mu \left(\frac{\partial u_i}{\partial x_j} + \frac{\partial u_j}{\partial x_i} - \frac{2}{3} \frac{\partial u_k}{\partial x_k} \delta_{ij} \right), \tag{2.100}$$

and the species flux is defined as

$$s_{jl} = \rho D \frac{\partial Y_l}{\partial x_j}. \tag{2.101}$$

The remaining definitions from the equations (2.3)-(2.6) are also used here.

Characteristic analysis is employed on the hyperbolic terms corresponding to waves propagating in the x_1 direction [83]. For waves that are approximately planar, traveling parallel to the x_1-axis, the analysis is simplified by considering the one-dimensional Euler equations,

$$\frac{\partial \rho}{\partial t} + \rho \frac{\partial u_1}{\partial x_1} + u_1 \frac{\partial \rho}{\partial x_1} = 0, \tag{2.102}$$

$$\frac{\partial u_1}{\partial t} + u_1 \frac{\partial u_1}{\partial x_1} + \frac{1}{\rho} \frac{\partial p}{\partial x_1} = 0, \tag{2.103}$$

$$\frac{\partial p}{\partial t} + \rho c^2 \frac{\partial u_1}{\partial x_1} + u_1 \frac{\partial p}{\partial x_1} = 0, \tag{2.104}$$

where $c = \sqrt{\gamma p/\rho}$ is the speed of sound. The system can be recast in terms of the differential characteristic variables,

$$\delta v_1 = \rho c \, \delta u_1 - \delta p, \tag{2.105}$$

$$\delta v_2 = c^2 \, \delta \rho - \delta p, \tag{2.106}$$

$$\delta v_3 = \rho c \, \delta u_1 + \delta p, \tag{2.107}$$

which results with the following characteristic equations,

$$\frac{\partial v_1}{\partial t} + (u_1 - c) \frac{\partial v_1}{\partial x} = 0, \tag{2.108}$$

$$\frac{\partial v_2}{\partial t} + u_1 \frac{\partial v_2}{\partial x} = 0, \tag{2.109}$$

$$\frac{\partial v_3}{\partial t} + (u_1 + c) \frac{\partial v_3}{\partial x} = 0. \tag{2.110}$$

These equations are all of the form

$$\frac{\partial v_\kappa}{\partial t} + \lambda_\kappa \frac{\partial v_\kappa}{\partial x_1} = 0, \tag{2.111}$$

which is replaced with

$$\frac{\partial v_\kappa}{\partial t} + \mathcal{I}_\kappa = 0. \tag{2.112}$$

Thus, the time variation of the characteristic wave amplitudes are given by

$$\mathcal{I}_1 = \lambda_1 \left(\frac{\partial p}{\partial x_1} - \rho c \frac{\partial u_1}{\partial x_1} \right), \tag{2.113}$$

$$\mathcal{I}_2 = \lambda_2 \left(c^2 \frac{\partial \rho}{\partial x_1} - \frac{\partial p}{\partial x_1} \right), \tag{2.114}$$

$$\mathcal{I}_3 = \lambda_3 \left(\frac{\partial p}{\partial x_1} + \rho c \frac{\partial u_1}{\partial x_1} \right), \tag{2.115}$$

with characteristic velocities

$$\lambda_1 = u_1 - c, \tag{2.116}$$

$$\lambda_2 = u_1, \tag{2.117}$$

$$\lambda_3 = u_1 + c. \tag{2.118}$$

The primitive variables can now be written in terms of the amplitude variations of the characteristic waves as

$$\frac{\partial \rho}{\partial t} + \frac{1}{2c^2}(\mathcal{I}_3 + \mathcal{I}_1 + 2\mathcal{I}_2) = 0, \tag{2.119}$$

$$\frac{\partial u_1}{\partial t} + \frac{1}{2\rho c}(\mathcal{I}_3 - \mathcal{I}_1) = 0, \tag{2.120}$$

$$\frac{\partial p}{\partial t} + \frac{1}{2}(\mathcal{I}_3 + \mathcal{I}_1) = 0. \tag{2.121}$$

The Local One-Dimensional Invsicid (LODI) relations use the above characteristic analysis of the one-dimensional inviscid problem to infer values for the wave amplitude variations in a multidimensional viscous system. Extending the analysis for a d-dimensional velocity field, where $d = 2$ or $d = 3$, and species transfer, the LODI relations are

$$\frac{\partial \rho}{\partial t} + \frac{1}{2c^2}(\mathcal{I}_{N_v} + \mathcal{I}_1 + 2\mathcal{I}_2) = 0, \tag{2.122}$$

$$\frac{\partial u_1}{\partial t} + \frac{1}{2\rho c}(\mathcal{I}_{N_v} - \mathcal{I}_1) = 0, \tag{2.123}$$

$$\frac{\partial u_{(2:d)}}{\partial t} + \mathcal{I}_{(3:d+1)} = 0, \tag{2.124}$$

$$\frac{\partial p}{\partial t} + \frac{1}{2}(\mathcal{I}_{N_v} + \mathcal{I}_1) = 0, \tag{2.125}$$

$$\frac{\partial Y_{(1:N_s)}}{\partial t} + \mathcal{I}_{(d+2:N_s+d+1)} = 0, \tag{2.126}$$

where $N_v = N_s + d + 2$ is the total number of evolved variables in the system, and the amplitude variation of the characteristic waves are

$$\mathcal{I}_1 = \lambda_1 \left(\frac{\partial p}{\partial x_1} - \rho c \frac{\partial u}{\partial x_1} \right), \tag{2.127}$$

$$\mathcal{I}_2 = \lambda_2 \left(c^2 \frac{\partial \rho}{\partial x_1} - \frac{\partial p}{\partial x_1} \right), \tag{2.128}$$

$$\mathcal{I}_{(3:d+1)} = \lambda_{(3:d+1)} \frac{\partial u_{2:d}}{\partial x_1}, \tag{2.129}$$

$$\mathcal{I}_{(d+2:N_s+d+1)} = \lambda_{(d+2:N_s+d+1)} \frac{\partial Y_{1:N_s}}{\partial x_1}, \tag{2.130}$$

$$\mathcal{I}_{N_v} = \lambda_{N_v} \left(\frac{\partial p}{\partial x_1} + \rho c \frac{\partial u}{\partial x_1} \right). \tag{2.131}$$

The associated characteristic velocities are

$$\lambda_1 = u_1 - c, \tag{2.132}$$

$$\lambda_2 = \lambda_{(3:d+1)} = \lambda_{(d+2:N_s+d+1)} = u_1, \tag{2.133}$$

$$\lambda_{N_v} = u_1 + c. \tag{2.134}$$

The characteristic waves are grouped for convenience, with their true definitions in brackets, as

$$\mathcal{X}_1 = \frac{1}{2c^2}(\mathcal{I}_{N_v} + \mathcal{I}_1 + 2\mathcal{I}_2) \left[= u_1 \frac{\partial \rho}{\partial x_1} + \rho \frac{\partial u_1}{\partial x_1} \right], \tag{2.135}$$

$$\mathcal{X}_2 = \frac{1}{2\rho c}(\mathcal{I}_{N_v} - \mathcal{I}_1) \left[= u_1 \frac{\partial u_1}{\partial x_1} + \frac{1}{\rho} \frac{\partial p}{\partial x_1} \right], \tag{2.136}$$

$$\mathcal{X}_{(3:d+1)} = \mathcal{I}_{(3:d+1)} \left[= u_1 \frac{\partial u_{(2:d)}}{\partial x_1} \right], \tag{2.137}$$

$$\mathcal{X}_{(d+2:N_s+d+1)} = \mathcal{I}_{(d+2:N_s+d+1)} \left[= u_1 \frac{\partial Y_{(1:N_s)}}{\partial x_1} \right], \tag{2.138}$$

$$\mathcal{X}_{N_v} = \frac{1}{2}(\mathcal{I}_{N_v} + \mathcal{I}_1) \left[= u_1 \frac{\partial p}{\partial x_1} + \rho c^2 \frac{\partial u_1}{\partial x_1} \right], \tag{2.139}$$

and the full system of equations can be written as

$$\frac{\partial \rho}{\partial t} + \mathcal{X}_1 + \sum_{n=2}^{d} \frac{\partial \rho u_n}{\partial x_n} = 0, \tag{2.140}$$

$$\frac{\partial \rho u_i}{\partial t} + u_i \mathcal{X}_1 + \rho \mathcal{X}_{i+1} + \sum_{n=2}^{d} \frac{\partial \rho u_i u_n}{\partial x_n} = -\frac{\partial p}{\partial x_i}(1 - \delta_{i1}) - \rho g_i + \frac{\partial \tau_{ij}}{\partial x_j}, \tag{2.141}$$

$$\begin{aligned} \frac{\partial \rho e}{\partial t} + \frac{1}{2}(u_j u_j)\mathcal{X}_1 + \rho u_j \mathcal{X}_{j+1} + \frac{\mathcal{X}_{N_v}}{\gamma - 1} + \sum_{n=2}^{d} \frac{\partial \rho e u_n}{\partial x_n} = \\ - \sum_{n=2}^{d} \frac{\partial p u_n}{\partial x_n} - \rho u_i g_i + \frac{\partial \tau_{ij} u_i}{\partial x_j} - \frac{\partial q_j}{\partial x_j} + \frac{\partial c_{p_l} T s_{jl}}{\partial x_j}, \end{aligned} \tag{2.142}$$

$$\frac{\partial \rho Y_l}{\partial t} + Y_l \mathcal{X}_1 + \rho \mathcal{X}_{l+d+1} + \sum_{n=2}^{d} \frac{\partial \rho Y_l u_n}{\partial x_n} = \frac{\partial s_{jl}}{\partial x_j}. \tag{2.143}$$

The major advantage of casting the equations in this form is that, when considered near a computational boundary, the set of $\mathcal{I}_\kappa$ represent the amplitude variations of the characteristic waves crossing a boundary in the x_1 direction. Caution must used when applying the LODI analysis to numerical simulations, since the full Navier-Stokes equations involve both viscous and tangential terms. The approximation is valid for sufficiently planar waves and small viscosity. The LODI relations have been successfully extended to non-planar three-dimensional waves [52].

The NSCBC are applied by first eliminating a conservation equation corresponding to each inviscid physical boundary condition. Then, the LODI relations (2.122)-(2.126) are used to express the wave amplitude variations, $\mathcal{I}_\kappa$, for the incoming waves in terms of the $\mathcal{I}_\kappa$ for the outgoing waves. Lastly, extra viscous conditions required by the use of the Navier-Stokes equations are applied and the remaining conservation equations (2.140)-(2.143) are solved on the boundaries. Two sample boundary types for subsonic flow are discussed in more detail in the following sections.

The NSCBC that make use of the classical LODI relations cannot be applied successfully to stratified flows such as RTI, since they assume a constant background state. The stratification leads to unstable boundaries and strong wave reflections. One of the objectives of this thesis is to extend these non-reflecting boundary conditions for highly stratified flows.

2.4.2.1 Adiabatic Slip Wall Representation

Representing a slip wall using the LODI relations allows accurate handling of wave reflections for subsonic compressible flows. The single inviscid condition is that the normal velocity at the wall is zero, that is $u_1 = 0$. The only two wave amplitude variations that are not zero are related to one another through (2.123), which gives $\mathcal{I}_1 = \mathcal{I}_{N_v}$, one of which represents an incoming wave, the other an outgoing wave. The outgoing wave $\mathcal{I}_\kappa$ is calculated from internal points and set equal to the incoming wave amplitude variation. The viscous conditions associated with an adiabatic slip wall require zero tangential viscous stresses, normal heat flux, and normal species flux. That is, at the wall,

$$\tau_{12} = \tau_{13} = q_1 = s_{1l} = 0. \tag{2.144}$$

The system is then evolved using the remaining conservation equations (2.140)-(2.143), not including the x_1 momentum equation.

2.4.2.2 Non-Reflecting Boundary Conditions

Whereas a perfectly non-reflecting boundary condition is not likely possible for the general, stable computation of the Navier-Stokes equations, the NSCBC methodology offers an exact non-reflecting treatment of boundaries for one-dimesional systems that remains well-posed for multi-dimensional problems. For compressible problems with waves propagating through a non-reflecting boundary, the mean pressure must be controlled by setting a static pressure p_∞ and allowing small amplitude wave reflections. In this sense, the LODI relations are used for the application of partially-reflecting boundary conditions. By imposing a static pressure, none of the dependent variables are fixed on the boundaries, and all of the conservation equations must be solved. The incoming wave amplitude variation is $\mathcal{I}_{\text{in}} = \mathcal{I}_1$ for the top boundary and $\mathcal{I}_{\text{in}} = \mathcal{I}_{N_v}$ for the bottom boundary. In order to satisfy the condition of constant pressure at infinity, the incoming wave amplitude variation is set to

$$\mathcal{I}_{\text{in}} = K(p - p_\infty), \tag{2.145}$$

such that the pressure at the boundary evolves toward the static pressure over a timescale K^{-1}. The constant coefficient is

$$K = \sigma(1 - M^2)\frac{c}{L}, \tag{2.146}$$

where M is the maximum Mach number in the flow, L is a characteristic size of the domain, and σ is a constant that measures the relative amount of wave reflection. Setting $\sigma = 0$ leads to a perfectly non-reflecting boundary, which makes the system ill-posed. The optimal value in test cases was found to be $\sigma = 0.25$. The viscous conditions require that the tangential stresses, normal heat flux, and normal species flux have zero spatial derivatives along x_1. The conditions,

$$\frac{\partial \tau_{12}}{\partial x_1} = \frac{\partial \tau_{13}}{\partial x_1} = \frac{\partial q_1}{\partial x_1} = \frac{\partial s_{1l}}{\partial x_1} = 0 \tag{2.147}$$

are implemented directly into the system of equations by explicitly setting the derivatives to zero. The system is then evolved using all of the conservation equations (2.140)-(2.143).

Chapter 3

Computational Advances for the Simulation of Compressible Rayleigh-Taylor Instability

Most Rayleigh-Taylor instability (RTI) research focuses on the incompressible regime, whereas most RTI applications, such as type Ia supernovae and inertial confinement fusion, involve highly compressible fluids. The combined effects of compressibility and large density gradients on the late-time behavior of RTI is not currently fully understood [30, 56]. For thermal equilibrium, acoustic and stratification properties of the background flow are interrelated, with stratification itself playing an important role. Attempting to perform numerical simulations of the compressible RTI system introduces a variety of additional complications, such as resolving the acoustic time scale, handling acoustic waves and RT shock waves at the boundaries, and performing computations over a vast range of density scales. In order to capture the late time behavior, the simulations need to be performed in long vertical domains, with density ranges spanning many orders of magnitude. To minimize the computational effort required for high resolution simulations on such domains, adaptive meshes are utilized so that the resolution of the computational grid matches the local scale of the system. Single-mode RTI remains a spatially localized phenomena near the interface well after the bubble and spike have formed. Most of the computational domain is therefore quiescent. Multi-mode systems grow from the small scales of the initial perturbation to large scales as the bubbles merge due to nonlinear mode coupling. Thus, applying an adaptive multiresolution method efficiently resolves the required wide range of scales.

The use of a wavelet-based adaptive method for the simulation of complex fluid systems

permits efficient use of computational resources, since high resolution simulations are performed only where small structures are present in the flow. The wavelets allow the grid to dynamically adapt to the structures in the flow as they evolve in time while maintaining a direct control of the error [79]. The Parallel Adaptive Wavelet Collocation Method (PAWCM) has been efficiently used for simulations of incompressible flows [42, 72] and compressible inert and reactive flows [51, 73]. PAWCM has not been previously used for the study of RTI systems. The extension of PAWCM to simulations of RTI is promising due to the localized nature of the system.

For the compressible case, care must be taken to apply a consistent initialization, such that generation of acoustic waves is suppressed and the instability growth remains pure. Care must also be taken at the computational boundaries in order to remove acoustic and shock waves from the domain, thus isolating the growth of RTI from wave reflections. An investigation of compressible RTI requires the use of efficient numerical methods, advanced boundary conditions, and a consistent initialization in order to capture the wide range of scales present in the system while reducing the computational impact associated with acoustic wave generation and the subsequent interaction with the flow. In the following sections, the nondimensional governing equations and parameters of interest are introduced, optimally consistent initializations are discussed for both the RTI system and a compressible homogeneous isotropic turbulent mixing case, boundary conditions are developed for handling acoustic waves within stratified flows, and various time integration schemes are presented.

3.1 Problem Description

RTI occurs when a light fluid supports a heavier fluid in the presence of a gravity-like body force, an accelerating front, or local differential motions. The density difference at the interface is characterized by the Atwood number. The compressibility effects are measured by the isothermal Mach number, which does not include the effects of the specific heat ratio. The stratification within the system is affected by both the Atwood and Mach numbers.

3.1.1 Nondimensional Governing Equations

The nondimensional form of the governing equations (2.3)-(2.6) is

$$\frac{\partial \rho^*}{\partial t^*} + \frac{\partial \rho^* u_j^*}{\partial x_j^*} = 0, \tag{3.1}$$

$$\frac{\partial \rho^* u_i^*}{\partial t^*} + \frac{\partial \rho^* u_i^* u_j^*}{\partial x_j^*} = -\frac{1}{M^2}\frac{\partial p^*}{\partial x_i^*} - \rho^* \delta_{i1} + \frac{1}{Re}\frac{\partial \tau_{ij}^*}{\partial x_j^*}, \tag{3.2}$$

$$\begin{aligned}\frac{\partial \rho^* e^*}{\partial t^*} + \frac{\partial \rho^* e^* u_j^*}{\partial x_j^*} &= -\frac{1}{M^2}\frac{\partial p^* u_i^*}{\partial x_i^*} - \rho^* u_1^* + \frac{1}{Re}\frac{\partial \tau_{ij}^* u_i^*}{\partial x_j^*} \\ &\quad - \frac{\gamma_I}{M^2(\gamma_I - 1)}\left(\frac{1}{RePr}\frac{\partial q_j^*}{\partial x_j^*} - \frac{1}{ReSc}\frac{\partial c_{p_l}^* T^* s_{jl}^*}{\partial x_j^*}\right),\end{aligned} \tag{3.3}$$

$$\frac{\partial \rho^* Y_l}{\partial t^*} + \frac{\partial \rho^* Y_l u_j^*}{\partial x_j^*} = \frac{1}{ReSc}\frac{\partial s_{jl}^*}{\partial x_j^*}, \tag{3.4}$$

where the asterisk (*) represents a nondimensional variable. The equation of state remains unchanged, $P^* = \rho^* R^* T^*$. The specific total energy is

$$e^* = \frac{1}{2}u_i^* u_i^* + \frac{1}{M^2}\left(\frac{\gamma_I}{\gamma_I - 1}c_p^* T^* - \frac{P^*}{\rho^*}\right). \tag{3.5}$$

The viscous stresses, heat flux, and species flux all remain unchanged,

$$\tau_{ij}^* = \mu^*\left(\frac{\partial u_i^*}{\partial x_j^*} + \frac{\partial u_j^*}{\partial x_i^*} - \frac{2}{3}\frac{\partial u_k^*}{\partial x_k^*}\delta_{ij}\right), \tag{3.6}$$

$$q_j^* = -k^*\frac{\partial T^*}{\partial x_j^*}, \tag{3.7}$$

$$s_{jl}^* = \rho^* D^*\frac{\partial Y_l}{\partial x_j^*}. \tag{3.8}$$

The reference length scale used to nondimensionalize the equations is the width of the domain L_h. For the single-mode case, the initial interface is perturbed with a single mode that fills the domain such that the perturbation wavelength equals the width of the domain, $L_h = \lambda$. The reference pressure and temperature take on the background interfacial values P_I and T_I, where the interface is defined to be the location where the two fluids are equally mixed based on the molar mass fraction, that is $X_{I_1} = X_{I_2} = 1/2$. The molar mass fraction is defined as

$$X_\kappa = \frac{\dfrac{Y_\kappa}{W_\kappa}}{\displaystyle\sum_{l=1}^{N_s}\frac{Y_l}{W_l}}, \tag{3.9}$$

where repeated indices do not imply summation, unless a summation symbol, Σ, is present. For the system with a background state in thermal equilibrium, the reference temperature is simply the background value, $T_I = T_0$.

3.1.2 Nondimensional Parameters

In order to investigate the compressibility effects on RTI, a distinction is made between fluid compressibility characterized by the values of the ratios of the specific heats, γ_1 and γ_2, and compressibility effects in response to the thermodynamic state of the system, characterized by a Mach number defined using the magnitude of a characteristic velocity relative to the speed of sound [53]. Since the flow starts with zero velocity, the Mach number is defined based on the gravity wave speed, $\sqrt{g\lambda}$, which characterizes the instability driving force, and the isothermal speed of sound $a_0 = \sqrt{P_I/\rho_I}$, which removes the effects of the specific heats from the definition [53, 98]. The definition of the isothermal Mach number is

$$M = \sqrt{\frac{\rho_I g\lambda}{P_I}}, \tag{3.10}$$

where the fluid density at the interface is given as

$$\rho_I = \frac{\mathcal{R}T_0}{P_I}\left(\frac{W_1 + W_2}{2}\right). \tag{3.11}$$

For certain classes of initial conditions, such as the thermal equilibrium case, M also determines the vertical variations of the equilibrium density and pressure profiles. In these cases, it can be regarded, in addition, as a stratification parameter [30]. The reference values for the fluid properties, namely μ_I, k_I, c_{p_I}, c_{v_I}, and D_I, are also taken to be the equally mixed quantities based on the molar mass fraction. The equally mixed ratio of specific heats is then defined as $\gamma_I = c_{p_I}/c_{v_I}$. In general, an arbitrary reference velocity scale, U_0, makes necessary the definition of the Froude number. Keeping in mind that the velocity scale, for the case presented here, is set by $U_0 = \sqrt{gL}$, and the length scale is set as $L = \lambda$, a general list of all the nondimensional parameters and their definitions is provided in Table 3.1.

Parameter	Definition	Effect
Atwood number	$A = \frac{W_2 - W_1}{W_2 + W_1}$	variable density / stratification
Mach number	$M = \left(\frac{\rho_I U_0}{P_I}\right)^{1/2}$	acoustic / compressibility / stratification
Reynolds number	$Re = \frac{\rho_I U_0 L}{\mu_I}$	viscous
Schmidt number	$Sc = \frac{\rho_I \mu_I}{D_I}$	mass diffusivity
Prandtl number	$Pr = \frac{c_{p_I} \mu_I}{k_I}$	thermal diffusivity
Froude number	$Fr = \frac{U_0}{(gL)^{1/2}}$	gravitational / stratification
Specific heat ratio	$\gamma_I = \frac{c_{p_I}}{c_{v_I}}$	compressibility

Table 3.1: Relevant parameters for compressible RTI are listed, along with the effects each has on the flow.

3.2 Initialization

The initialization of the thermodynamic quantities and the velocity field for RTI simulations must be derived directly from the governing equations to prevent strong acoustic wave generation at the interface. A mismatch in enthalpy and species diffusion prevents complete consistency, but an initialization strategy can be achieved where pressure disturbances are minimized. Linear stability theory offers consistent initial conditions for a slightly perturbed interface with a stratified background. An ideal initialization for the compressible homogeneous isotropic turbulent mixing case has equal representation of the two pure fluids using the density distribution.

3.2.1 Thermodynamic Initialization for Raleigh Taylor Instability

The RTI system is initialized with a hydrostatic background state, to which linear perturbation fields for density and pressure are added due to the interface perturbation. Alternatively, the modes can also be superimposed such that no perturbation is required for the interface, density, or pressure, but a linear perturbation field for velocity is added.

The background state has a zero velocity field, representing a system at rest. Plugging $u_i = 0$

into the vertical momentum equation, the hydrostatic background state requires:

$$\frac{\partial p^H}{\partial x_1} = -\rho^H g. \tag{3.12}$$

Assuming a background state in thermal equilibrium, $T^H = T_0$, the solution for each fluid is

$$p_m^H = P_I \exp\left(-\frac{g x_1}{R_m T_0}\right), \tag{3.13}$$

$$\rho_m^H = \frac{P_I}{R_m T_0} \exp\left(-\frac{g x_1}{R_m T_0}\right), \tag{3.14}$$

where the subscript m denotes the fluid species.

The nondimensional version of the background equilibrium state is

$$p_{1,2}^{H*} = \exp\left[-M^2(1 \mp A)x_1\right], \tag{3.15}$$

$$\rho_{1,2}^{H*} = (1 \mp A)\exp\left[-M^2(1 \mp A)x_1\right]. \tag{3.16}$$

Figure 3.1 shows the background density profiles for various M and A. It is easily observed from the profiles and the analytical solution for the background density that M is a measure of stratification, and A is a measure of the interfacial density difference, for this case. Additionally, the stratification is also strongly affected by A. At high values of A, the density profiles for the bottom fluid are largely unaffected by M, while the stratification in the top fluid is drastically affected by M.

A single-mode perturbation is added to the hydrostatic background state consistent with linear stability theory [53]. The perturbation fields for the two-dimensional system are of the form

$$p'_m = F_m(x_1)\exp(ikx_2 + nt), \tag{3.17}$$

$$\rho'_m = G_m(x_1)\exp(ikx_2 + nt). \tag{3.18}$$

The x_1-dependent functions are solved from the governing equations (2.13)-(2.15) with the imposed solution from (3.17) and (3.18), as is done is Section 2.2.2. For the fully compressible case, the growth rate n is described through the nonlinear relationship (2.32). The extension of linear stability analysis to the compressible case has shown that the effects of compressibility on the early time growth rate are not characterized by a single parameter [53]. The added complexity due to

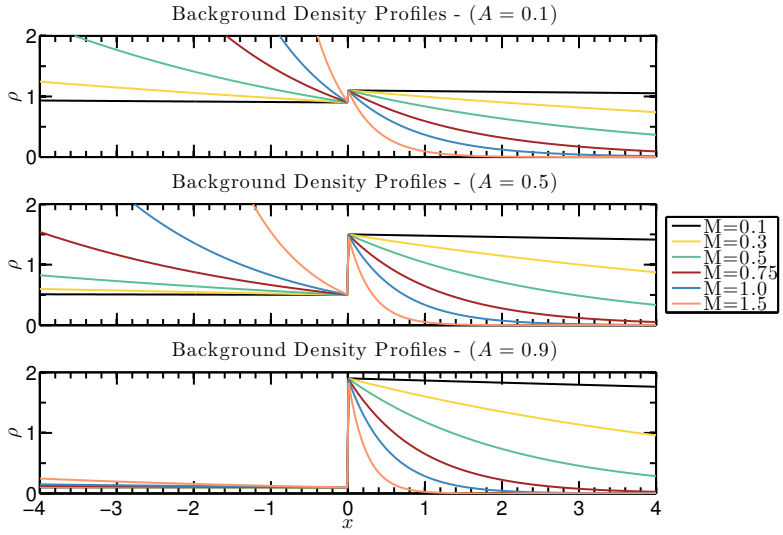

Figure 3.1: Background density profiles at various M and A for the thermal equilibrium case.

the effects of compressibility is expected to increase as the late time growth of RTI is investigated. The initial fields for pressure and density for each fluid are

$$p_m = p_m^H + p'_m, \tag{3.19}$$

$$\rho_m = \rho_m^H + \rho'_m. \tag{3.20}$$

To ensure the initialization is well resolved, the interface is smoothed by setting the molar mass fraction to $X_1 = [1 + \mathrm{erf}((x_1 - \eta_I(x_2, x_3))/\delta)]/2$, where $\eta_I(x_2, x_3)$ represents the location of the perturbed interface, and δ is the initial diffusion thickness of the interface. The error function is used in the molar mass fraction initialization because it is an exact solution to the diffusion equation. This initialization allows for an analytical solution of the smoothed background pressure and density fields,

$$p^H = P_I \exp\left[\frac{-g}{RT_0}\left(x_1 - \eta_I - \frac{\delta^2}{2}\frac{\partial \ln R}{\partial x_1}\right)\right], \tag{3.21}$$

$$\rho^H = \frac{p^H}{RT_0}. \tag{3.22}$$

These definitions represent smoothed fields because the gas constant takes on the local value according to the local mass fraction. Additionally, the extra smoothing term in the exponential is a

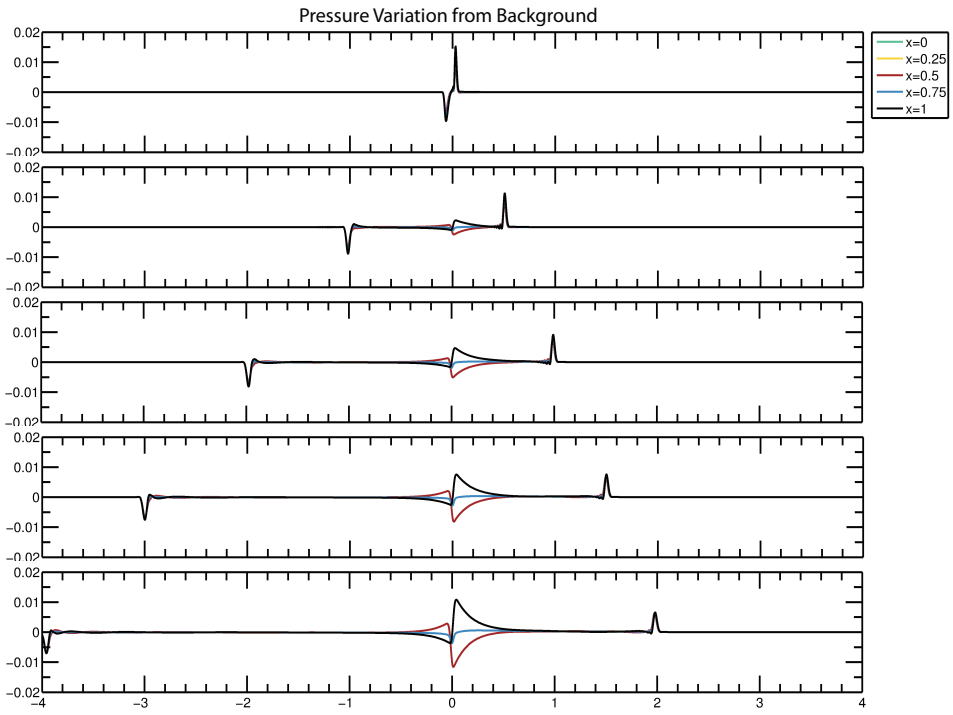

Figure 3.2: The stationary, isothermal, hydrostatic background state leads to the generation of strong acoustic waves at the interface. The plots show the time evolution of vertical lines of the pressure variations from background state, where time increases downward.

direct result of the molar mass fraction initialization.

The initial fields are smoothed at the interface using the contribution of the pure fluid solution to the smoothed hydrostatic background state. That is,

$$p = p_1 \frac{p^H}{p_1^H} \quad \text{and} \quad \rho = \rho_1 \frac{\rho^H}{\rho_1^H} \quad \text{for} \quad x_1 \geq \eta_I, \tag{3.23}$$

$$p = p_2 \frac{p^H}{p_2^H} \quad \text{and} \quad \rho = \rho_2 \frac{\rho^H}{\rho_2^H} \quad \text{for} \quad x_1 \leq \eta_I, \tag{3.24}$$

The perturbed initial temperature is then derived from the equation of state. Any potential jump in temperature at the interface is smoothed by numerically solving the diffusion equation for the temperature field. The smoothing is only done until the temperature field is well resolved. Any variation introduced from this final smoothing process is accounted for in the density field.

3.2.2 Velocity Field Initialization for Raleigh Taylor Instability

A zero velocity initialization is an obvious choice for the comparison of numerical simulations to experimental results, since most experiments attempt to start with static fluids. The zero initial velocity assumption is an intrinsic part of the linear stability analysis, which leads to consistent initial fields for the thermodynamic variables. The governing equations can be written as

$$\frac{\mathcal{D}\rho}{\mathcal{D}t} = -\rho\frac{\partial u_j}{\partial x_j}, \tag{3.25}$$

$$\frac{\mathcal{D}u_i}{\mathcal{D}t} = -\frac{1}{\rho}\frac{\partial p}{\partial x_i} - g_i + \frac{1}{\rho}\frac{\partial \tau_{ij}}{\partial x_j}, \tag{3.26}$$

$$\begin{aligned}\frac{\mathcal{D}p}{\mathcal{D}t} &= -\gamma p\frac{\partial u_j}{\partial x_j} + (\gamma-1)\,\tau_{ij}\frac{\partial u_i}{\partial x_j} + (\gamma-1)\,\frac{\partial}{\partial x_j}\left[k\frac{\partial T}{\partial x_j}\right] \\ &\quad + (\gamma-1)\,D\rho\frac{\partial c_P}{\partial x_j}\frac{\partial T}{\partial x_j} + \gamma T\frac{\partial}{\partial x_j}\left[D\rho\frac{\partial R}{\partial x_j}\right],\end{aligned} \tag{3.27}$$

$$\frac{\mathcal{D}R}{\mathcal{D}t} = \frac{1}{\rho}\frac{\partial}{\partial x_j}\left[D\rho\frac{\partial R}{\partial x_j}\right], \tag{3.28}$$

where $\mathcal{D}/\mathcal{D}t$ represents the material derivative. Applying the stationary ($u_i = 0$), isothermal ($T = T_0$), and hydrostatic ($\partial p/\partial x_i = -\rho g_i$) assumptions to the governing equations associated with the background state leads to $\mathcal{D}p/\mathcal{D}t \neq 0$. The inconsistency arises because the species diffusion leads to a nonzero enthalpy diffusion term in the energy equation, which inevitably creates disturbances in the pressure field at the interface. These disturbances lead to the generation of relatively strong acoustic waves that propagate out from the initial interface. Figure 3.2 shows the generation and propagation of strong acoustic waves due to the inconsistent initialization.

The initialization can be improved by minimizing the pressure disturbances in place of the stationary assumption. In order to satisfy $\mathcal{D}p/\mathcal{D}t = 0$ after applying only the isothermal ($T = T_0$) and hydrostatic ($\partial p/\partial x_i = -\rho g_i$) assumptions, and neglecting the viscous term, a balance is required for the remaining two terms,

$$\gamma p\frac{\partial u_j}{\partial x_j} = \gamma T\frac{\partial}{\partial x_j}\left[D\rho\frac{\partial R}{\partial x_j}\right]. \tag{3.29}$$

An equation for the divergence of velocity is found and expanded as

$$\frac{\partial u_j}{\partial x_j} = \frac{1}{\rho R}\frac{\partial}{\partial x_j}\left[D\rho\frac{\partial R}{\partial x_j}\right] = \frac{\partial}{\partial x_j}\left[D\frac{\partial \ln R}{\partial x_j}\right] + D\frac{\partial \ln R}{\partial x_j}\frac{\partial \ln \rho R}{\partial x_j}. \tag{3.30}$$

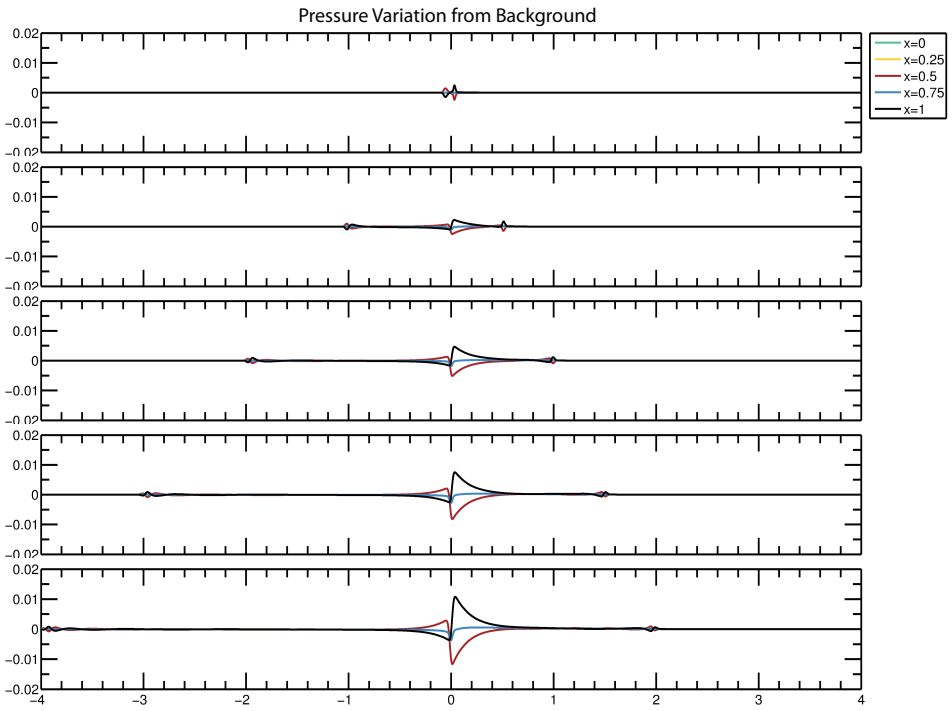

Figure 3.3: The diffused, isothermal, hydrostatic background state leads to the generation of weak acoustic waves at the interface. The plots show the time evolution of vertical lines of the pressure variations from background state, where time increases downward.

The last term typically has a small contribution, but may become significant for highly stratified cases with large initial diffusion thickness. The final term is neglected, leaving a divergence on both sides of the equation,

$$\frac{\partial u_j}{\partial x_j} = \frac{\partial}{\partial x_j}\left[D\frac{\partial \ln R}{\partial x_j}\right], \tag{3.31}$$

which is integrated to give the initial velocity field for minimizing pressure disturbances at the interface,

$$u_i = D\frac{\partial \ln R}{\partial x_i}. \tag{3.32}$$

For variable density flows in the limit of incompressible pure fluids, mixing by species diffusion leads to non-zero divergence of velocity [54], which is equivalent to the result obtained for the compressible case. Thus, the modified initialization represents a non-stationary, diffused, isothermal, hydrostatic background state. Figure 3.3 shows the generation and propagation of acoustic disturbances that

are weak compared to the waves generated from the stationary background state shown in Figure 3.2.

With the presence of initial diffusive mixing in the compressible case, there is no way to obtain a fully consistent initialization that accounts for both the species and enthalpy diffusion in the energy equation. Therefore, acoustic waves are necessarily generated from the initial conditions, whose magnitudes are dependent upon M, A, D, and the initial diffusive layer thickness, δ. The diffused background state is an optimally consistent initialization, where small pressure disturbances are introduced due to the presence of the viscous terms, the neglected term in the divergence of velocity formula given in (3.30), and the interaction between the background state and the initial perturbed fields consistent with linear stability theory. The acoustic waves are greatly reduced by setting the initial velocity field to the diffusive mixing velocity given in (3.32). The initialization represents a diffused interface that experiences a sudden perturbation. The effects of the diffused and perturbed interface are introduced independently, but are combined in (3.23).

The advantages of the diffused initialization over a zero velocity initial state include higher consistency, uncontaminated flow evolution, and more efficient use of computational resources. The original motivation for applying a stationary initialization in order to match experiments is actually a significant approximation when miscible fluids are used in the lab. The diffused initialization is optimally consistent in terms of acoustic generation and is a better physical representation of any real system. Furthermore, any acoustic wave generated at the interface must be dealt with at the boundaries of the computational domain, in order to prevent wave reflection and contamination of the pure instability growth. When adaptive grids are used for numerical simulations of RTI, additional computational resources must be used to resolve the propagation of the acoustic waves generated from the inconsistencies in the initialization. Waves with higher amplitudes require higher resolution, and more resources are used to resolve the acoustics instead of the RTI growth. This can be observed in the adaptive grids associated with the two initializations, shown in Figure 3.4. The stationary initialization generates stronger acoustic waves and requires almost three times the number of active wavelets used to represent the diffused initialization case, where the acoustic

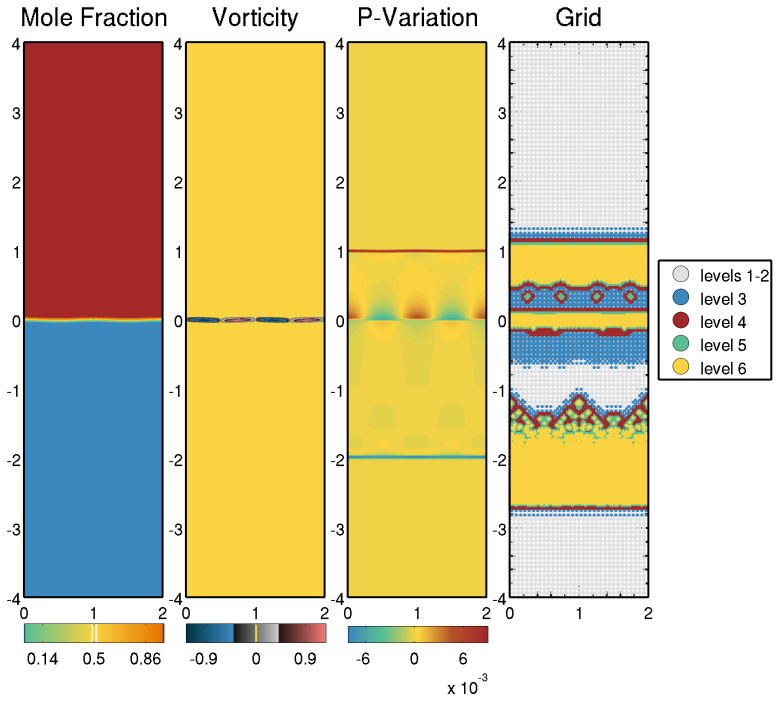

(a) Stationary Initialization

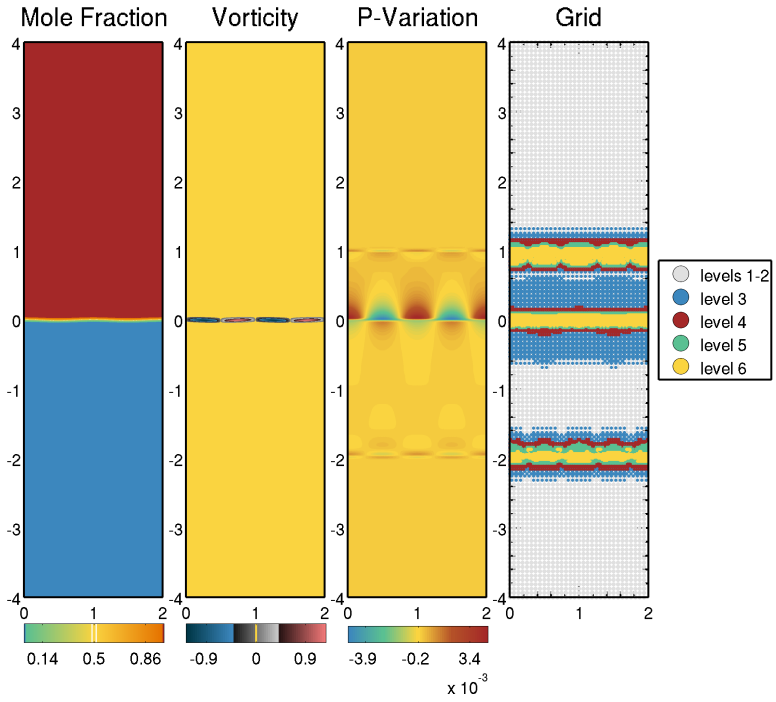

(b) Diffused Initialization

Figure 3.4: Early time acoustic wave propagation for the two initializations. The grid for the stationary and diffused initializations encompass 116,828 and 39,537 active wavelets, respectively.

generation is much weaker. The acoustic effect on the adaptive grid also has a longer duration for stronger acoustic waves. The adaptive grids at a later time, where the RTI growth is well into the linear regime, are shown in Figure 3.5. The computational boundaries represent reflecting walls, such that the acoustic waves remain inside the computational domain and their late time effects can be observed. The grid continues to resolve the acoustics from the stationary initialization, whereas the diffused initialization case is only weakly adapting to the waves. Even at this late time, the zero initial velocity case uses 57% more points than the optimally consistent initialization.

3.2.3 Consistent Initialization for Compressible Homogeneous Isotropic Turbulent Mixing

The turbulent mixing layer of RTI is often studied as a homogeneous buoyancy-driven VD flow, where the fluids are assumed incompressible. For significantly late times and, consequently, wide mixing regions, the turbulence that occurs deep within the layer, away from the edges, is statistically homogeneous. As discussed in Section 2.3.1.6, the homogeneous RT system is investigated in an attempt to understand the physics of turbulent mixing subjected to differential accelerations. Compressible variable density (CVD) flows are characterized by the molecular mixing of fluids with different molar masses. A simple CVD flow is compressible homogeneous isotropic turbulent mixing (CHITM), which is valuable for studying the compressibility effects on molecular mixing. With the exception of the buoyancy terms, the governing equations for CHITM are equivalent to those used for compressible RTI simulations.

The CHITM system is initialized as random blobs of two pure compressible fluids, subjected to a turbulent velocity field. As the turbulence decays, the fluids mix, inevitably resulting in a perfect mixture of the two fluids filling the domain. The mixing rates of the two fluids are evaluated from the evolution of the probability density function (PDF) for various flow properties that measure the relative concentrations of the pure fluid species. The problem is assumed triply-periodic without gravitational effects. The buoyancy-driven turbulence that occurs within the RT mixing layer is therefore replaced with an initial turbulent velocity field in the CHITM system.

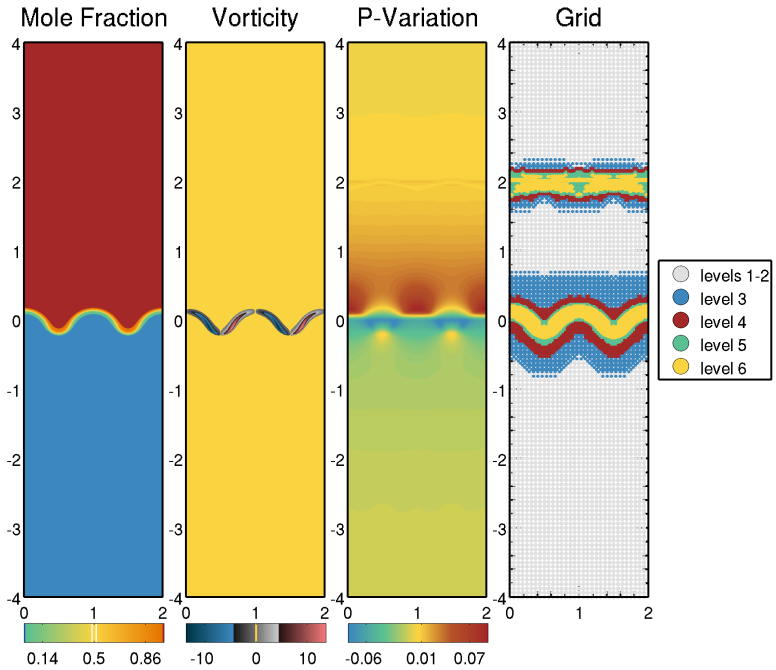

(a) Stationary Initialization

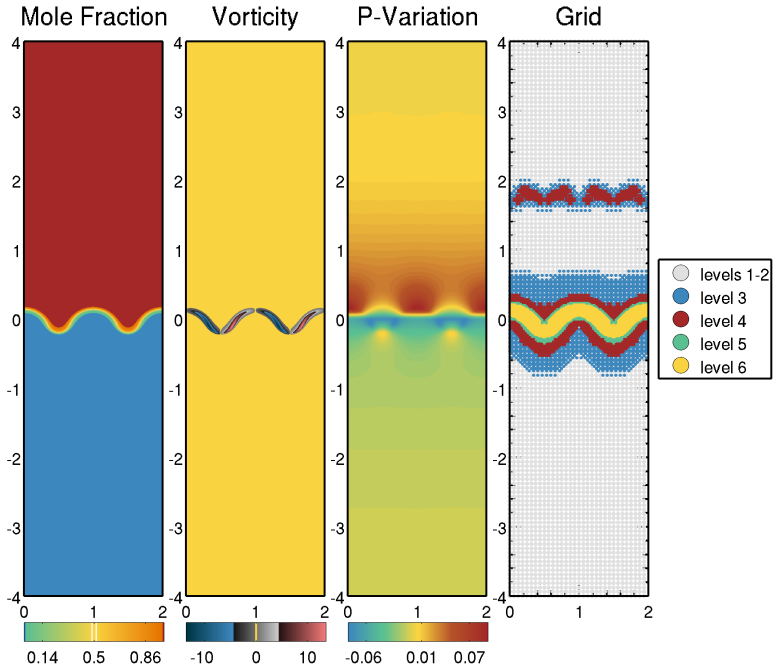

(b) Diffused Initialization

Figure 3.5: Late time acoustic wave propagation for the two initializations showing the duration of acoustic effect on the adaptive grid. The grid for the stationary and diffused initializations have 32,173 and 20,465 active wavelets, respectively.

The velocity scale is set by the isothermal speed of sound $a_0 = \sqrt{P_I/\rho_I}$. The compressibility effects are again split between the thermodynamic and specific heat ratio effects, by defining the Mach number based on the initial turbulent kinetic energy k_t and the isothermal speed of sound,

$$M = \sqrt{\frac{\rho_I k_t}{P_I}}. \tag{3.33}$$

A consistent initialization is important for physically accurate simulations of CHITM. The ideal initial state is composed of large random blobs of two pure fluids, which is then subjected to a turbulent velocity field to generate the mixing. In order to explore the mixing between two pure fluids, the initial state should be composed of a density field where the two fluids are equally present. The PDF for the density field should therefore consist of two sharp peaks, corresponding to the densities of the two pure fluids at the mean pressure and temperature of the thermodynamically equilibrated state. The fluids are assumed miscible. Therefore, the interfaces between the initial blobs of pure fluid have a small diffusive layer. The resulting initial PDF for ρ should be nearly-double-delta with minimal frequency for the values between the peaks. There are various strategies, each assuming different thermodynamic equilibrium conditions, that may be used to obtain the initial fields. An ideal initialization has nearly equal concentrations of each of the pure fluids based on the density field. Furthermore, an accurate initialization must ensure that all of the variables remain physical. For example, the mass fractions, Y_l, must be bounded by zero and one.

A random solenoidal velocity field, u_i^s, is generated with the following spectrum

$$E(k) = \frac{k^4}{k_0^5} \exp\left[-2\left(\frac{k}{k_0}\right)^2\right], \tag{3.34}$$

where $\mathbf{k}$ is the wavenumber vector in Fourier space, the wavenumber magnitude is $k = |\mathbf{k}|$, and k_0 is a reference wavenumber that controls the width of the spectrum. The thermodynamic quantities are found using this divergence-free velocity field, consistent with the compressible equations.

In order to obtain an initialization with the idealized nearly-double-delta PDF, a field is assigned a random Gaussian distribution with a low wavenumber top-hot spectrum. All negative values are set to zero, and all positive values are set to one, creating random large-scale blobs with

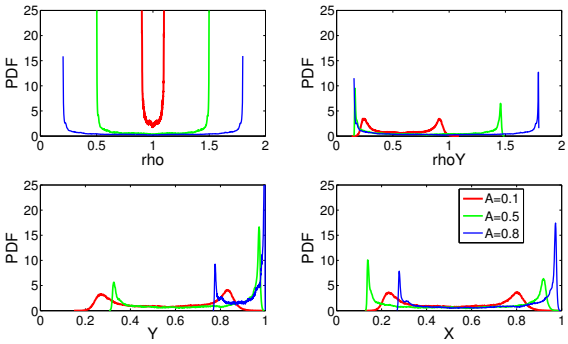

(a) ρ-Symmetric Initialization

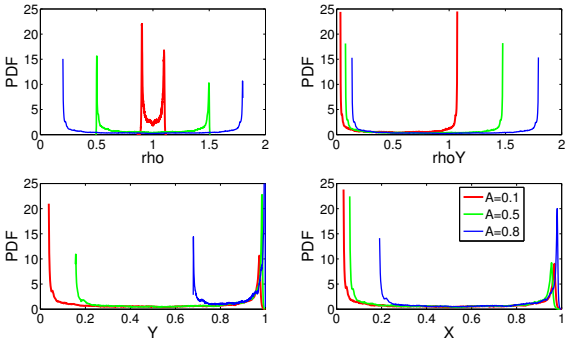

(b) ρY-Symmetric Initialization

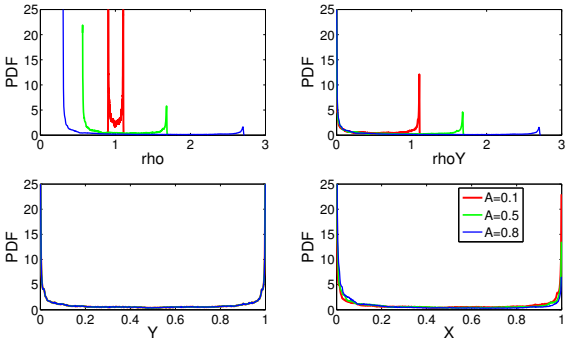

(c) Y-Symmetric Initialization

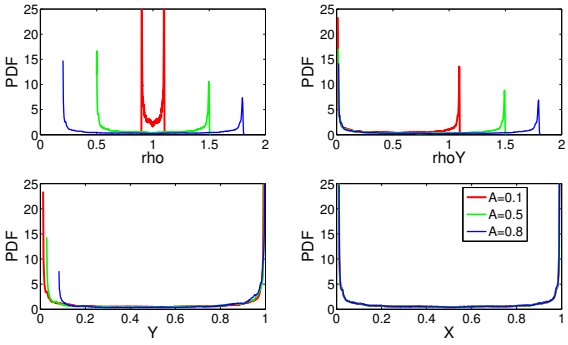

(d) X-Symmetric Initialization

Figure 3.6: The PDFs associated with the four initialization strategies.

a true double-delta PDF. This field is characterized by sharp interfaces and is referred to as ψ_{sh}. The field is slightly diffused so that the interfaces are well-resolved by applying a smoothing filter in Fourier space,

$$\hat{\psi}_{\text{sm}} = \hat{\psi}_{\text{sh}} e^{-\alpha_d k^2}, \tag{3.35}$$

where α_d is a smoothing parameter, chosen just large enough to fully resolve the interface. The resulting field now has a nearly-double-delta PDF. The initial state is produced by setting a particular variable, one that represents the relative concentration of each fluid, based on ψ_{sm}. Since the ideal initialization contains equal amounts of the pure fluid densities, assigning ψ_{sm} to the density field is a natural choice, and is referred to as the ρ-symmetric initialization. Additionally, the heavy fluid mass fraction, Y_2, volume fraction, ρY_2, or molar mass fraction, X_2, can also be initialized algebraically using ψ_{sm}. The definitions for the first step of each of these four initialization strategies are as follows,

$$\rho\text{-symmetric:} \qquad \rho = \frac{P_I}{\mathcal{R}T_0}\left[(W_2 - W_1)\psi_{\text{sm}} + W_1\right], \tag{3.36}$$

$$Y\text{-symmetric:} \qquad Y_2 = \psi_{\text{sm}}, \tag{3.37}$$

$$\rho Y\text{-symmetric:} \qquad \rho Y_2 = \frac{P_I W_2}{\mathcal{R}T_0}\psi_{\text{sm}}, \tag{3.38}$$

$$X\text{-symmetric:} \qquad X_2 = \psi_{\text{sm}}. \tag{3.39}$$

The remaining thermodynamic variables are computed through an assumption about the equilibrium state and by taking the divergence of the momentum equations. The isothermal assumption, with constant $T = T_0$, is the most straightforward. Neglecting the viscous term, the divergence of the momentum equations give

$$\frac{\partial}{\partial x_i}\left[u_j^s \frac{\partial u_i^s}{\partial x_j}\right] = -T_0 \frac{\partial}{\partial x_i}\left[\frac{1}{\rho}\frac{\partial \rho R}{\partial x_i}\right], \tag{3.40}$$

which can be solved for ρ or Y_2, depending on the initialization type.

The four initialization strategies are compared based on the quality of the PDFs for the derived fields. The PDFs of ρ, ρY_2, Y_2, and X_2 that are obtained using each of the initialization types is shown in Figure 3.6. The ρ-symmetric case is the natural choice, but the Y PDF for high

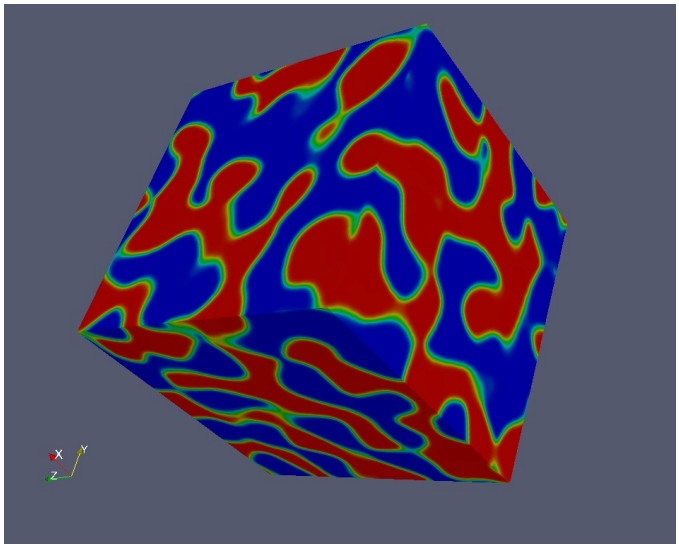

Figure 3.7: The CHITM system is initialized as random blobs of pure fluids with different molar masses.

Atwood numbers is heavily skewed toward the heavy fluid, such that the pure light fluid is poorly represented. The ρY-symmetric initialization similarly leads to skewed PDFs of Y at high A. The Y-symmetric strategy gives density PDFs where the height of the peaks are drastically different. Thus, the best choice for the isothermal case is the X-symmetric initialization, since the PDFs of ρ and Y both represent a system of pure fluids with equal concentration. The resulting three-dimensional initial field for the density is displayed in Figure 3.7. The set of possible initializations is easily extended to include the thermodynamic equilibrium state where $\rho R = \text{const}$, which corresponds to the incompressible limit. For this case, the ρ-symmetric and X-symmetric cases are identical. Also, ρ and Y_2 can be algebraically computed for all four initialization strategies.

The species transport equations give a relationship for the dilatational velocity field that is applicable for the mixing of pure incompressible fluids, where $\rho R = \text{const}$, [54],

$$\frac{\partial u_j^d}{\partial x_j} = -\frac{\partial}{\partial x_j}\left(D\frac{\partial \ln \rho}{\partial x_j}\right). \tag{3.41}$$

It is assumed that the dilatational velocity is strictly due to the diffusive mixing of the fluids. The full velocity field is taken to be the sum of the dilatational velocity,

$$u_j^d = -D\frac{\partial \ln \rho}{\partial x_j}, \tag{3.42}$$

and the turbulent solenoidal part, that is $u_i = u_i^s + u_i^d$.

The pressure field is then obtained from the divergence of the momentum equations, where the viscous terms are included such that the initialization is consistent for all Re,

$$\frac{\partial}{\partial x_i}\left[\frac{1}{\rho}\frac{\partial p}{\partial x_i}\right] = -\frac{\partial}{\partial x_i}\left[\frac{\partial u_i}{\partial t}\right] - \frac{\partial}{\partial x_i}\left[u_j\frac{\partial u_i}{\partial x_j}\right] + \frac{\partial}{\partial x_i}\left[\frac{1}{\rho}\frac{\partial \tau_{ij}}{\partial x_j}\right]. \tag{3.43}$$

Simplifying the evolution term requires only the dilatational part of the velocity field and uses the continuity equation to obtain

$$-\frac{\partial}{\partial x_i}\left[\frac{\partial u_i}{\partial t}\right] = -\frac{\partial}{\partial t}\left[\frac{\partial u_i}{\partial x_i}\right] = \frac{\partial}{\partial t}\left[\frac{\partial}{\partial x_i}\left(D\frac{\partial \ln\rho}{\partial x_i}\right)\right] = \frac{\partial}{\partial x_i}\left[D\frac{\partial}{\partial x_i}\left(\frac{1}{\rho}\frac{\rho u_j}{\partial x_j}\right)\right]. \tag{3.44}$$

With the rewritten evolution term, the right-hand side of the equation for pressure is represented by the Laplacian of a function, F, where

$$\frac{\partial^2 F}{\partial x_i \partial x_i} = \frac{\partial}{\partial x_i}\left[D\frac{\partial}{\partial x_i}\left(\frac{1}{\rho}\frac{\rho u_j}{\partial x_j}\right)\right] - \frac{\partial}{\partial x_i}\left[u_j\frac{\partial u_i}{\partial x_j}\right] + \frac{\partial}{\partial x_i}\left[\frac{1}{\rho}\frac{\partial \tau_{ij}}{\partial x_j}\right]. \tag{3.45}$$

This substitution takes advantage of the relative ease of computing inverse Laplacians, such that F can be treated as a known quantity. The equation for pressure is

$$\frac{\partial}{\partial x_i}\left[\frac{1}{\rho}\frac{\partial p}{\partial x_i}\right] = \frac{\partial^2 F}{\partial x_i \partial x_i}. \tag{3.46}$$

Integrating once gives

$$\frac{1}{\rho}\frac{\partial p}{\partial x_i} = \frac{\partial F}{\partial x_i} + Z_i, \tag{3.47}$$

where the Z_i are global constants, but are not known and must be computed. In order to solve for pressure, equation (3.47) is rewritten as a Poisson equation for pressure as,

$$\frac{\partial^2 p}{\partial x_i \partial x_i} = \frac{\partial}{\partial x_i}\left[\rho\frac{\partial F}{\partial x_i}\right] + Z_j\frac{\partial \rho}{\partial x_j}. \tag{3.48}$$

The terms on the right-hand side are rewritten as Laplacians,

$$\frac{\partial^2 G}{\partial x_i \partial x_i} = \frac{\partial}{\partial x_i}\left[\rho\frac{\partial F}{\partial x_i}\right], \tag{3.49}$$

$$\frac{\partial^2 Q_j}{\partial x_i \partial x_i} = \frac{\partial \rho}{\partial x_j}, \tag{3.50}$$

such that G and Q_j can be computed by taking inverse Laplacians. This leads to a simple differential equation for pressure,

$$\frac{\partial^2 p}{\partial x_i \partial x_i} = \frac{\partial^2 G}{\partial x_i \partial x_i} + \frac{\partial^2 Q_j Z_j}{\partial x_i \partial x_i}, \tag{3.51}$$

which is solved for the perturbation of pressure from the background state as

$$p' = G + Q_j Z_j. \tag{3.52}$$

The constant background pressure can then be added to obtain the full solution for pressure as $p = P_I + p'$. Once pressure is calculated, temperature is solved using the equation of state, $T = p/\rho R$.

In order to compute the pressure, the Z_i must first be calculated. Since the domain is periodic in all dimensions, taking a spatial average of equation (3.47) gives,

$$\left\langle \frac{1}{\rho} \frac{\partial p}{\partial x_i} \right\rangle = Z_i, \tag{3.53}$$

where $\langle G \rangle$ signifies the spatial average of the quantity G. The solution for pressure can be rewritten to match the form of Z_i by taking the gradient of equation (3.52), dividing by density, and averaging to obtain

$$Z_i = \left\langle \frac{1}{\rho} \frac{\partial G}{\partial x_i} \right\rangle + Z_j \left\langle \frac{\partial Q_j}{\partial x_i} \right\rangle, \tag{3.54}$$

which is a simple algebraic system of equations that can be solved for Z_i.

3.3 Boundary Conditions

For compressible RTI, pressure waves are generated at the interface from the initialization and continuously as the instability grows [60]. The acoustic waves travel outward and must be dealt with at the computational boundaries. Figure 3.8 shows the background density and pressure profiles associated with the test case used for presenting the various boundary conditions. The A and M are chosen such that the acoustic speed of the light fluid is exactly twice that of the heavy fluid. The stratification within each pure fluid adds an additional layer of complexity that must be accounted for when treating the computational boundaries. Figure 3.9 shows the acoustic

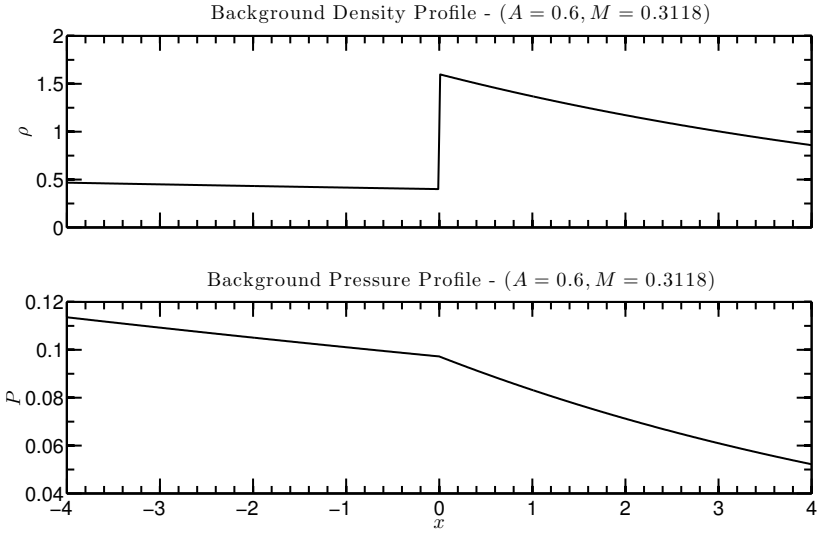

Figure 3.8: Background density and pressure profiles for the $A = 0.6$ and $M = 0.3118$ case.

wave generation and propagation for the test case when slip walls are applied at the vertical boundaries. Vertical lines of the pressure variations from the background state are shown, with time increasing downward. The wave is free to reflect off the walls and interfere with the growth of the instability, thus highlighting the importance of properly handling the acoustic disturbances near the boundaries. Multiple vertical lines are displayed to show the planar nature of the wave. Simulations of RTI are performed with a domain that is periodic in the horizontal (x_2) direction. The boundary conditions in the vertical (x_1) direction are designed to simulate an infinite domain such that any pressure wave approaching the numerical boundaries is not reflected and, thus, does not interact with and disturb the growth of the instability. The instability is isolated by applying either a diffusion buffer zone or non-reflecting characteristics-based boundary conditions at the top and bottom of the domain.

3.3.1 Numerical Diffusion Buffer Zone

Applying a numerical diffusion zone near the vertical edges of the computational domain does not remove the acoustic waves, but sufficiently reduces the intensity such that any wave reflection has negligible effect on the flow. The zone must be large enough for sufficient damping to occur.

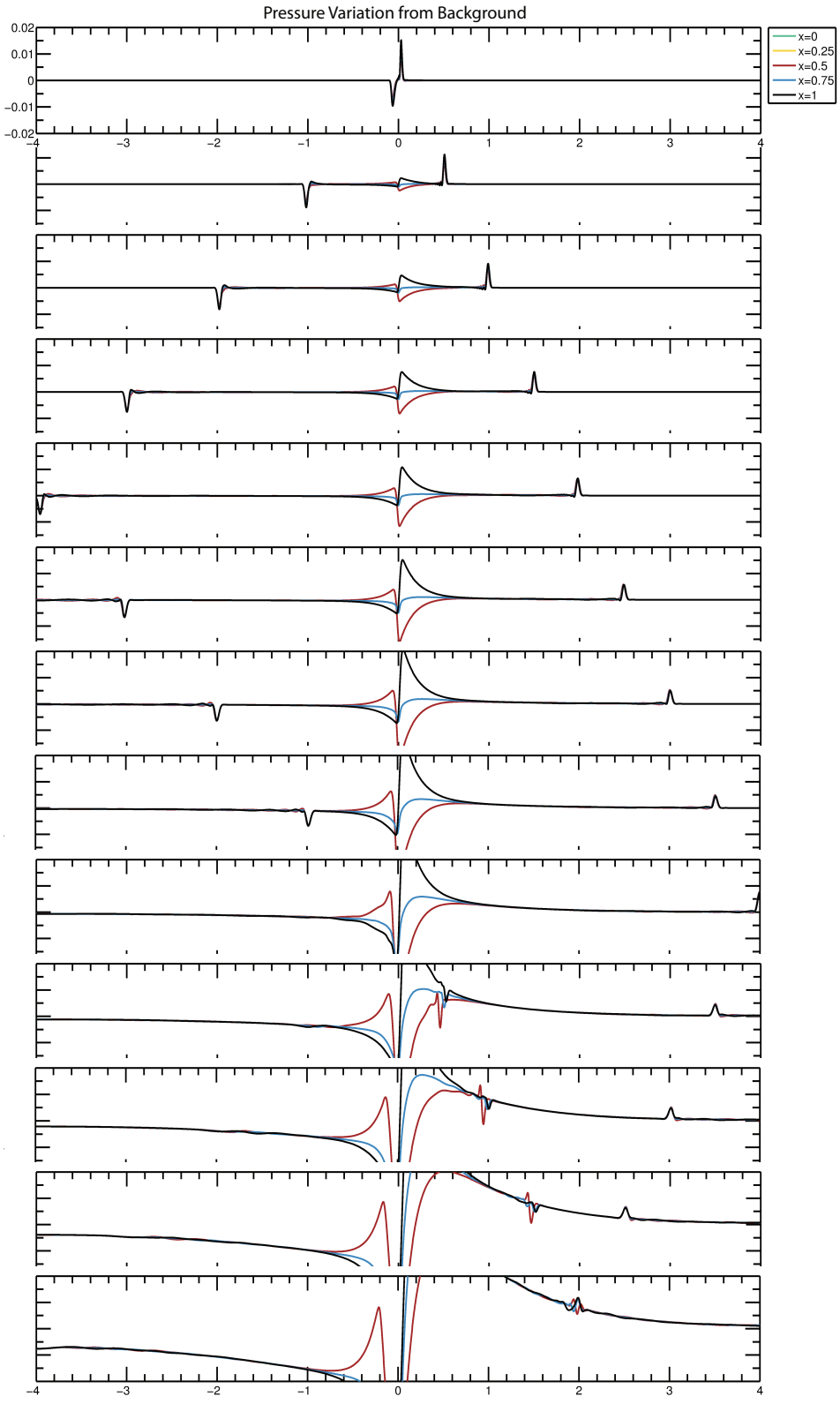

Figure 3.9: Acoustic wave propagation with slip wall boundaries.

Since an adaptive grid is utilized, the computational cost of the buffer layer is negligible. Therefore, the buffer layer can be extended to extreme lengths to accommodate large damping.

The governing equations (2.3)-(2.6) are rewritten as

$$\frac{\partial \mathbf{U}}{\partial t} = \mathbf{F}(\mathbf{U}), \tag{3.55}$$

where all of the evolved variables are combined as $\mathbf{U} = [\rho, \rho u_i, \rho e, \rho Y_l]$, and $\mathbf{F}(\mathbf{U})$ represents all of the terms but the time derivatives. The fully conservative formulation of the diffusion buffer zone for a one-dimensional system is

$$\frac{\partial \mathbf{U}_i}{\partial t} = \mathbf{F}(\mathbf{U})_i + \frac{1}{\Delta x}\left[\xi_{i+1/2}\left(\frac{\mathbf{U}^P_{i+1} - \mathbf{U}^P_i}{\Delta x}\right) - \xi_{i-1/2}\left(\frac{\mathbf{U}^P_i - \mathbf{U}^P_{i-1}}{\Delta x}\right)\right], \tag{3.56}$$

where the subscripts signify the indices for the spatial grid, ξ is a function that accounts for the geometry and local strength of the numerical diffusion zone, and $\mathbf{U}^P$ represents the perturbed quantities of the evolved variables from the background state, $\mathbf{U}^P = \mathbf{U} - \mathbf{U}^H$. Performing the numerical diffusion on the perturbation quantities accounts for spatially varying fields, specifically those affected by the stratification intrinsic to compressible RTI.

Using smooth transitions for the diffusion buffer layer near the vertical boundaries, where the strength of the diffusive effects is gradually increased, allows the use of a simplified non-conservative scheme,

$$\frac{\partial \mathbf{U}}{\partial t} = \mathbf{F}(\mathbf{U}) + \nu_d \xi_d \frac{\partial^2_L \mathbf{U}^P}{\partial x_i \partial x_i} - \sigma_b \xi_b \mathbf{U}^P. \tag{3.57}$$

This formulation diffuses momentum and reduces kinetic energy in the buffer zone, but it is not fully conservative. The function $\xi_d(x_1)$ represents a mask function for the numerical diffusion zone. In the middle of the domain, $\xi_d = 0$, and no numerical diffusion is applied. Near the boundaries, ξ_d is gradually increased to one. The numerical diffusion coefficient, ν_d, is set locally to

$$\nu_d(x_1, x_2, x_3, t) = \left(2\Delta t \sum_\alpha \frac{1}{\Delta x^2_\alpha}\right)^{-1}, \tag{3.58}$$

where Δx_α changes is space and time as the grid dynamically adapts to the flow. Setting the diffusion coefficient in this way allows for maximum diffusion without introducing additional stability

requirements. A low order derivative is used for the diffusion terms in order to reduce computational cost and to preserve monotonicity. The 'L' subscript on the second derivative signifies the low order nature of the discretized operator.

A Brinkman-type penalization term is included to force the solution toward the background state within the Brinkman zone, represented by the Brinkman mask function, ξ_b. In practice, it is common to use the same mask function for both the numerical diffusion zone and the Brinkman zone; that is, $\xi_b = \xi_d$. The forcing parameter, σ_b, is inversely proportional to the timescale of the damping. Large values of σ_b lead to a rapid driving of the solution to the background state at the expense of wave reflections at the boundaries of the Brinkman zone. At the opposite extreme, significantly small values of σ_b result in no forcing effect on the solution. An optimal amount of forcing for simulations of compressible RTI within the numerical diffusion zone is achieved using

$$\sigma_b = 0.25\frac{c}{L}, \tag{3.59}$$

where c is the characteristic acoustic speed and L is a characteristic length scale. The local pure fluid acoustic speeds and length scales are applied, which leads to the final form of the forcing parameter,

$$\sigma_{b,\kappa} = 0.25\sqrt{\frac{\gamma_\kappa \mathcal{R} T_0}{W_\kappa \lambda^2}}, \tag{3.60}$$

where summation over the repeated index, κ, is not assumed. Thus, the numerical diffusion zone at the bottom and top of the computational domain have different forcing parameters, $\sigma_{b,1}$ and $\sigma_{b,2}$ respectively.

A numerical diffusion buffer zone is applied to the test case and shown in Figure 3.10. The diffusion layer mask, ξ_d, is gradually increased from zero to one between $3 < |x| < 3.25$, and the buffer zone takes full force, $\xi_d = 1$, where $3.25 < |x| < 4$. Slip wall conditions are applied at the top and bottom boundaries. When compared to the case without a diffusion zone, the acoustic waves are quickly and drastically damped upon entering the diffusion layer. The waves are not completely removed, but the amplitude is reduced significantly. This reduces the impact the acoustics have on the instability growth, while eliminating the computational cost of resolving the waves.

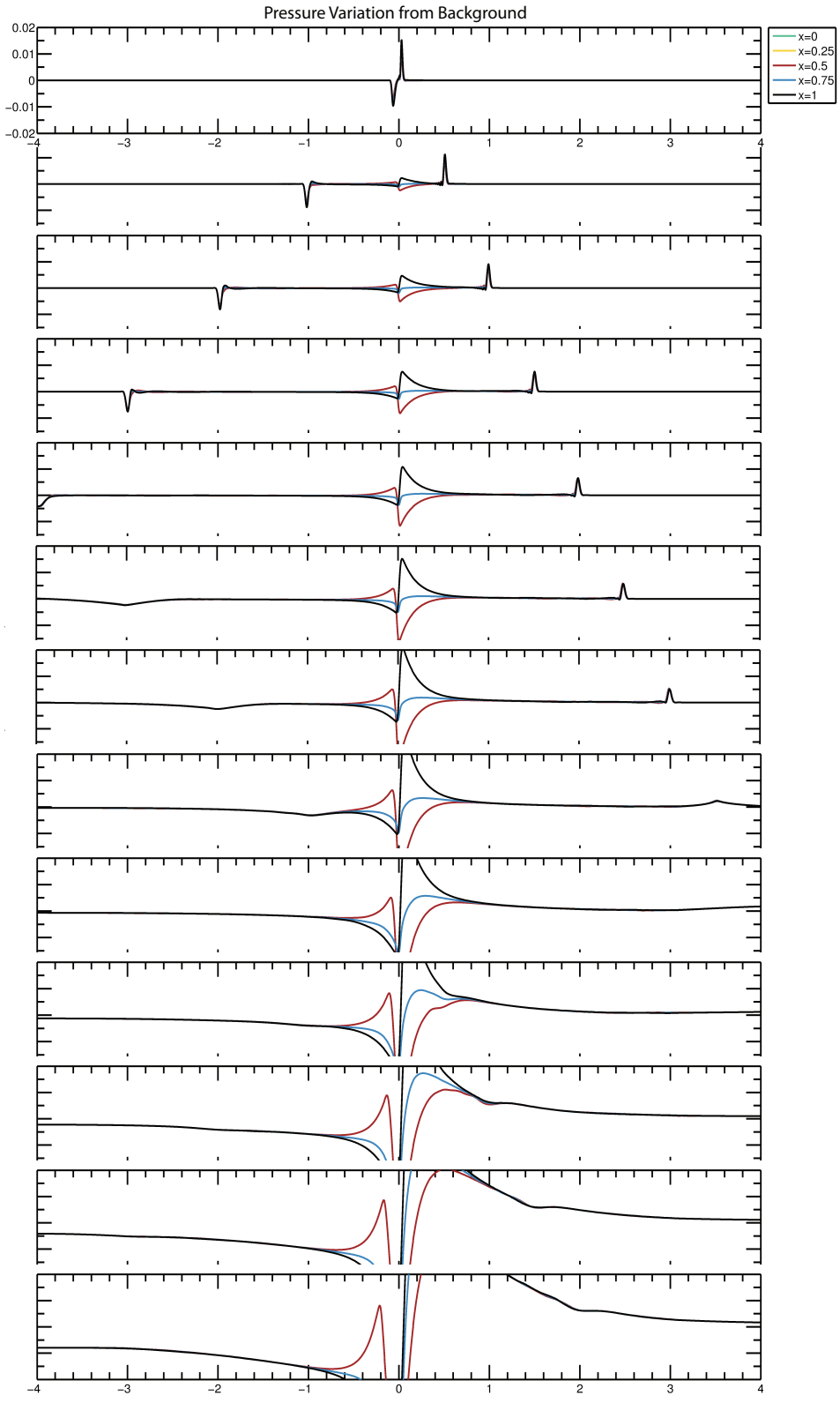

Figure 3.10: Acoustic wave propagation with a diffusion buffer layer for $|x| > 3$.

3.3.2 Non-Reflecting Boundary Conditions for Stratified Flow

The NSCBC method from Section 2.4.2 using the LODI relations introduced by Poinsot and Lele [63] requires a modification to account for stratified background states. The analysis is performed on the one-dimensional Euler equations,

$$\frac{\partial \rho}{\partial t} + \rho \frac{\partial u}{\partial x} + u \frac{\partial \rho}{\partial x} = 0, \tag{3.61}$$

$$\frac{\partial u}{\partial t} + u \frac{\partial u}{\partial x} + \frac{1}{\rho} \frac{\partial p}{\partial x} = 0, \tag{3.62}$$

$$\frac{\partial p}{\partial t} + \rho c^2 \frac{\partial u}{\partial x} + u \frac{\partial p}{\partial x} = 0. \tag{3.63}$$

The waves are approximately planar and viscous effects are not considered. Pressure and density can be decomposed into the steady hydrostatic background state and the unsteady fields as follows,

$$p(x_1, x_2, x_3, t) = p^H(x_1) + \check{p}(x_1, x_2, x_3, t), \tag{3.64}$$

$$\rho(x_1, x_2, x_3, t) = \rho^H(x_1) + \check{\rho}(x_1, x_2, x_3, t). \tag{3.65}$$

The hydrostatic quantities are equivalent to the background state from the linear stability analysis. The relationship given in (3.12) holds true for p^H and ρ^H, and both are assumed constant with time. However, the hydrostatic fields vary with x_1 everywhere, including near the boundaries. Therefore, the hydrostatic background state is removed from the pressure and density evolution terms before the characteristic equations are derived. The modified Euler equations are

$$\frac{\partial \check{\rho}}{\partial t} + \rho \frac{\partial u}{\partial x} + u \frac{\partial \check{\rho}}{\partial x} = -u \frac{\partial \rho^H}{\partial x}, \tag{3.66}$$

$$\frac{\partial u}{\partial t} + u \frac{\partial u}{\partial x} + \frac{1}{\rho} \frac{\partial \check{p}}{\partial x} = \frac{\rho^H g}{\rho}, \tag{3.67}$$

$$\frac{\partial \check{p}}{\partial t} + \rho c^2 \frac{\partial u}{\partial x} + u \frac{\partial \check{p}}{\partial x} = \rho^H g u. \tag{3.68}$$

The differential characteristic variables for this system are

$$\delta v_1 = \rho c \, \delta u - \delta \check{p}, \tag{3.69}$$

$$\delta v_2 = c^2 \, \delta \check{\rho} - \delta \check{p}, \tag{3.70}$$

$$\delta v_3 = \rho c \, \delta u + \delta \check{p}, \tag{3.71}$$

which results with the following characteristic equations:

$$\frac{\partial v_1}{\partial t} + (u-c)\frac{\partial v_1}{\partial x} = -(u-c)\rho^H g, \tag{3.72}$$

$$\frac{\partial v_2}{\partial t} + u\frac{\partial v_2}{\partial x} = u(\gamma-1)\rho^H g, \tag{3.73}$$

$$\frac{\partial v_3}{\partial t} + (u+c)\frac{\partial v_3}{\partial x} = (u+c)\rho^H g. \tag{3.74}$$

Therefore, the LODI relations are applied only to the unsteady fields, with the hydrostatic background state affecting the system through appropriate source terms in the characteristic equations. The modified wave amplitude variations are

$$\mathcal{I}_1 = \lambda_1\left(\frac{\partial \check{p}}{\partial x_1} - \rho c\frac{\partial u}{\partial x_1}\right), \tag{3.75}$$

$$\mathcal{I}_2 = \lambda_2\left(c^2\frac{\partial \check{\rho}}{\partial x_1} - \frac{\partial \check{p}}{\partial x_1}\right), \tag{3.76}$$

$$\mathcal{I}_{(3:d+1)} = \lambda_{(3:d+1)}\frac{\partial u_{2:d}}{\partial x_1}, \tag{3.77}$$

$$\mathcal{I}_{(d+2:N_s+d+1)} = \lambda_{(d+2:N_s+d+1)}\frac{\partial Y_{1:N_s}}{\partial x_1}, \tag{3.78}$$

$$\mathcal{I}_{N_v} = \lambda_{N_v}\left(\frac{\partial \check{p}}{\partial x_1} + \rho c\frac{\partial u}{\partial x_1}\right), \tag{3.79}$$

with characteristic velocities

$$\lambda_1 = u_1 - c, \tag{3.80}$$

$$\lambda_2 = \lambda_{(3:d+1)} = \lambda_{(d+2:N_s+d+1)} = u_1, \tag{3.81}$$

$$\lambda_{N_v} = u_1 + c. \tag{3.82}$$

The full system can then be written as

$$\frac{\partial \rho}{\partial t} + \left(\mathcal{X}_1 + u_1\frac{\partial \rho^H}{\partial x_1}\right) + \sum_{n=2}^{d}\frac{\partial \rho u_n}{\partial x_n} = 0, \tag{3.83}$$

$$\frac{\partial \rho u_i}{\partial t} + u_i\left(\mathcal{X}_1 + u_1\frac{\partial \rho^H}{\partial x_1}\right) + \left(\rho\mathcal{X}_{i+1} - \rho^H g_i\right) + \sum_{n=2}^{d}\frac{\partial \rho u_i u_n}{\partial x_n} = -\frac{\partial p}{\partial x_i}(1-\delta_{i1}) - \rho g_i + \frac{\partial \tau_{ij}}{\partial x_j}, \tag{3.84}$$

$$\frac{\partial \rho e}{\partial t} + \frac{1}{2}(u_j u_j)\left(\mathcal{X}_1 + u_1\frac{\partial \rho^H}{\partial x_1}\right) + \left(\rho u_j\mathcal{X}_{j+1} - \rho^H g_1 u_1\right) \tag{3.85}$$

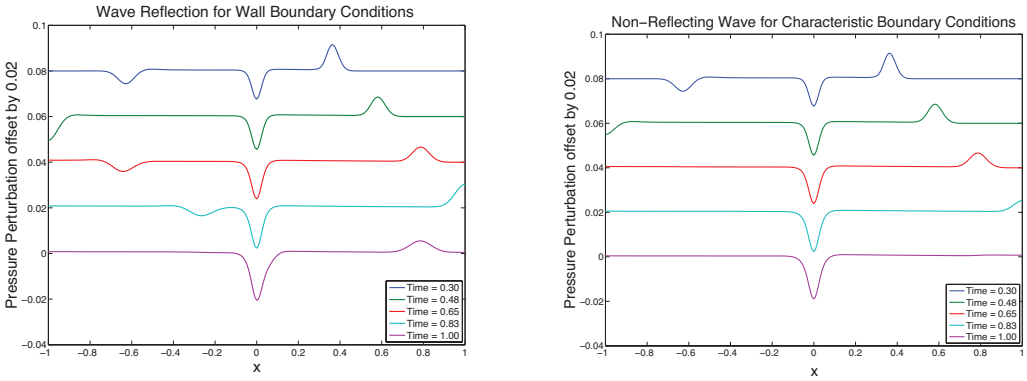

(a) NSCBC Slip Wall Conditions (b) NSCBC Non-Reflecting Conditions

Figure 3.11: The two characteristic-based boundary condition types are applied for the one-dimensional mixing in the RT unstable configuration. The pressure perturbation from the hydrostatic background is plotted at various times to show the acoustic waves approaching and reacting to the domain edges.

$$+\frac{1}{\gamma-1}\left(\mathcal{X}_{N_v}-\rho^H g_1 u_1\right)+\sum_{n=2}^{d}\frac{\partial \rho e u_n}{\partial x_n}= \\ -\sum_{n=2}^{d}\frac{\partial p u_n}{\partial x_n}-\rho u_i g_i+\frac{\partial \tau_{ij}u_i}{\partial x_j}-\frac{\partial q_j}{\partial x_j}+\frac{\partial c_{p_l} T s_{jl}}{\partial x_j}, \tag{3.86}$$

$$\frac{\partial \rho Y_l}{\partial t}+Y_l\left(\mathcal{X}_1+u_1\frac{\partial \rho^H}{\partial x_1}\right)+\rho\mathcal{X}_{l+d+1}+\sum_{n=2}^{d}\frac{\partial \rho Y_l u_n}{\partial x_n}=\frac{\partial s_{jl}}{\partial x_j}, \tag{3.87}$$

where the terms that have been added to account for stratification are colored blue. The definition for the set of $\mathcal{X}_\kappa$ is

$$\mathcal{X}_1 = \frac{1}{2c^2}(\mathcal{I}_{N_v}+\mathcal{I}_1+2\mathcal{I}_2)\left[=u_1\frac{\partial\rho}{\partial x_1}+\rho\frac{\partial u_1}{\partial x_1}\right], \tag{3.88}$$

$$\mathcal{X}_2 = \frac{1}{2\rho c}(\mathcal{I}_{N_v}-\mathcal{I}_1)\left[=u_1\frac{\partial u_1}{\partial x_1}+\frac{1}{\rho}\frac{\partial p}{\partial x_1}\right], \tag{3.89}$$

$$\mathcal{X}_{(3:d+1)} = \mathcal{I}_{(3:d+1)}\left[=u_1\frac{\partial u_{(2:d)}}{\partial x_1}\right], \tag{3.90}$$

$$\mathcal{X}_{(d+2:N_s+d+1)} = \mathcal{I}_{(d+2:N_s+d+1)}\left[=u_1\frac{\partial Y_{(1:N_s)}}{\partial x_1}\right], \tag{3.91}$$

$$\mathcal{X}_{N_v} = \frac{1}{2}(\mathcal{I}_{N_v}+\mathcal{I}_1)\left[=u_1\frac{\partial p}{\partial x_1}+\rho c^2\frac{\partial u_1}{\partial x_1}\right], \tag{3.92}$$

which is the same as in (2.135)-(2.137), but is included here for consistency.

Both the adiabatic slip wall and non-reflecting boundary conditions discussed in Sections 2.4.2.1 and 2.4.2.2 can be implemented with the modified NSCBC for stratified flow. For both

boundary condition types, the well-posedness of the system is ensured by treating the flux terms consistent with the LODI conditions. Figure 3.11 shows the two boundary condition types applied to the one-dimensional mixing of RT-unstable fluids. Acoustic waves are generated from the initial conditions due to the molecular mixing and travel outward towards the boundaries. The non-hydrostatic component of pressure is plotted at five times. Whereas the wave fully reflects with the wall condition, there is essentially no reflection when the modified characteristic conditions are applied, successfully simulating an infinite domain with a non-constant background pressure field.

The characteristics-based non-reflecting boundary conditions for stratified flows is applied to the test case and shown in Figure 3.12. In comparison with the slip wall and diffusion buffer zone cases, the non-reflecting boundaries admit no appreciable wave reflection. The small additional computational cost required to use a non-reflecting boundary condition is outweighed by its success at simulating an infinite domain with stratified fluids. For dynamically adaptive methods, complete removal of the acoustics at the boundaries prevents unnecessary adaptation on the propagating waves, leading to an efficient use of computational resources.

3.4 Time Integration Schemes

When performing time-dependent numerical simulations of fluid systems, there is no general time integration scheme that is optimal for all cases. An effective time discretization method depends on the nonlinearity of the governing equations, the diversity of terms in the equations, the stiffness of the system, stability requirements, and the required accuracy of the solution. Thus, different time integration schemes are optimal for different problems. Furthermore, various time discretization methods may be employed throughout a single simulation, as the evolution of the flow and the dynamically adaptive grid leads to temporal fluctuations of the stability requirements.

3.4.1 Implicit Schemes

Implicit time integration schemes are commonly utilized to solve the full Navier-Stokes equations, where diffusion is important. This avoids any restriction placed on the size of the time-step

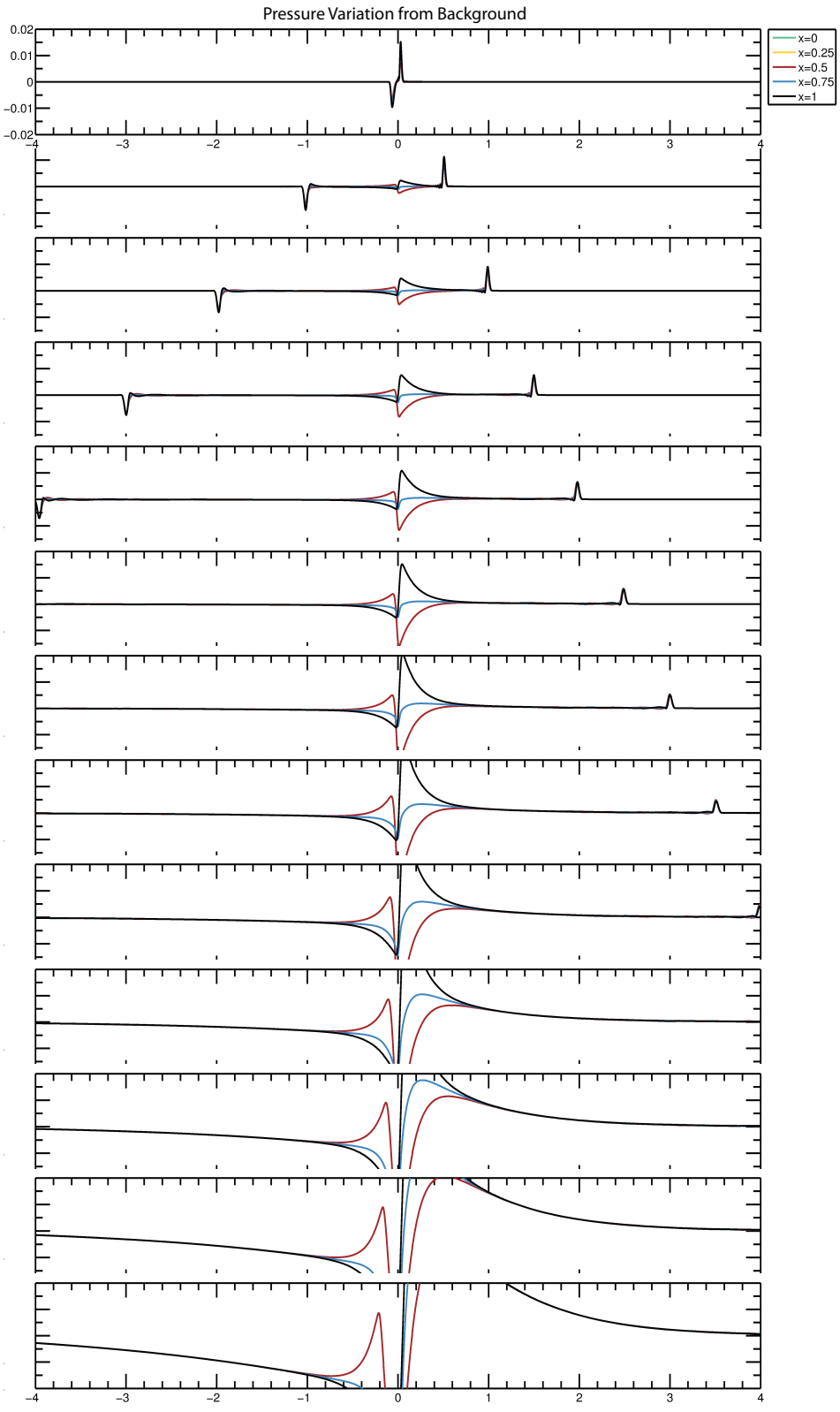

Figure 3.12: Acoustic wave propagation with non-reflecting boundaries.

for high resolution simulations, which must be considered when using an explicit time discretization. The simplified governing equations from (3.55) can be discretized using the Crank-Nicholson method as,

$$\frac{\mathbf{U}^{n+1} - \mathbf{U}^n}{\Delta t} = \frac{1}{2}\left[\mathbf{F}^n + \mathbf{F}^{n+1}\right], \tag{3.93}$$

where the superscripted quantities, $\mathbf{U}^n$ and $\mathbf{U}^{n+1}$, represent the solution at the beginning and end, respectively, of the current time step. Also, the terms on the right-hand side of the equation represent the evaluation of $\mathbf{F}(\mathbf{U})$ at the appropriate time level, that is $\mathbf{F}^n \equiv \mathbf{F}(\mathbf{U}^n)$. The Crank-Nicholson method is unconditionally stable and second-order accurate, that is, $O(\Delta t^2)$. For systems where higher accuracy is needed, preconditioned Krylov-subspace solvers are often used. Implicit methods often use a linearization of the discretized equations and require an iterative scheme, such as the preconditioned biconjugate gradient stabilized (BiCGSTAB) method, to handle nonlinearity in the system. When PAWCM is used, a multilevel method, similar to the multigrid method but on an adaptive grid, can optimize the iterative process within the BiCGSTAB method. However, for highly nonlinear systems, where the hyperbolic terms in the governing equations are significant, the convergence of the iterative process is not predictable, making the use of implicit time integration methods inefficient.

3.4.2 Explicit Schemes

When using implicit schemes, the Courant-Friedrichs-Lewy (CFL) stability condition must be satisfied when nonlinearities in the system are significant. The convective-acoustic CFL condition is

$$\frac{(U + c)\Delta t}{\Delta x} \leq \mathcal{C}, \tag{3.94}$$

where U is the local absolute fluid velocity, c is the local speed of sound, and $\mathcal{C}$ is the CFL coefficient that depends on the discretization scheme. Typically, $\mathcal{C} \leq 1$, where the maximum allowed time step size is directly proportional to $\mathcal{C}$. For cases where the CFL condition is stricter than any of the diffusion stability requirements when setting the time step size, explicit time integration schemes

are the optimal choice. The fully explicit Runge-Kutta (ERK) scheme,

$$\mathbf{U}^* = \mathbf{U}^n + \Delta t \mathbf{F}^n, \tag{3.95}$$

$$\mathbf{U}^{n+1} = \frac{1}{2}\mathbf{U}^n + \frac{1}{2}\mathbf{U}^* + \frac{1}{2}\Delta t \mathbf{F}^*, \tag{3.96}$$

where $\mathbf{U}^*$ represents the solution at an intermediate time level, is second-order accurate, that is $O(\Delta t^2)$, and total variation diminishing (TVD) [80]. TVD schemes are successful at simulating the propagation of shock waves while preserving monotonicity. A TVD time integration scheme is a good choice for simulations of compressible RTI, due to the presence of sharp acoustic waves, especially when the molar mass difference is large and the stratification is strong. The second-order TVD Runge-Kutta scheme can also be written as

$$\mathbf{U}^* = \mathbf{U}^n + \Delta t \mathbf{F}^n, \tag{3.97}$$

$$\mathbf{U}^{n+1} = \mathbf{U}^n + \frac{\Delta t}{2}\left[\mathbf{F}^n + \mathbf{F}^*\right]. \tag{3.98}$$

A third-order, that is $O(\Delta t^3)$, fully explicit TVD Runge-Kutta scheme is

$$\mathbf{U}^* = \mathbf{U}^n + \Delta t \mathbf{F}^n, \tag{3.99}$$

$$\mathbf{U}^{**} = \frac{3}{4}\mathbf{U}^n + \frac{1}{4}\mathbf{U}^* + \frac{1}{4}\Delta t \mathbf{F}^*, \tag{3.100}$$

$$\mathbf{U}^{n+1} = \frac{1}{3}\mathbf{U}^n + \frac{2}{3}\mathbf{U}^{**} + \frac{2}{3}\Delta t \mathbf{F}^{**}, \tag{3.101}$$

where $\mathbf{U}^*$ and $\mathbf{U}^{**}$ are the solutions at intermediate time levels [80]. This scheme has a low storage requirement because the evaluations of $\mathbf{F}(\mathbf{U})$ are always taken at the current intermediate time level. The third-order TVD ERK scheme can also be written as

$$\mathbf{U}^* = \mathbf{U}^n + \Delta t \mathbf{F}^n, \tag{3.102}$$

$$\mathbf{U}^{**} = \mathbf{U}^n + \frac{\Delta t}{4}\left[\mathbf{F}^n + \mathbf{F}^*\right], \tag{3.103}$$

$$\mathbf{U}^{n+1} = \mathbf{U}^n + \frac{\Delta t}{6}\left[\mathbf{F}^n + \mathbf{F}^* + 4\mathbf{F}^{**}\right]. \tag{3.104}$$

Both of the TVD ERK schemes have a CFL coefficient of unity.

3.4.3 Implicit-Explicit Schemes

The use of a fully explicit time integration scheme is unreasonable for high resolution simulations of a fluid system where viscous and diffusion effects are significant, due to strict stability requirements from the diffusion terms. However, fully implicit schemes may also be inefficient due to the need to iterate on the nonlinear hyperbolic terms. A third option is to discretize each term individually in order to take full advantage of the benefits of implicit and explicit methodology, while eliminating many of the drawbacks. Implicit-explicit (IMEX) Runge-Kutta schemes combine diagonally implicit Runge-Kutta (DIRK) and ERK schemes [6]. The hyperbolic and parabolic terms are grouped separately, such that $\mathbf{F}(\mathbf{U}) = \mathbf{H}(\mathbf{U}) + \mathbf{P}(\mathbf{U})$, and the generalized governing equations from (3.55) are rewritten as

$$\frac{\partial \mathbf{U}}{\partial t} = \mathbf{H}(\mathbf{U}) + \mathbf{P}(\mathbf{U}). \tag{3.105}$$

The hyperbolic part, $\mathbf{H}(\mathbf{U})$, corresponds to the convection, pressure gradient, and body force terms. The remaining diffusion terms make up the parabolic part, $\mathbf{P}(\mathbf{U})$. Systems with negligible diffusive effects ($\mathbf{P} \approx 0$) are generally nonlinear, but not too stiff. Conversely, diffusion dominated systems ($\mathbf{H} \approx 0$) tend to be highly stiff, but mostly linear. Thus, IMEX schemes use an ERK method for the discretization of $\mathbf{H}(\mathbf{U})$ and a DIRK method for $\mathbf{P}(\mathbf{U})$, while optimizing the DIRK attenuation properties and the combined stability regions. The required number of iterations is often small during the implicit steps of these IMEX schemes, especially when using efficient iterative solvers, such as the multilevel BiCGSTAB method performed on an adaptive grid while using PAWCM. However, since an implicit stage is more expensive then an explicit step, IMEX schemes are developed to reduce the number of implicit steps while maintaining the required order of accuracy.

A single-stage DIRK scheme is combined with a two-stage ERK method to form a second-order IMEX scheme as [6],

$$\mathbf{U}^* = \mathbf{U}^n + \frac{\Delta t}{2}\left[\mathbf{H}^n + \mathbf{P}^*\right], \tag{3.106}$$

$$\mathbf{U}^{n+1} = \mathbf{U}^n + \Delta t\left[\mathbf{H}^* + \mathbf{P}^*\right]. \tag{3.107}$$

Applying the test equation, $\partial U/\partial t = \lambda U$, to this DIRK method, with $z = \lambda \Delta t$, the convergence factor in the stiffness limit of $z \to -\infty$ is $R(\infty) = 1$, which corresponds to no attenuation. However, the scheme is A-stable, since $|R(z)| \leq 1$ for $\mathrm{Re}(z) \leq 0$.

A similar second-order IMEX scheme can be derived by combining the two-stage TVD ERK method from (3.97)-(3.98) with a Crank-Nicholson single-stage implicit method as,

$$\mathbf{U}^* = \mathbf{U}^n + \frac{\Delta t}{2}\left[2\mathbf{H}^n + \mathbf{P}^n + \mathbf{P}^*\right], \tag{3.108}$$

$$\mathbf{U}^{n+1} = \mathbf{U}^n + \frac{\Delta t}{2}\left[\mathbf{H}^n + \mathbf{P}^n + \mathbf{H}^* + \mathbf{P}^*\right]. \tag{3.109}$$

Whereas this combination has the benefits of a TVD explicit scheme and an A-stable implicit scheme, there is no attenuation in the stiffness limit.

A third-order IMEX scheme using a two-stage, A-stable DIRK and a three-stage ERK method is [6],

$$\mathbf{U}^* = \mathbf{U}^n + \Delta t\gamma\left[\mathbf{H}^n + \mathbf{P}^*\right], \tag{3.110}$$

$$\mathbf{U}^{**} = \mathbf{U}^n + \Delta t\left[(\gamma - 1)(\mathbf{H}^n - 2\mathbf{H}^*) + (1 - 2\gamma)\mathbf{P}^* + \mathbf{P}^{**}\right], \tag{3.111}$$

$$\mathbf{U}^{n+1} = \mathbf{U}^n + \frac{\Delta t}{2}\left[\mathbf{H}^* + \mathbf{P}^* + \mathbf{H}^{**} + \mathbf{P}^{**}\right], \tag{3.112}$$

where $\gamma = (3 + \sqrt{3})/6$. This method has some attenuation of the stability function in the stiffness limit, since $|R(\infty)| = 0.7321$.

The three-stage TVD ERK scheme from (3.102)-(3.104) is combined with a two-stage DIRK method to produce a second-order IMEX scheme as,

$$\mathbf{U}^* = \mathbf{U}^n + \Delta t\left[\mathbf{H}^n + \mathbf{P}^*\right], \tag{3.113}$$

$$\mathbf{U}^{**} = \mathbf{U}^n + \frac{\Delta t}{4}\left[\mathbf{H}^n + \mathbf{H}^* - 2\mathbf{P}^* + 4\mathbf{P}^{**}\right], \tag{3.114}$$

$$\mathbf{U}^{n+1} = \mathbf{U}^n + \frac{\Delta t}{6}\left[\mathbf{H}^n + \mathbf{H}^* + 4\mathbf{H}^{**} + 6\mathbf{P}^{**}\right]. \tag{3.115}$$

The attenuation is even stronger with this A-stable method, since $|R(\infty)| = 0.5$.

For highly-stiff problems, it is important that the discretization is L-stable, which combines A-stability with full attenuation in the stiffness limit, that is $|R(\infty)| = 0$. A second-order IMEX

scheme that combines a two-stage, L-stable DIRK and a three-stage ERK method is [6],

$$\begin{aligned}
\mathbf{U}^{*} &= \mathbf{U}^{n} + \Delta t\gamma\left[\mathbf{H}^{n} + \mathbf{P}^{*}\right], && (3.116)\\
\mathbf{U}^{**} &= \mathbf{U}^{n} + \Delta t\left[\delta\mathbf{H}^{n} + (1-\delta)\mathbf{H}^{*} + (1-\gamma)\mathbf{P}^{*} + \gamma\mathbf{P}^{**}\right], && (3.117)\\
\mathbf{U}^{n+1} &= \mathbf{U}^{n} + \Delta t\left[(1-\gamma)(\mathbf{H}^{*} + \mathbf{P}^{*}) + \gamma(\mathbf{H}^{**} + \mathbf{P}^{**})\right], && (3.118)
\end{aligned}$$

where $\gamma = (2-\sqrt{2})/2$ and $\delta = -2\sqrt{2}/3$.

The previous IMEX schemes all include an additional explicit step following the final implicit stage. Identifying the last internal stage with the solution at the next time step ensures L-stability and is particularly good for highly-stiff problems. A second-order IMEX scheme using a two-stage, L-stable DIRK scheme and a two-stage ERK method is [6],

$$\begin{aligned}
\mathbf{U}^{*} &= \mathbf{U}^{n} + \Delta t\gamma\left[\mathbf{H}^{n} + \mathbf{P}^{*}\right], && (3.119)\\
\mathbf{U}^{n+1} &= \mathbf{U}^{n} + \Delta t\left[\delta\mathbf{H}^{n} + (1-\delta)\mathbf{H}^{*} + (1-\gamma)\mathbf{P}^{*} + \gamma\mathbf{P}^{n+1}\right], && (3.120)
\end{aligned}$$

where $\gamma = (2-\sqrt{2})/2$ and $\delta = 1 - 1/(2\gamma)$.

A second-order IMEX method results from the combination of the three-stage TVD ERK scheme from (3.102)-(3.104) and a three-stage, L-stable DIRK method as,

$$\begin{aligned}
\mathbf{U}^{*} &= \mathbf{U}^{n} + \Delta t\left[\mathbf{H}^{n} + \mathbf{P}^{*}\right], && (3.121)\\
\mathbf{U}^{**} &= \mathbf{U}^{n} + \frac{\Delta t}{4}\left[\mathbf{H}^{n} + \mathbf{H}^{*} - 2\mathbf{P}^{*} + 4\mathbf{P}^{**}\right], && (3.122)\\
\mathbf{U}^{n+1} &= \mathbf{U}^{n} + \frac{\Delta t}{6}\left[\mathbf{H}^{n} + \mathbf{H}^{*} + 4\mathbf{H}^{**} - 6\mathbf{P}^{*} + 6\mathbf{P}^{**} + 6\mathbf{P}^{n+1}\right]. && (3.123)
\end{aligned}$$

The cost of an additional implicit step should be weighed against the need of a TVD explicit method and a L-stable implicit scheme.

Chapter 4

Simulations of Single-Mode Rayleigh-Taylor Instability

Until recently, reaching and maintaining a terminal velocity was thought to be the late time behavior of the Rayleigh-Taylor instability (RTI) system where only a single wavelength perturbation is introduced [34]. This conclusion was supported by experimental and theoretical results, which temporarily closed the book on the single-mode RTI system. Furthermore, it was concluded that the single-mode case had little impact on a thorough understanding of the multi-mode RTI system. It is now known that the vortical motions generated due to the density jump play a dominant role in the late-time evolution of the bubbles and spikes, and that the velocity is far from constant [89]. Furthermore, the dynamics of the single-mode case contain valuable insights for the multimode case. Specifically, the single-mode growth is an upper bound for the multimode mixing layer.

Similarly, most of the current research on RTI focuses solely on the incompressible case. RTI can be observed in a wide range of astrophysical and atmospheric flows [28, 74] and has drastic effects on many engineering systems of interest, such as inertial confinement fusion [43, 44]. The majority of the systems where RTI naturally occurs involve highly compressible fluids. Of particular interest is the crucial role Rayleigh-Taylor mixing plays during the thermonuclear flame front acceleration in type Ia supernovae [9]. The compressibility effects during this violent expansion are potentially drastic. Thus, a detailed understanding of the compressibility effects on the growth of RTI is necessary. Linear stability theory has shown that there is no unique parameter characterizing compressibility [53]. Acoustic effects, material properties, and background stratification can all

affect the instability growth, often in opposed ways. At late times, as the nonlinear effects become important, the number of these parameters is only expected to increase and their interactions to become even more complicated.

An investigation of compressible RTI requires the use of efficient numerical methods, advanced boundary conditions, and a consistent initialization in order to capture the wide range of scales present in the system while reducing the computational impact associated with acoustic wave generation and the subsequent interaction with the flow. Numerical simulations are performed on an adaptive mesh using the Parallel Adaptive Wavelet Collocation Method (PAWCM). The combined effects of compressibility and large density variations on the late-time behavior of RTI is not currently fully understood [30, 56]. For thermal equilibrium, acoustic and stratification properties of the background flow are interrelated, with stratification itself playing an important role. In order to capture the late time behavior, simulations need to be performed in long vertical domains, with density ranges spanning many orders of magnitude. The utilization of PAWCM for simulations on such domains minimizes the computational effort, since Rayleigh-Taylor instability remains a spatially localized phenomenon near the interface well into the turbulent stage.

A thorough investigation of the single-mode RTI is presented in the following sections. The parameters and computational methodologies that are held consistent throughout all cases are presented first. Then, simulations run in the incompressible limit are compared against well established results. The compressibility effects on the growth of RTI are then discussed, with a focus on the background stratification and vortex dynamics. Finally, low-resolution three-dimensional cases are presented to look at the dimensional dependence of the compressibility effects.

4.1 Implementation of the Parallel Adaptive Wavelet Collocation Method

In this study, direct numerical simulations are performed using the PAWCM within the advanced computational framework discussed in Chapter 3. Once the significant wavelets are flagged, in addition to the adjacent zone, required for resolving flow evolution, and the reconstruction check, a symmetry check is applied to ensure the grid remains symmetric around the centerline of the bub-

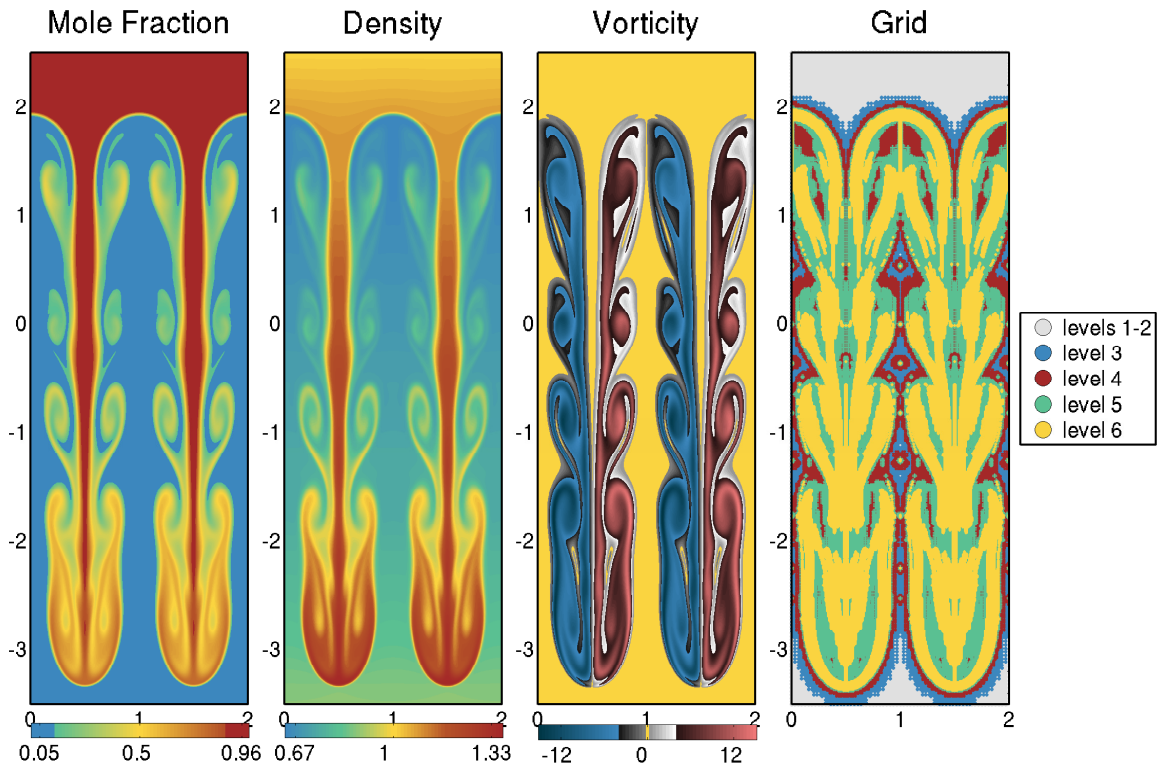

Figure 4.1: Mole fraction, density, vorticity, and the associated adaptive grid for the late-time instability growth with $M = 0.3$ and $A = 0.3$.

bles and spikes. Ensuring the grid is symmetric leads to stable simulations with longer durations. The solution itself is not forced to be symmetric, but only the grid. A half wavelength instability can be studied with mirror boundary conditions, which ensures the solution is symmetric. However, simulating the full wavelength acts as an accuracy check on the implementation of the numerical method. A typical dynamically adapted grid with the symmetry check applied is shown in Figure 4.1 for a late-time RTI simulation. The effective global resolution is 8193×512, yet only 16.5% of the points are used (690,318 points, 83.5% compression). The initialization for the perturbed fields can be applied to the thermodynamic variables on a perturbed interface, or equivalently to the velocity field on a flat interface. The latter option leads to longer durations with symmetric solutions for the single-mode case. Thus, velocity perturbations are applied as the initial conditions.

The domain is periodic in the horizontal (x_2) direction. Either a diffusion buffer zone or the characteristics-based non-reflecting boundary conditions are utilized in the vertical direction.

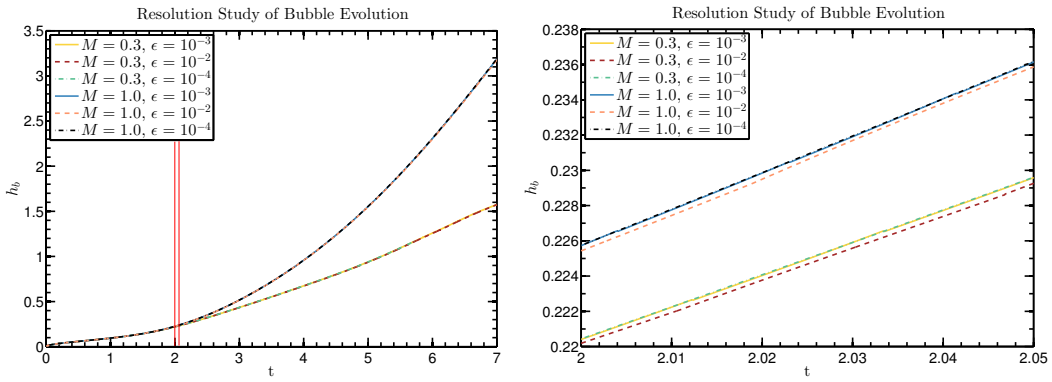

(a) Full Evolution (b) Zoomed-In View

Figure 4.2: Resolution convergence study where the threshold parameter ϵ is varied. A zoomed view, corresponding to the region between the two vertical red lines, is presented for clear observation of the line variability for the high-ϵ cases. $A = 0.7$ for all cases.

The diffusion layer zone is the more computationally efficient technique, while the non-reflecting boundary conditions presented in Section 3.3.2 have the least wave reflection.

Grid adaptation can be done in different ways. One way is simply to adapt on each integrated variable. Another method, used in this work, involves adaptation on additional dynamically important physical quantities, which ensures adequate resolution of the flow structures that control the dynamics of the flow evolution. The adapted variables are the heavy fluid mass fraction and its gradient, the velocity field, vorticity, and strain rate.

The Runge-Kutta schemes introduced in Section 3.4 are used for time integration. When using an explicit method, the time integration stability requirements for every term must be satisfied. Since long vertical domains are used with strongly stratified fluids, a constant kinematic viscosity, ν, is applied in each pure fluid. Using a constant dynamic viscosity, μ, which is the true fluid property, leads to extremely restrictive stability requirements where the density values are very small, namely near the top of the domain.

4.1.1 Resolution Convergence Studies

Traditionally, the resolution studies for PAWCM are performed by increasing and decreasing the threshold parameter, ϵ, while adjusting the maximum level of resolution and the number of

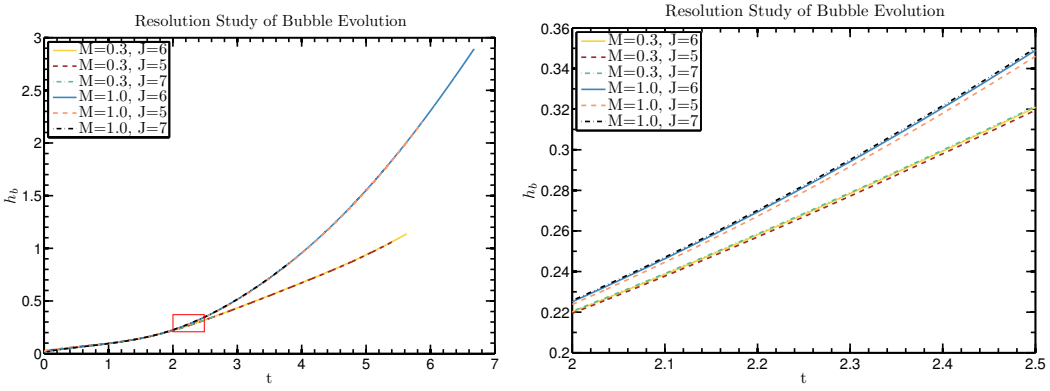

(a) Full evolution (b) Zoomed-In View

Figure 4.3: The results of the resolution study are shown for the entire bubble height evolution, as well as for a small window near the separation of the two bubble height line plots, corresponding to the red box. J is the maximum number of resolution levels. For all cases, $A = 0.7$ and $\epsilon = 10^{-3}$.

wavelets used to represent the solution. The resolution convergence study is presented in two ways. First, the threshold parameter, ϵ, is varied with a fixed maximum level of resolution. Since the RTI simulations are initialized with an interface that is as sharp as the grid will allow, all available levels of resolution are initially filled. After the interface has diffused, wavelets on the higher levels of resolution may be left out of the solution. As seen in Figure 4.2, the lines corresponding to the $\epsilon = 10^{-3}$ and $\epsilon = 10^{-4}$ cases lie on top of one another. Thus, the solution is assumed to be converged at $\epsilon = 10^{-3}$. The variability for $\epsilon = 10^{-2}$ is small, but noticeable. The threshold parameter is set to $\epsilon = 10^{-3}$ for all cases presented here.

In order to ensure that the maximum level of resolution is sufficient, a second resolution study is performed by increasing and decreasing the effective resolution, while keeping ϵ constant. When the maximum level, J, is increased by one, the effective resolution increases by a factor of two in each dimension. The results of the resolution study for the $A = 0.7$ case are presented in Figure 4.3. The solution is clearly converged as the effective resolution increases.

4.1.2 Simulation Parameters

Whereas a complete understanding of RTI requires a thorough investigation of all the parameters that may affect the instability growth, the work presented here focuses on the compressibility

and variable density effects. The Atwood numbers range from $A = 0.1$ to $A = 0.9$. The Mach numbers of interest are $M = 0.1$, which well represents the incompressible limit, to $M = 1.5$. To ensure the domain can support the late time growth of RTI, the vertical axis is extended to $x_1 = \pm 8$. The $M = 1.0$ cases have density values that span seven orders of magnitude, while the $M = 1.5$ cases have a density range over fifteen orders. Thus, the density stratification adds a layer of complexity to simulations of compressible RTI.

The viscosity is set based on the perturbation Reynolds number,

$$Re_p = \sqrt{\frac{Ag\lambda^3}{(1+A)\nu^2}}, \tag{4.1}$$

which is the best measure of viscous effects when the various Atwood number is varied. The typical value used is $Re_p = 5000$, but $Re_p = 1500$ and $Re_p = 10000$ cases are used to test the effect of the Reynolds number. The other dimensionless parameters are held constant at $Sc = 1.0$ and $Pr = 1.0$. The compressibility effect from the ratio of specific heats has been removed from the definition of the Mach number. The pure fluid values are $\gamma_1 = \gamma_2 = 1.4$. The initial diffusion layer thickness is chosen such that 32 points lie across the interface at the maximum level of resolution. This ensures the initial conditions are well resolved. The simulations show a diffusion growth regime as the first stage of RTI growth, which proves that the initial layer is not too large. The initial perturbation amplitude is chosen to be as small as possible, while still significantly larger than the initial diffusion layer thickness. In practice, the initial amplitude is set to $\eta_A = 0.005$.

4.2 Simulations of Incompressible Rayleigh-Taylor Instability

The incompressible single-mode RTI system is well researched, and a recent study has classified the stages of growth as follows [89]:

- DG - diffusive growth (species diffusion)
- EG - exponential growth (described by linear stability theory)
- PFG - potential flow growth (until terminal velocity is reached)

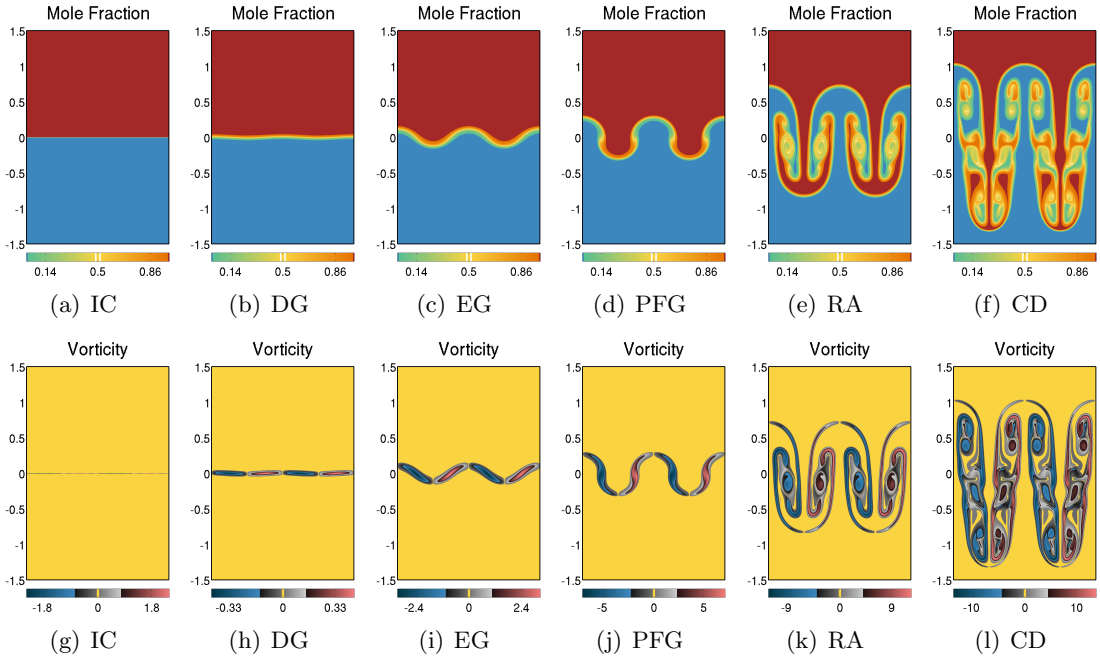

Figure 4.4: The stages of incompressible RTI are labeled as: IC - initial conditions, DG - diffusive growth, EG - exponential growth described by linear stability thoery, PFG - potential flow growth, RA - reacceleration, and CD - chaotic development.

- RA - reacceleration (induced flow from vortical motions)
- CD - chaotic development (mean quadratic growth)

Diffusion dominates early, while the perturbation, too small to have any effect yet, begins to grow exponentially consistent with linear stability theory. Once the structures begin approaching the theoretical terminal velocities, they experience a deceleration as vortical structures are created along the interface. The vortex pair interacts with the bubbles and spikes and induces motion to reaccelerate the instability growth. In the extremely late times, a chaotic development is observed, where vortices interact with each other to produce rapid acceleration and deceleration of the bubble and spikes. The late time velocity is observed to fluctuate around a mean value that grows quadratically. The five stages of RTI growth (with the initial conditions as an additional step) are displayed in Figure 4.4. From the mole fraction images, the locations of the interface and the pure fluids can be observed. The vorticity at each stage is also provided. At the end of the potential

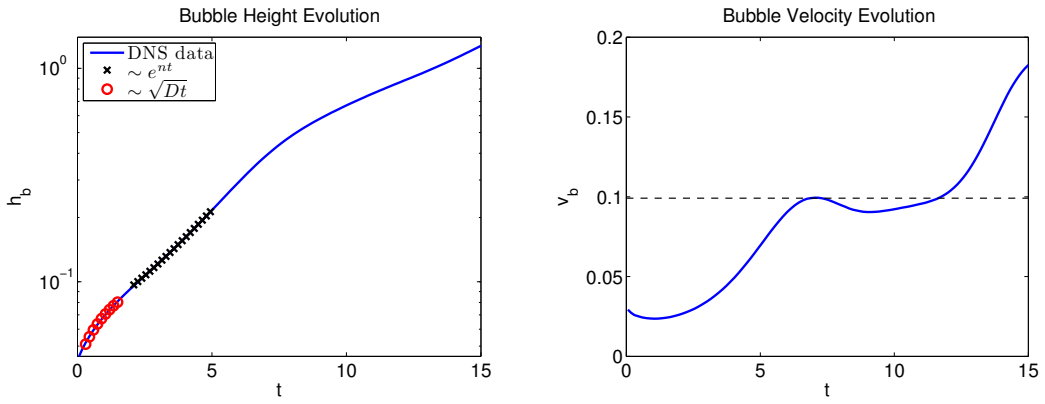

(a) Bubble Height Evolution

(b) Bubble Velocity Evolution

Figure 4.5: Bubble height and velocity for $A = 0.1$ and $M = 0.2$. The red circles represent diffusive growth and the black crosses match the exponential growth predicted by linear stability theory. The dotted line in the bubble velocity plot represents the terminal bubble velocity, V_b^*, from the potential flow analysis.

flow growth stage, the vortex generation becomes significant, leading to a vortex pair that drives the reacceleration. The late-time chaotic development is characterized by numerous vortex pairs influencing the bubble and spike tips and interacting with each other.

As a feasibility study, simulations of the incompressible case ($M = 0.2$) has shown that PAWCM successfully captures the linear regime, bubble and spike formations, and late-time flow characteristics for the single-mode perturbation case [71]. Early-time and late-time plots of the mass fraction, vorticity, vertical velocity, and adaptive grid for the incompressible case are shown in Figures 2.21 and 2.22. The bubble height and velocity plots for the $A = 0.1$ case are shown in Figure 4.5. The early-time diffusive and exponential growth stages are matched in the plot, where the linear solution is approximated using the diffusive and viscous formula (2.12). This formula yields similar results to those obtained numerically in [30]. For the values considered here, diffusive and viscous effects on the linear growth rate account for a 30% decrease from the incompressible, immiscible result in (2.11). Compressibility has less than a 2% influence on the linear growth rate. Once the bubble reaches the asymptotic velocity, signified by the horizontal dotted line, a brief deceleration is observed, followed by a reacceleration region [68]. Due to the viscous effects and limited duration of the simulation, the chaotic development is not observed for this case.

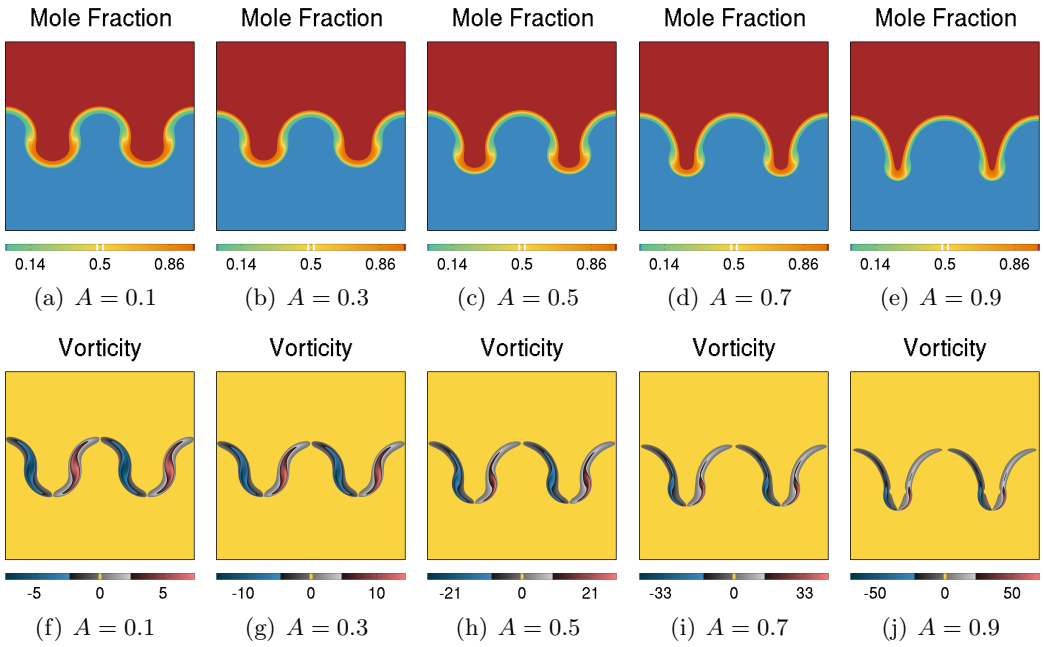

(a) $A = 0.1$ (b) $A = 0.3$ (c) $A = 0.5$ (d) $A = 0.7$ (e) $A = 0.9$

(f) $A = 0.1$ (g) $A = 0.3$ (h) $A = 0.5$ (i) $A = 0.7$ (j) $A = 0.9$

Figure 4.6: The spike and bubble shapes are compared across the range of Atwood numbers. This is a $M = 0.1$ case, which well represents incompressible flow.

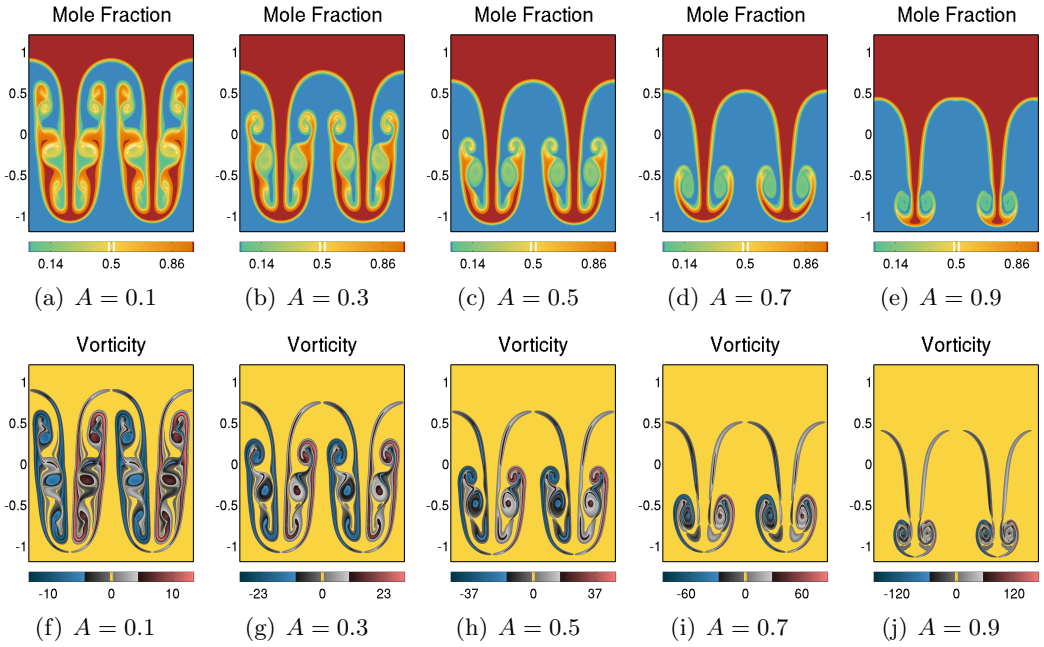

(a) $A = 0.1$ (b) $A = 0.3$ (c) $A = 0.5$ (d) $A = 0.7$ (e) $A = 0.9$

(f) $A = 0.1$ (g) $A = 0.3$ (h) $A = 0.5$ (i) $A = 0.7$ (j) $A = 0.9$

Figure 4.7: Late-time spike and bubble shapes for various Atwood numbers. The $M = 0.3$ case is presented here, which is near the limit for incompressibility.

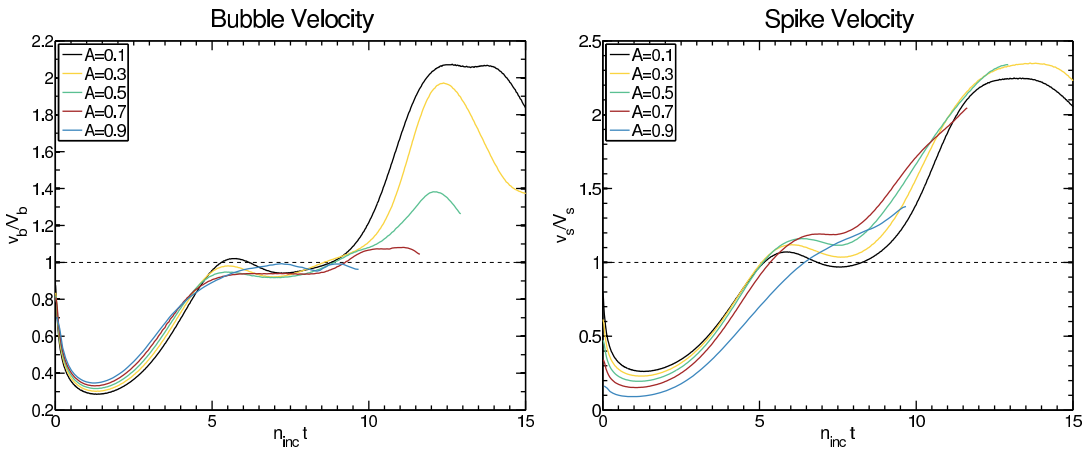

(a) Bubble Velocity A-Dependence (b) Spike Velocity A-Dependence

Figure 4.8: Bubble and spike velocity normalized by the asymptotic values derived from potential flow analysis. The horizontal axis is time normalized using the exponential growth rate from linear stability theory. The dotted lines are at unity, where the velocity matches the theoretical terminal velocity.

Labeling the structures as bubbles and spikes is not representative of the low-A case, since the two sides of the interface are mostly symmetrical. As the density difference of the two pure fluids is increased, the heavy fluid falls in a sharper and more narrow fashion, as observed in Figure 4.6. The light fluid simultaneously rises in a more rounded and smooth way. Thus, the bubble and spike names fit at moderate to high Atwood numbers. The Atwood-dependent shape effect is observed early on during the linear growth (Figure 4.6) and has drastic consequences on the late-time instability development, as seen in Figure 4.7. The narrowness of the spike is intensified as A is increased. In order to maintain an equal volume of each fluid, the bubbles become wider and flatter at higher A.

The vorticity plots in Figures 4.6 and 4.7 show that as the density difference increases, the vorticity generated also grows in intensity. Furthermore, whereas the vortices are generated near the horizontal centerline for the low-A case, the vortex creation occurs near the bubble tip for the high-A cases.

The Atwood number dependence on the asymptotic velocity that the bubble and spike achieve before decelerating is well predicted by the potential flow analysis. Figure 4.8 plots the evolution of

the bubble and spike velocity, normalized by the asymptotic values, that is v_b/V_b and v_s/V_s. Time is normalized using the exponential growth rate from linear stability theory for the incompressible case. The normalized velocity is near unity for all cases. The PAWCM simulations of the incompressible single-mode RTI successfully capture all stages of the instability growth, while utilizing computational resources efficiently.

4.3 Compressibility Effects on Rayleigh-Taylor Instability

The compressibility effects on RTI growth is closely tied to the background stratification for the thermal equilibrium case. The Mach number not only represents the intrinsic compressibility of the fluids by scaling the interfacial pressure, but also has a direct effect on the vertical variations in density. As shown in Figure 3.1, the molar mass difference between the two fluids plays a secondary role in setting the differences in the background density profiles of the two fluids. At low-A, any increase in M affects the stratification in both fluids similarily. However, at high-A, increasing M has drastic effects on the density profile in the heavy fluid, while having minimal effect on the light fluid.

A set of PAWCM simulations is presented in Figure 4.9. Each row represents a constant Atwood number, with bubble height, spike height, bubble velocity, and spike velocity displayed in each columns one through four, respectively. The Mach number dependence is plotted in each image.

The differences in the exponential growth matches the compressible dependence on growth rate obtained using linear stability analysis. The compressible effects on the linear growth rate has a larger impact at low-A. For example, increasing M from 0.1 to 1.0 decreases the growth rate by 10.7% at $At = 0.1$, but only decreases n_{com} by 4.1% at $At = 0.3$ and 1.8% at $At = 0.7$. This effect can be seen most clearly in the bubble velocity plots, where there is an obvious differences in the linear growth rate at $At = 0.1$, but almost no difference for $At \geq 0.5$

The behavioral differences observed in the exponential growth regime extend to the later stages. For low-A, the decrease in the linear growth as M increases leads to a decrease in the

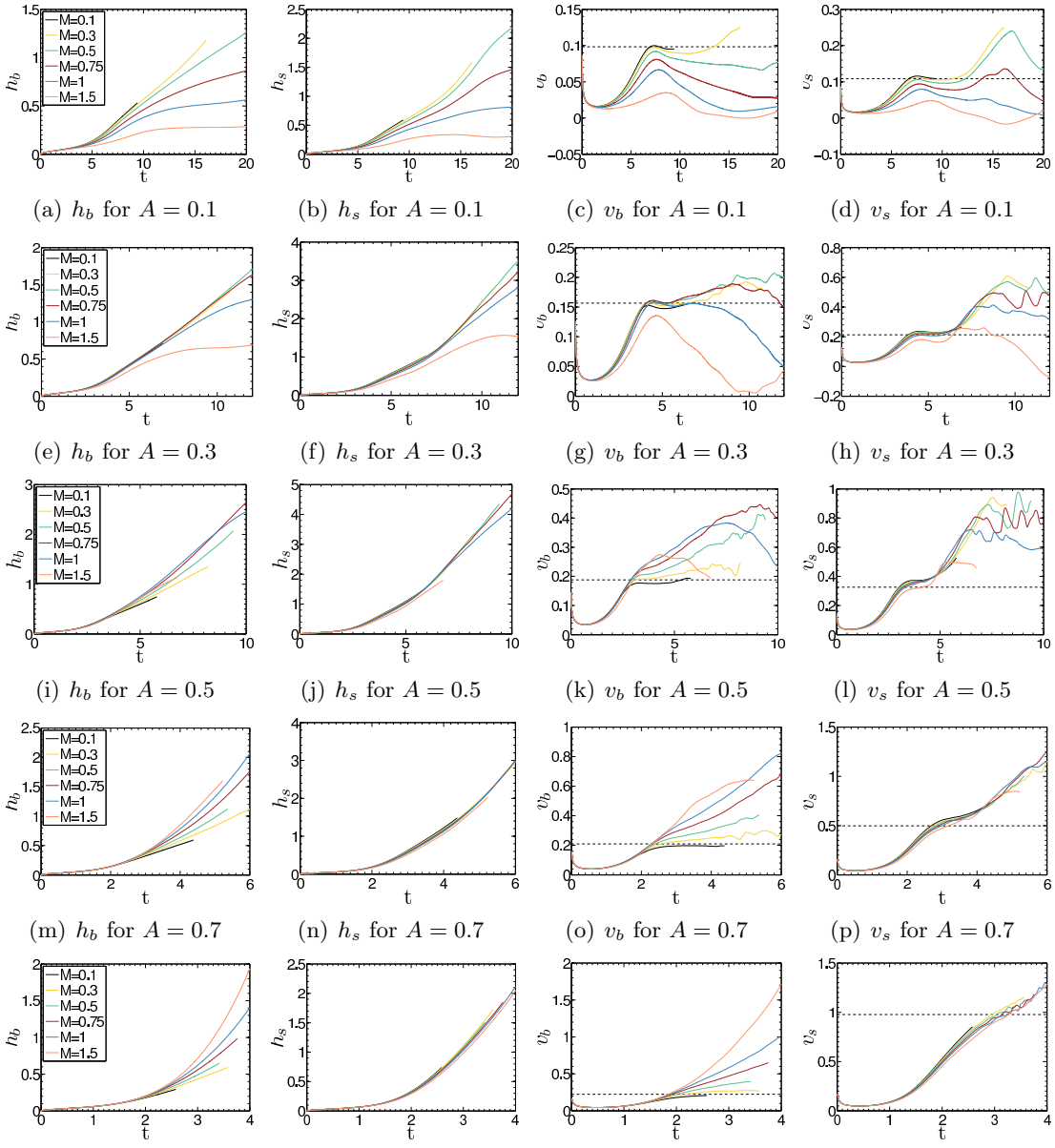

(a) h_b for $A = 0.1$ (b) h_s for $A = 0.1$ (c) v_b for $A = 0.1$ (d) v_s for $A = 0.1$

(e) h_b for $A = 0.3$ (f) h_s for $A = 0.3$ (g) v_b for $A = 0.3$ (h) v_s for $A = 0.3$

(i) h_b for $A = 0.5$ (j) h_s for $A = 0.5$ (k) v_b for $A = 0.5$ (l) v_s for $A = 0.5$

(m) h_b for $A = 0.7$ (n) h_s for $A = 0.7$ (o) v_b for $A = 0.7$ (p) v_s for $A = 0.7$

(q) h_b for $A = 0.9$ (r) h_s for $A = 0.9$ (s) v_b for $A = 0.9$ (t) v_s for $A = 0.9$

Figure 4.9: The M-dependence of the evolutions of bubble height, h_b (far left column), spike height, h_s (second column), bubble velocity, v_b (third column), and spike velocity, v_s (far right column) are shown for various A (rows). The dotted line represents the asymptotic velocity values from potential flow theory.

transitional constant bubble velocity, and an overall suppression of the instability growth. At high-A, a transitional constant bubble velocity never occurs.

On the spike side of the interface, the differences continue between low and high Atwood cases. For low-A, the behavior is similar to its bubble counterpart, where the constant velocity and the overall growth is suppressed as compressibility is increased. However, for high-A, the spike behavior converges for all M. At late times, a spike reacceleration occurs and leads into chaotic development.

There is a drastic change in the monotonic behavior of the RTI growth as M increases when different Atwood regimes are considered. Compressibility and stratification act to suppress the growth when small molar mass differences are involved. Alternatively, for large molar mass differences, an enhancement in the growth occurs when compressibility and stratification increase.

The change in behavior occurs during different stages of the instability growth. For low-A, the suppression occurs during the early exponential growth, because the growth rate is strongly affected by M. For high-A, the early growth is independent of the Mach number and enhancement occurs later, after the incompressible case reaches the asymptotic velocity and the reacceleration regime.

A conservation of mass principle explains the high-A observation. In this limit, the Mach number has little effect on both the shape of the falling spike and the density profile of the light fluid that the spike is falling into. Since the spike growth converges for all M in the this regime, the mass of the heavy fluid within the the spike is nearly equivalent across all M. The heavy fluid stratification is drastically affected by the increase in M. When the compressibility effects are high, the heavy fluid density profile falls off rapidly away from the interface, and a greater volume of heavy fluid is required to support the spike growth. Thus, the bubble of light fluid rises at an accelerated rate in order to displace the greater volume of heavy fluid.

In order to observe the stratification effects on the growth of the instability as M is varied, Figure 4.10 compares the $M = 0.3$ and $M = 1.0$ cases for $A = 0.1$. At low A, the stratification is about the same on both sides of the interface, since there is very little density difference. For low-M

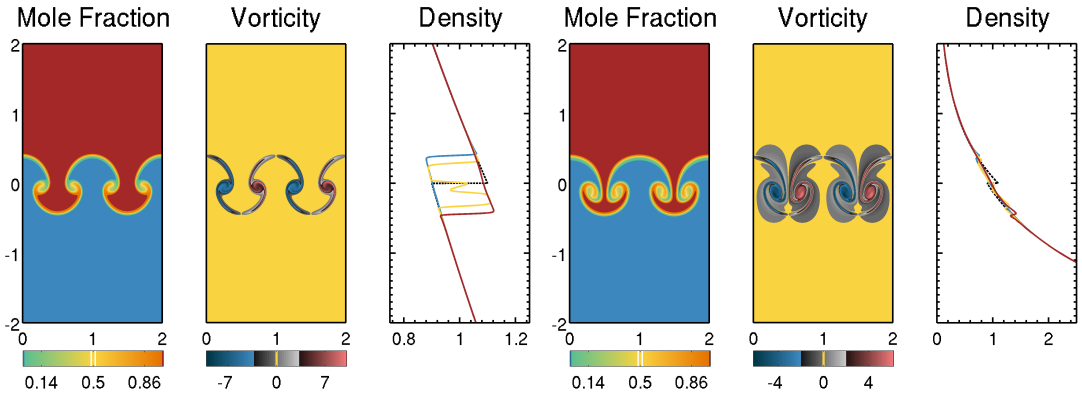

(a) $h_s = 0.5$ for $M = 0.3$ (b) $h_s = 0.5$ for $M = 1.0$

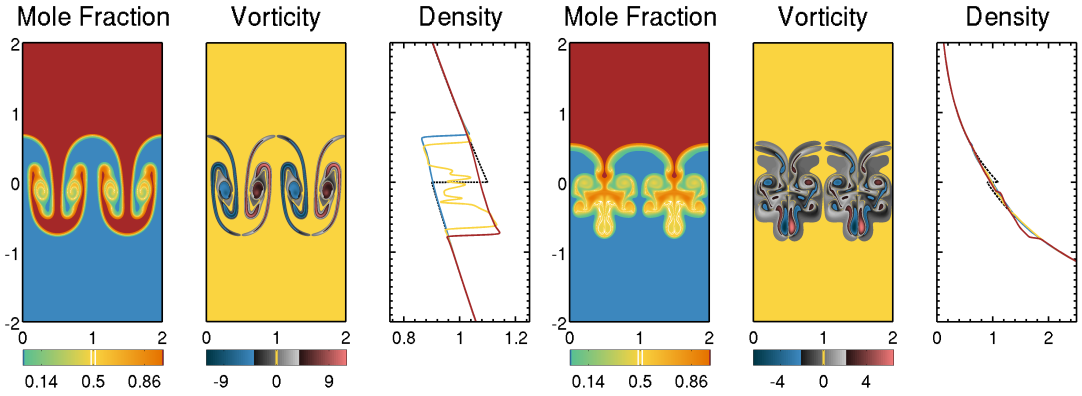

(c) $h_s = 0.8$ for $M = 0.3$ (d) $h_s = 0.8$ for $M = 1.0$

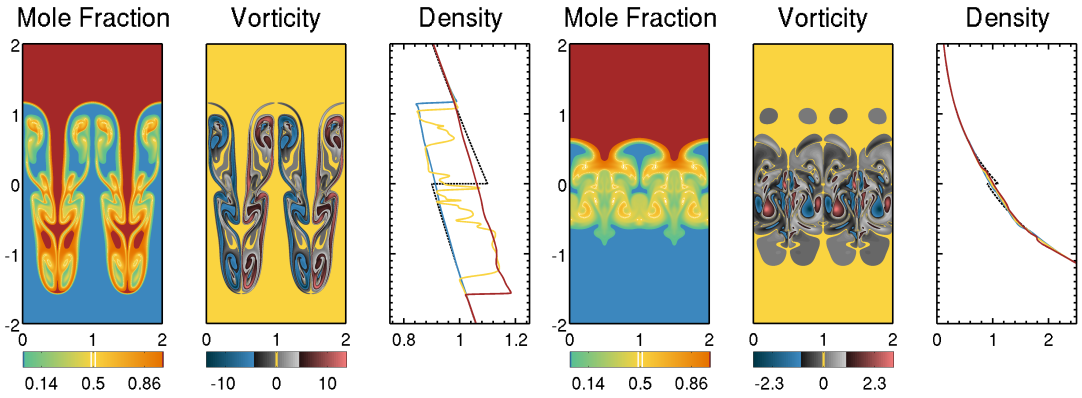

(e) Late-time for $M = 0.3$ (f) Late-time for $M = 1.0$

Figure 4.10: Mole fraction and density profiles for $A = 0.1$, at $M = 0.3$ (low compressibility) and $M = 1.0$ (high compressibility) for comparison.

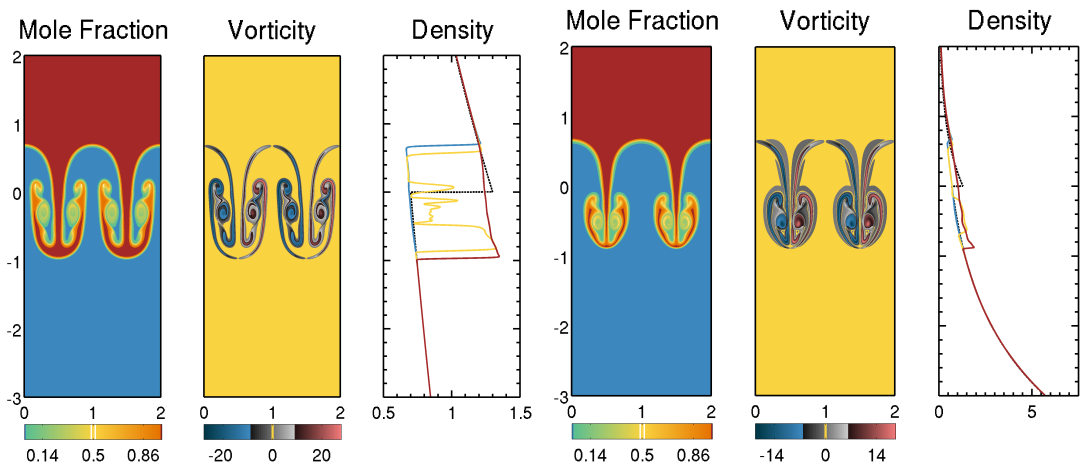

(a) $h_s = 1.0$ for $M = 0.3$

(b) $h_s = 1.0$ for $M = 1.0$

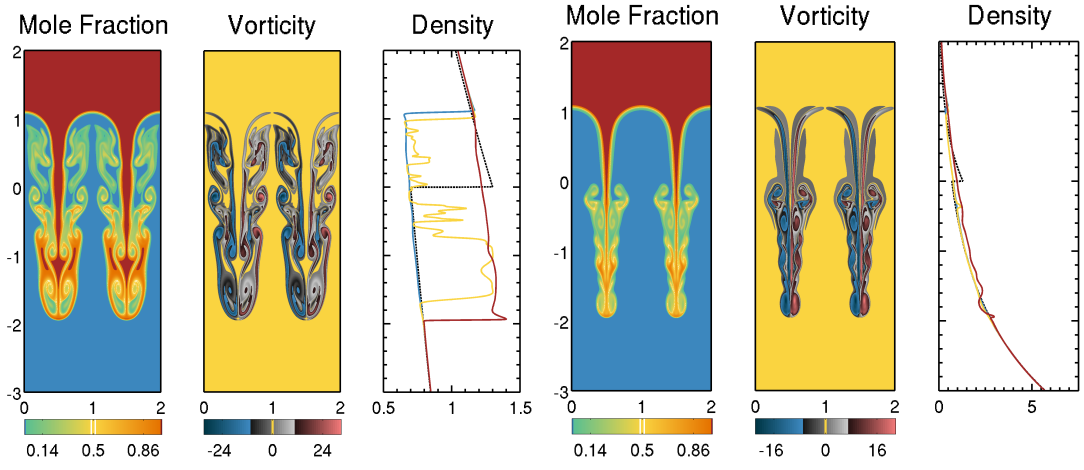

(c) $h_s = 2.0$ for $M = 0.3$

(d) $h_s = 2.0$ for $M = 1.0$

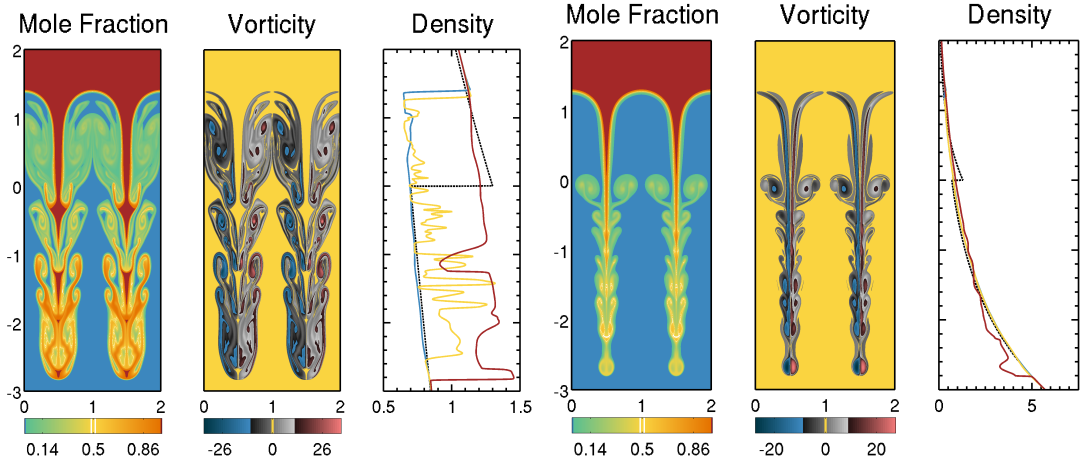

(e) Late-time for $M = 0.3$

(f) Late-time for $M = 1.0$

Figure 4.11: Mole fraction and density profiles for $A = 0.3$, at $M = 0.3$ (low compressibility) and $M = 1.0$ (high compressibility) for comparison.

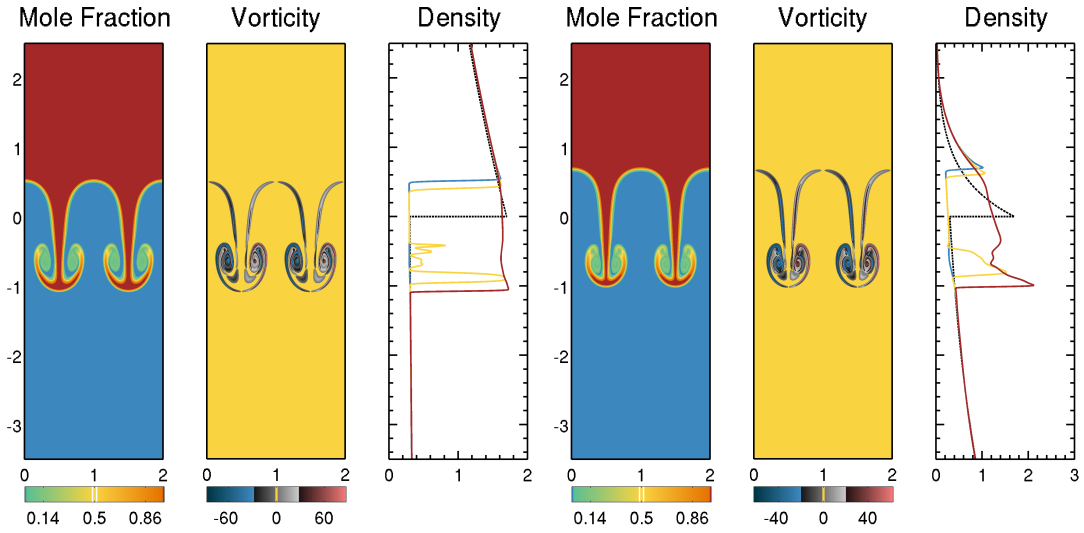

(a) $h_s = 1.0$ for $M = 0.3$

(b) $h_s = 1.0$ for $M = 1.0$

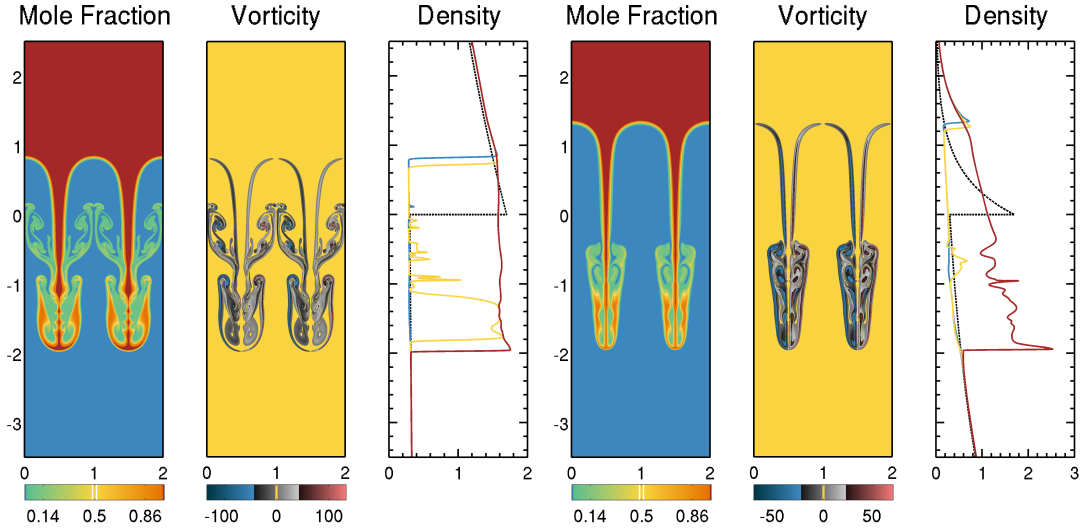

(c) $h_s = 2.0$ for $M = 0.3$

(d) $h_s = 2.0$ for $M = 1.0$

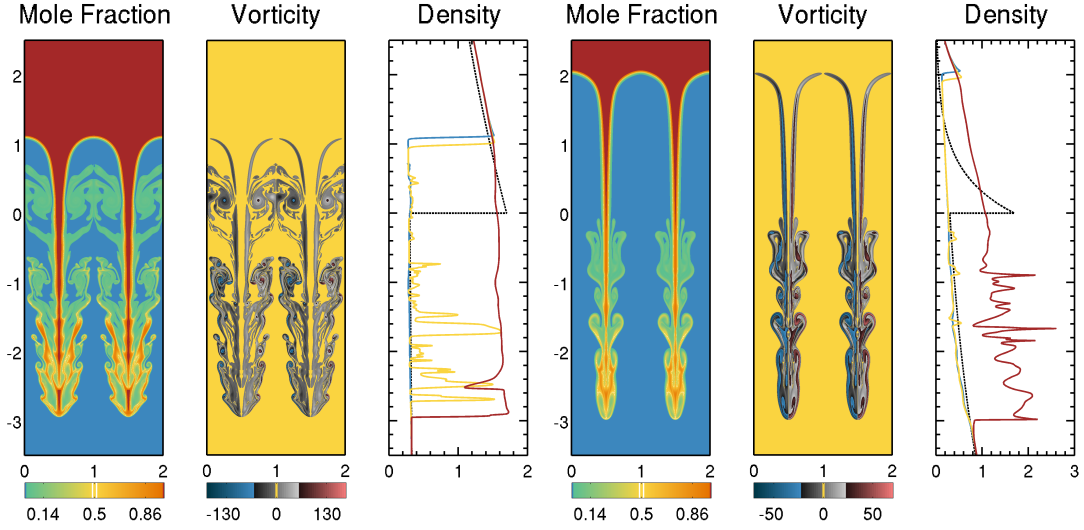

(e) $h_s = 3.0$ for $M = 0.3$

(f) $h_s = 3.0$ for $M = 1.0$

Figure 4.12: Mole fraction and density profiles for $A = 0.7$, at $M = 0.3$ (low compressibility) and $M = 1.0$ (high compressibility) for comparison.

and low-A, the heavy fluid is compressed as it falls, while the density in the light fluid decreases as it rises. This maintains an unstable situation as the instability grows. For high-M and low-A, the initial density difference at the interface is small when compared to the background stratification. The spike only falls a short distance before equilibrium is achieved with global stability.

Figure 4.11 shows results for the moderate $A = 0.3$ case. Once again, the background stratification is vastly different between the $M = 0.3$ and $M = 1.0$ cases. Also, the shapes of the bubbles and spikes are considerably unique. Despite these differences, the growth of the instability is largely the same for both the bubbles and the spikes until a relatively late time, when spike height reaches 2.5λ. At that point, the high-M case is once again suppressed. There is a long period where the density inside the spike is actually lower than the surrounding media. This is attributed to both inertial and compressibility effects. The behavior at $A = 0.3$ is similar to, but delayed with respect to, the $A = 0.1$ case.

The large density difference case is presented in Figure 4.12, where $A = 0.7$. There are differences in the background stratification, but most of the variance occurs in the top fluid. Since, the lower fluid's molar mass is much smaller than that of the top fluid, the densities are much smaller, which leads to relatively low stratification. Thus, the lower fluid is largely unaffected by the compressibility effects, which explains the moderate convergence of spike velocities in the high-A regime. Although the spike velocities for all M approach the $M = 0.1$ curve, the incompressible case remains the upper bound for the growth of the spike. Conversely, the growth of the bubble increases with M, as observed in Figure 4.12. The increased bubble velocity is directly linked to the spike evolution and the need for more heavy fluid material to maintain the rate of the falling spike.

Vorticity is suppressed in the higher M systems for all cases presented. Also, the wake of the vortices is kept closer to the spike when the stratification is high. That is, the horizontal cross-sectional area of the spike and its trailing vortices is much smaller for the high-M cases. Not only is vortex production suppressed, but the vortex spreading and interaction remains confined. The spike is more streamlined when stratification is high. This is investigated in more detail in next

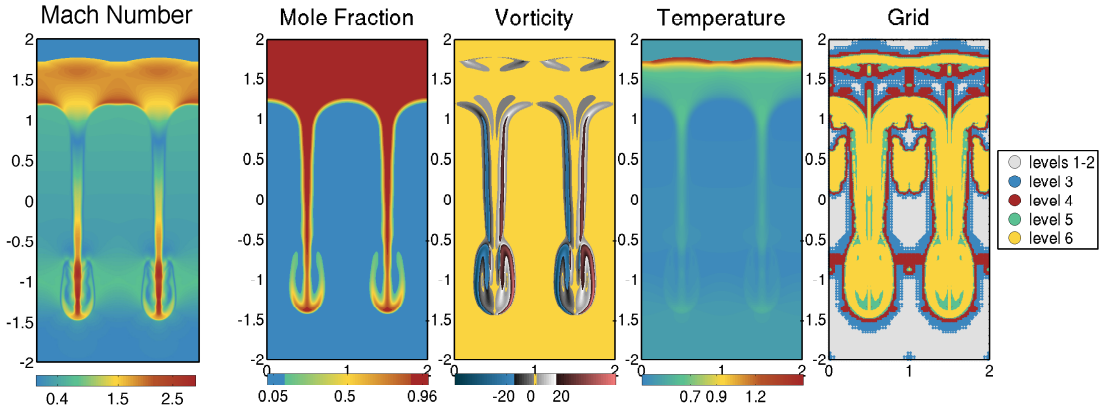

(a) M_{local} (b) X, ω, T, and the adaptive grid

Figure 4.13: Rayleigh-Taylor shock wave with a highly stratified background state ($M = 1.5$ and $A = 0.9$).

section.

Figure 4.13 shows the grid for highly stratified RTI. In this case, the bubbles act like pistons continually generating shock waves [60]. The Rayleigh-Taylor shock wave can be seen as a temperature jump above the bubbles. The local Mach number is defined as $M_{local} = |\mathbf{u}|/c$, where the local speed of sound is $c = \sqrt{\gamma p/\rho}$. The rapid acceleration of the bubble causes the flow behind the shock to become highly supersonic. The grid dynamically adapts to the formation and propagation of the shock wave. For this case, the effective global resolution is 8193×512, yet only 9% of the points are used (375,634 points, 91% compression).

4.4 Vortex Dynamics in Rayleigh-Taylor Instability

The late-time growth of single-mode RTI is dominated by vortex creation, interactions, and the induced velocities. The chaotic nature of the bubble and spike evolution at late-times is due to the sporadic jets produced from vortex pair interactions and the stretching and squeezing of the spike stem. This can lead to puffing of the spike, characterized by quick burts of acceleration as material is propelled downward. When vortex pairs reach the bubble or spike tip region, the induced velocity drives the growth of the bubble or spike.

The vortex dynamics can be analyzed by studying the vorticity equation. However, in order

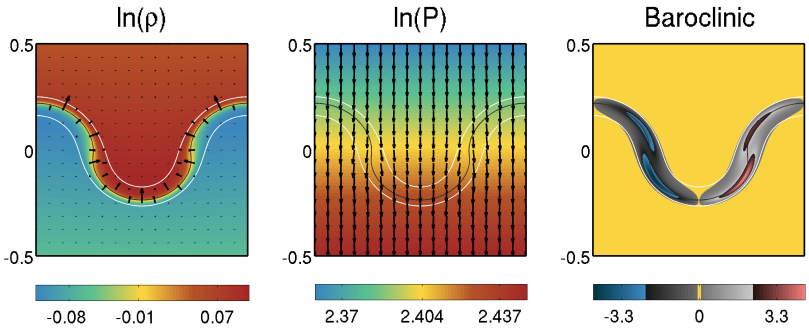

(a) Baroclinic Decomposition $M = 0.3$ and $A = 0.1$

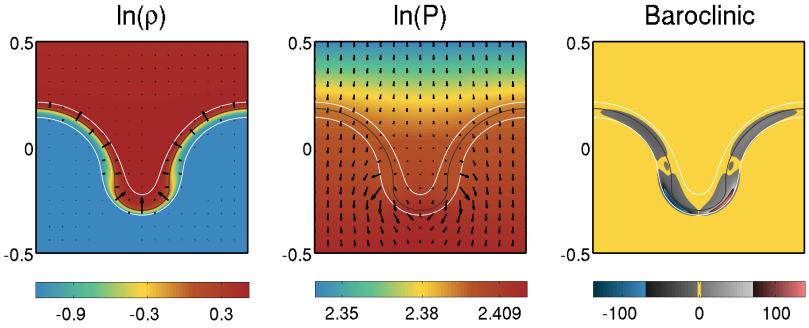

(b) Baroclinic Decomposition $M = 0.3$ and $A = 0.7$

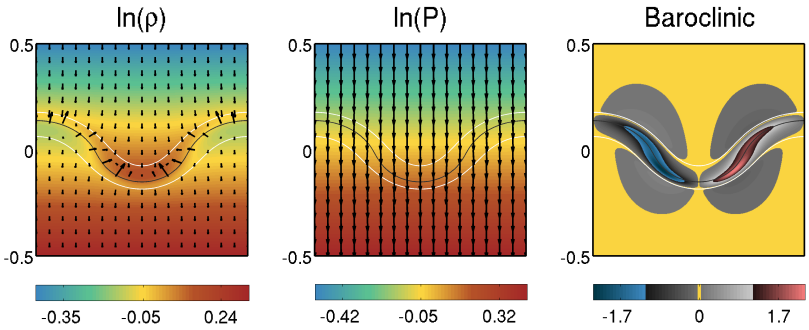

(c) Baroclinic Decomposition $M = 1.0$ and $A = 0.1$

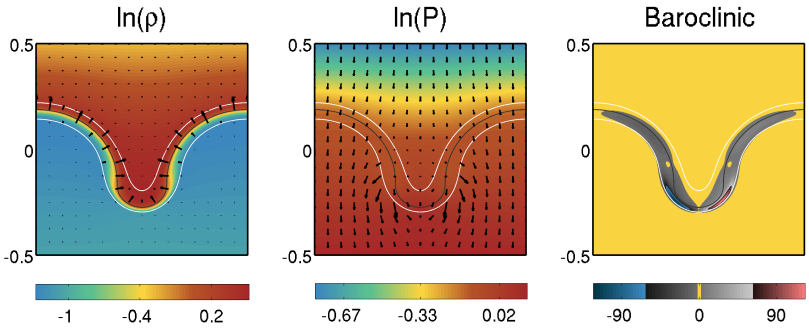

(d) Baroclinic Decomposition $M = 1.0$ and $A = 0.7$

Figure 4.14: In order to compare the Atwood and Mach effects on the baroclinic generation of enstrophy, the gradients of $\ln(\rho)$ and $\ln(p)$ are vector plotted above the fields themselves. The vector plot for pressure is also multiplied by c^2. Baroclinic generation of vorticity is simply the cross product, labeled as "Baroclinic."

take advantage of the symmetry of the system, horizontal averages will be taken. This motivates use of enstrophy, defined as

$$\Omega = \frac{1}{2}\vec{\omega} \cdot \vec{\omega}, \tag{4.2}$$

which is simply a measure of the vorticity magnitude. When a horizontal plane has a large average enstrophy, it is a sign that the vorticity is large and the surrounding media will be influenced by the induced velocities. The enstrophy transport equation is

$$\frac{\partial \Omega}{\partial t} = -(\vec{u} \cdot \nabla)\Omega + \vec{\omega} \cdot [(\vec{\omega} \cdot \nabla)\vec{u}] - 2\Omega(\nabla \cdot \vec{u}) + \frac{\vec{\omega}}{\rho^2} \cdot [\nabla\rho \times \nabla p] + \vec{\omega} \cdot \left[\nabla \times \left(\frac{\nabla \cdot \tau}{\rho}\right)\right], \tag{4.3}$$

where the terms on the right hand side of the equation are, in order, the convection, stretching, compressive, baroclinic, and viscous terms. For the two dimensional case, the stretching term has no contribution.

RTI is driven by the baroclinic generation of vorticity, since misaligned pressure and density gradients are responsible for the early instability growth. The baroclinic term can be rewritten as

$$\frac{\vec{\omega}}{\rho} \cdot [\nabla\rho \times \nabla p] = \frac{c^2\vec{\omega}}{\gamma} \cdot [\nabla \ln(\rho) \times \nabla \ln(p)]. \tag{4.4}$$

Figure 4.14 shows a decomposition of the baroclinic term by vector plotting the gradients. Strong enstrophy production occurs in locations where the two fields are perpendicular. For the low-A, low-M case, the density gradients are always normal to the interface, and pressure gradients are strictly vertical. Thus, the baroclinic generation is strongest where the interface is vertically aligned, which occurs near the mid-plane. As the Atwood number is raised to $A = 0.7$, the density gradients remain normal to the interface, but pressure takes on strong local variations due to the motion of the spike. The strongest baroclinic generation occurs near the spike tips. There is little baroclinic generation near the bubble tips.

In addition to occurring closer to the spike tips, the baroclinic generation is also stronger for higher A, because the density gradients are larger. This effect can be seen in the horizontal averaged plots shown in Figure 4.15, where the peak of the baroclinic generation of enstrophy lies near the mid-plane between the bubble and spike for the $A = 0.1$ cases and near the bubble tip for

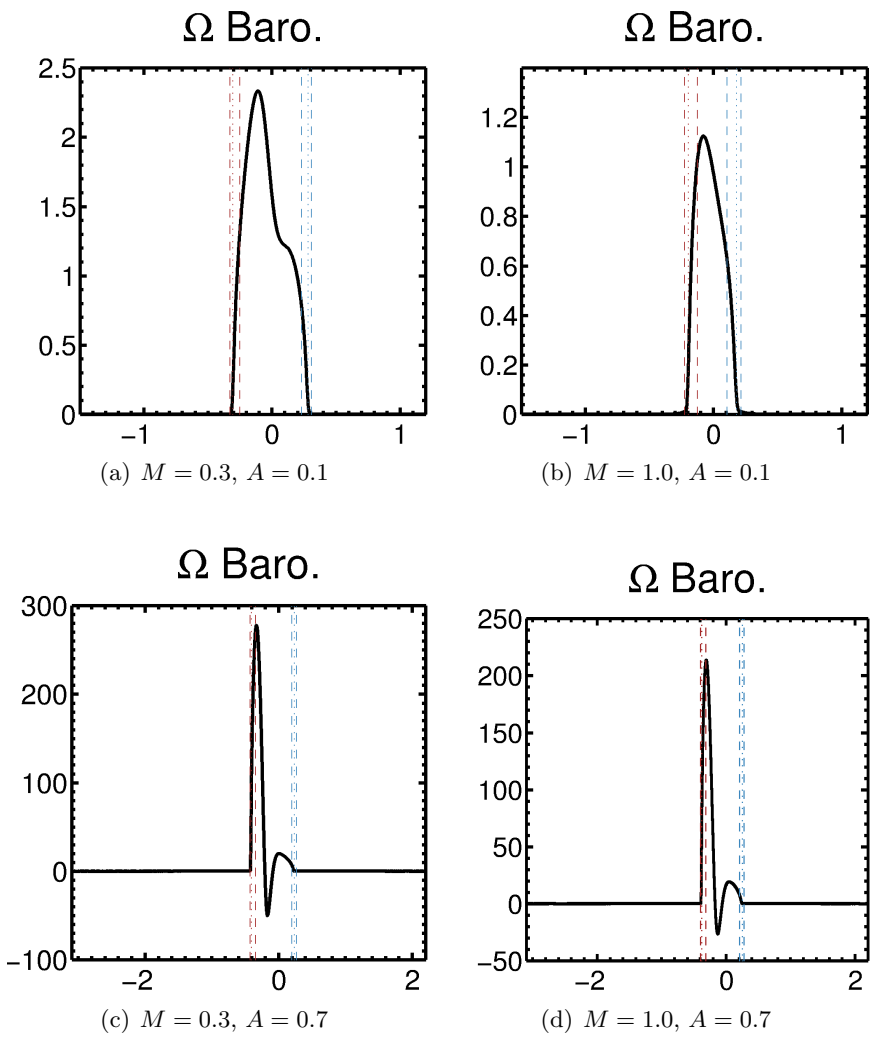

(a) $M = 0.3$, $A = 0.1$ (b) $M = 1.0$, $A = 0.1$

(c) $M = 0.3$, $A = 0.7$ (d) $M = 1.0$, $A = 0.7$

Figure 4.15: Horizontal averaged baroclinic enstrophy for early times. The red dashed lines represent the outer limits of the spike tip along $x_1 = 0.5$. The blue dashed lines represent the outer limits of the bubble tip along $x_1 = 0$.

the $A = 0.7$ cases. Also, the baroclinic enstrophy generation is two orders of magnitude greater for the high-A cases.

The compressibility effects cause a weakening of the early enstrophy generation from the baroclinic terms. For the incompressible case, the only density gradients lie normal to the interface between the two species. The compressibility effects lead to stably stratified background states within each pure fluid. This cancels some of the interfacial density gradient effects as observed in the baroclinic decomposition in Figure 4.14. Compressibility has little effect on the Atwood

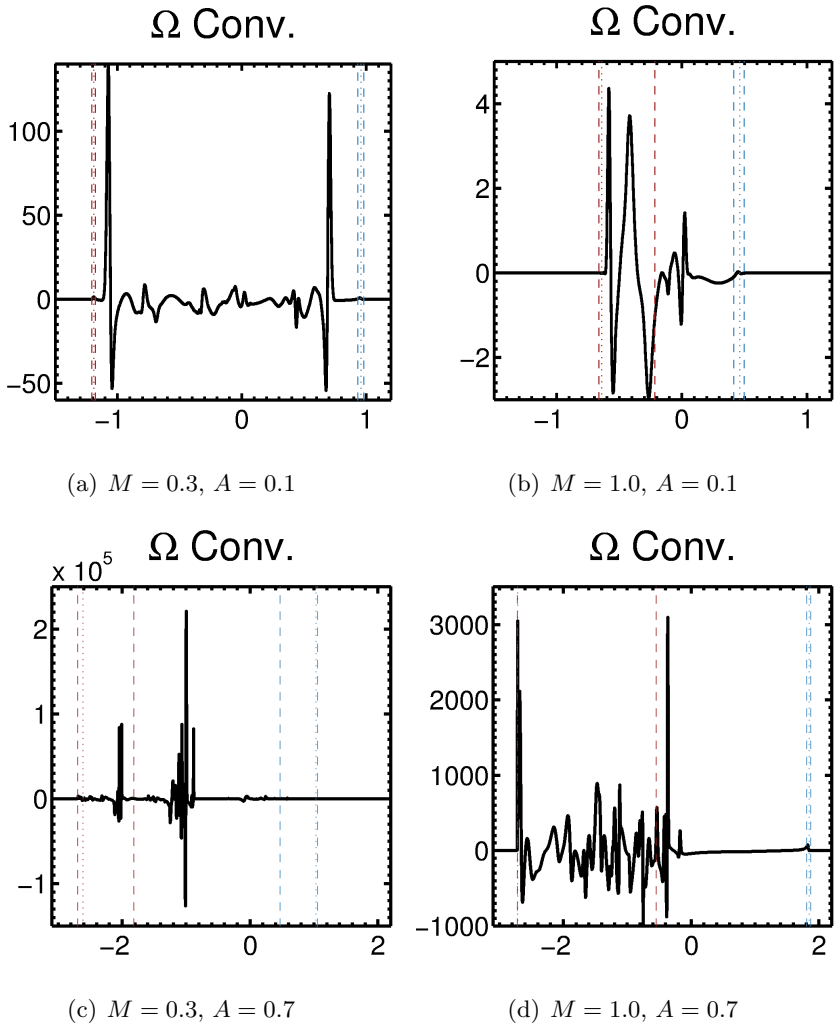

(a) $M = 0.3$, $A = 0.1$

(b) $M = 1.0$, $A = 0.1$

(c) $M = 0.3$, $A = 0.7$

(d) $M = 1.0$, $A = 0.7$

Figure 4.16: Horizontally averaged enstrophy convection terms show the transport of enstrophy toward the bubbles and spikes. The red dashed lines represent the outer limits of the spike tip along $x_1 = 0.5$. The blue dashed lines represent the outer limits of the bubble tip along $x_1 = 0$.

dependence on the baroclinic generation. The observations made in the incompressible limit, as A is increased, hold true for the high-M cases. That is, the baroclinic generation in the high-A cases is stronger in magnitude and skewed away from the bubble and toward the spike.

The early time growth is dominated by baroclinic generation, and is the cause for the vortex roll-up of the interface. The induced velocities from the initial vortex pair cause a reaccleration of the instability. The vorticies themselves then begin to move with the flow. At later-times, the enstrophy is transported toward the bubble and spike tips, which can be seen in the horizontally

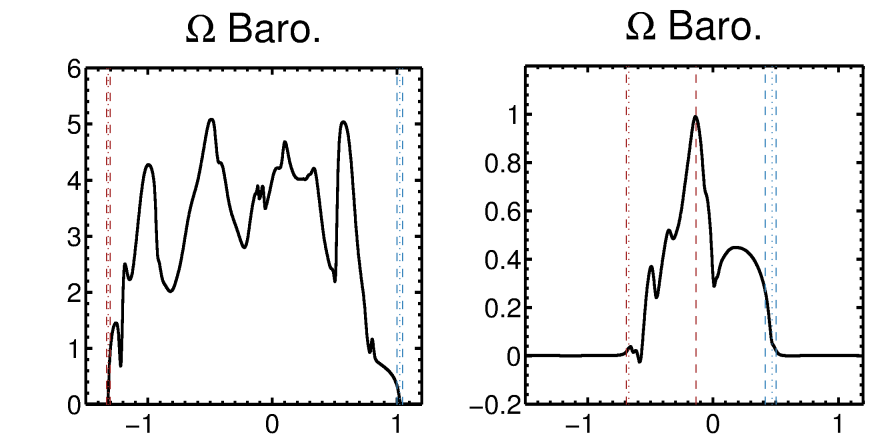

(a) $M = 0.3$, $A = 0.1$ (b) $M = 1.0$, $A = 0.1$

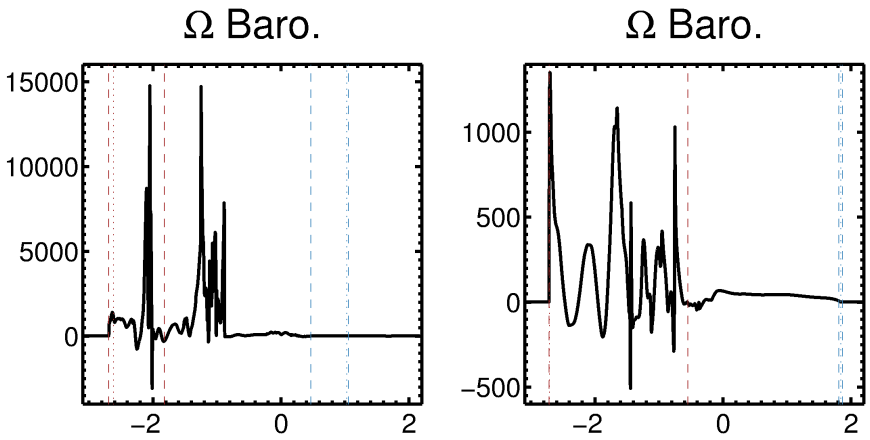

(c) $M = 0.3$, $A = 0.7$ (d) $M = 1.0$, $A = 0.7$

Figure 4.17: Late-time horizontally averaged baroclinic enstrophy. The red dashed lines represent the outer limits of the spike tip along $x_1 = 0.5$. The blue dashed lines represent the outer limits of the bubble tip along $x_1 = 0$.

averaged quantities in Figure 4.16. The enstrophy transport is symmetric for the low-A case. For large Atwood number, the enstrophy transport toward the bubble is suppressed. The vortical motion do not need to travel far to reach the spike, however, and therefore have an almost immediate impact on the growth of the spike. At late-times, enstrophy transport and compression may play a large role, but there remains baroclinic generation at the spike tips, as seen in the high-M, high-A results from Figure 4.17. The newly generated enstrophy near the spike tips results in newly formed vortices, which lead to vortex interactions. In this sense, the spike tips act as a vorticity generator

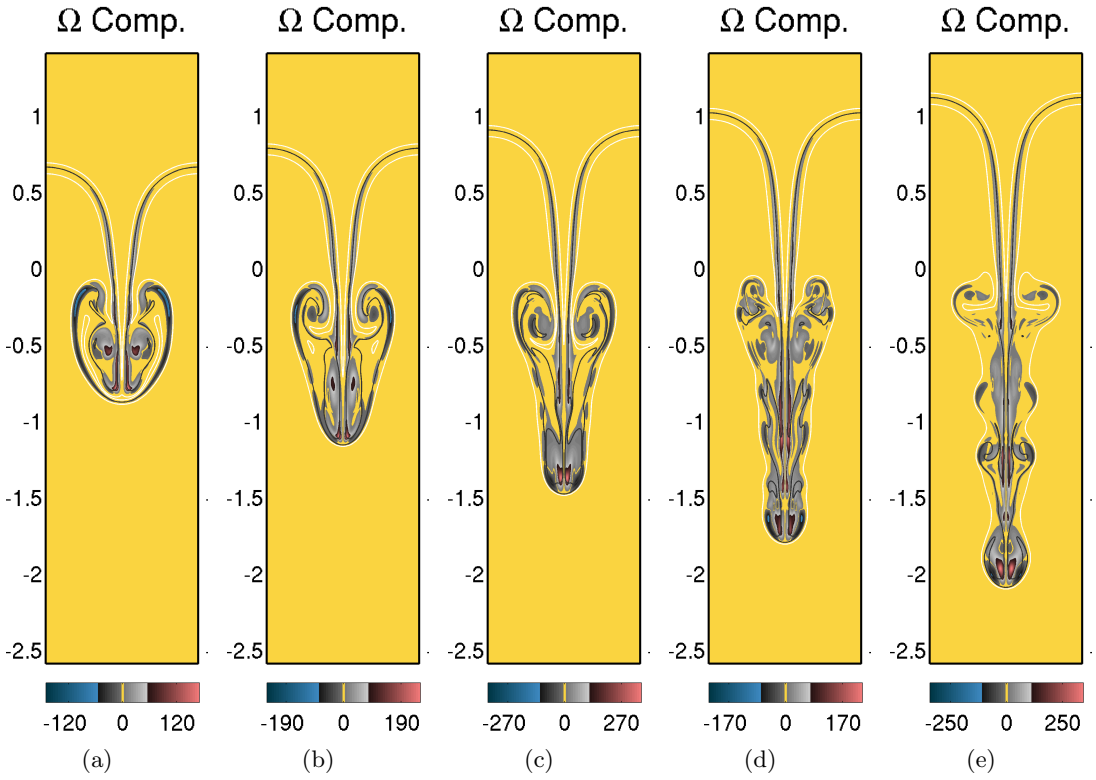

Figure 4.18: Enstrophy compression at spike tip for $M = 0.1$ and $A = 0.3$.

that inevitably gets transported toward the bubble, but never reaches the bubble for high Atwood numbers. The vortices are interrupted by other vortical motions as they travel upwards. The vortical flow initially generated near the spike tips, is more likely to return to the spike, causing sporadic accelerations.

In some cases, after the enstrophy generation at the spike tips and transport toward the bubble, a vortical structure is pulled back down by the induced motion from other vorticies. It travels toward the spike tip along the stem. Upon reaching the spike tip, a strong compression occurs, which acts to further enhance the local enstrophy and intensifies the induced flow. Figure 4.18 is an example of the compression term having a large impact on the growth of the spike. This case corresponds to the high-M case shown in Figure 4.11. At very late times, the density within the spike tip is actually significantly less than the surrounding media. The enstrophy compression and the resulting intense induced flow within the spike tip overcomes the buoyant forces that try

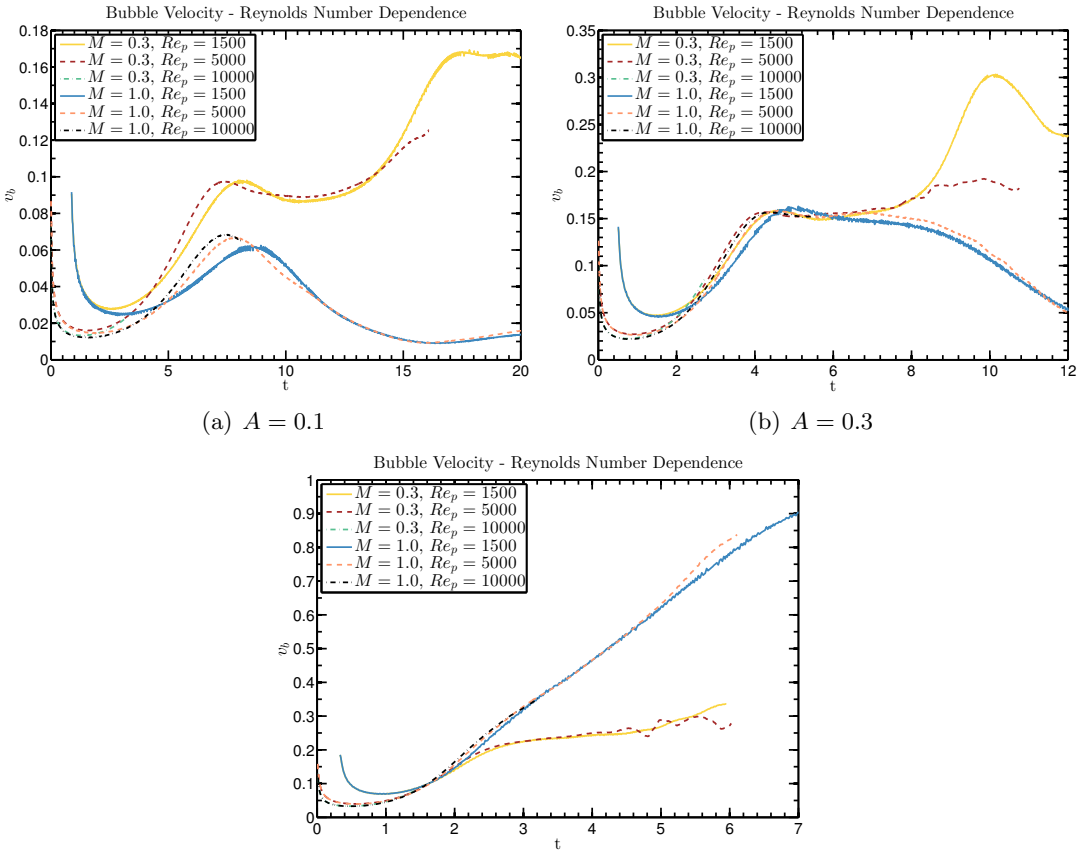

(a) $A = 0.1$

(b) $A = 0.3$

(c) $A = 0.7$

Figure 4.19: Bubble velocity plotted for various perturbation Reynolds numbers.

to pull the spike back up. The viscous terms are small, and act as drag on the enstrophy transport.

4.5 Viscous Effects on Rayleigh-Taylor Instability

The growth of RTI may have a large Reynolds number dependence. The vortical motions generated from the baroclinic terms have a dominant role in the chaotic nature of the late-time RTI growth. Viscosity may strongly influence the late-time behavior since it tends to damp vortical motions.

The bubble velocity evolution as A, M, and Re_p are all varied are shown in Figure 4.19, in order to test the Reynolds dependence on the reversal of the monotonic relationship for M and A. The $Re_p = 1500$ case is time-shifted since a large initial amplitude is applied for that case. Viscosity

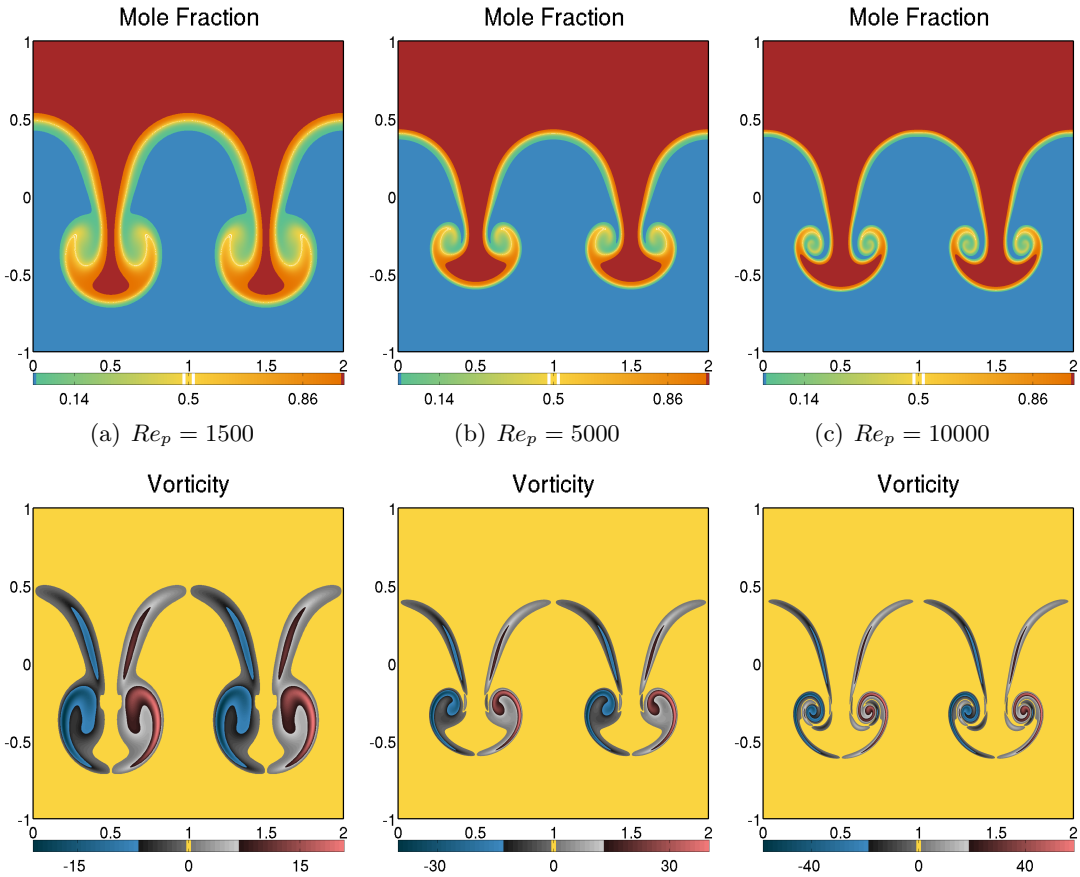

(a) $Re_p = 1500$ (b) $Re_p = 5000$ (c) $Re_p = 10000$

(d) $Re_p = 1500$ (e) $Re_p = 5000$ (f) $Re_p = 10000$

Figure 4.20: Early time Reynolds number comparison.

acts to decrease the exponential growth rate predicted from linear stability theory. This effect can be seen in the figure. The qualitative behavior remains the same across all Reynolds numbers well into the reacceleration region. The largest deviation occurs at late-times for $A = 0.3$, where the low-Re_p bubble undergoes a strong reacceleration and the moderate-Re_p bubble experiences a small acceleration. In this case, the higher viscosity case has an enhanced growth. This supports the theory discussed in Section 4.4 that vorticity suppression enhances the growth of the bubbles and spikes.

The viscosity effect on the molar mass fraction and vorticity is shown in Figure 4.20. Viscosity not only causes a larger diffusion layer at the interface but also leads to decreased vorticity during the early stages of RTI growth. Figure 4.21 compares the $Re_p = 1500$ and $Re_p = 5000$ cases

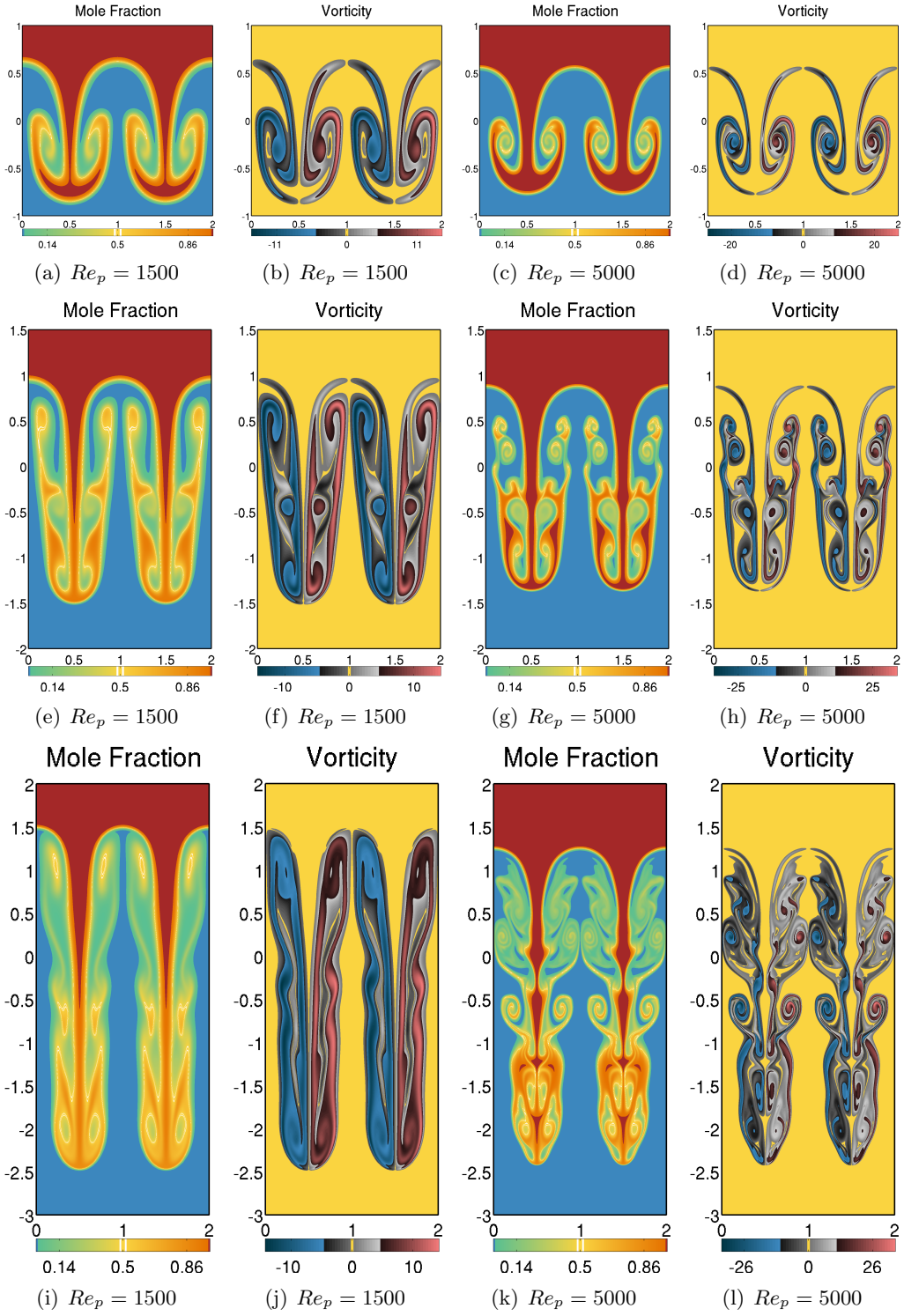

(a) $Re_p = 1500$ (b) $Re_p = 1500$ (c) $Re_p = 5000$ (d) $Re_p = 5000$

(e) $Re_p = 1500$ (f) $Re_p = 1500$ (g) $Re_p = 5000$ (h) $Re_p = 5000$

(i) $Re_p = 1500$ (j) $Re_p = 1500$ (k) $Re_p = 5000$ (l) $Re_p = 5000$

Figure 4.21: Late time Reynolds number comparison.

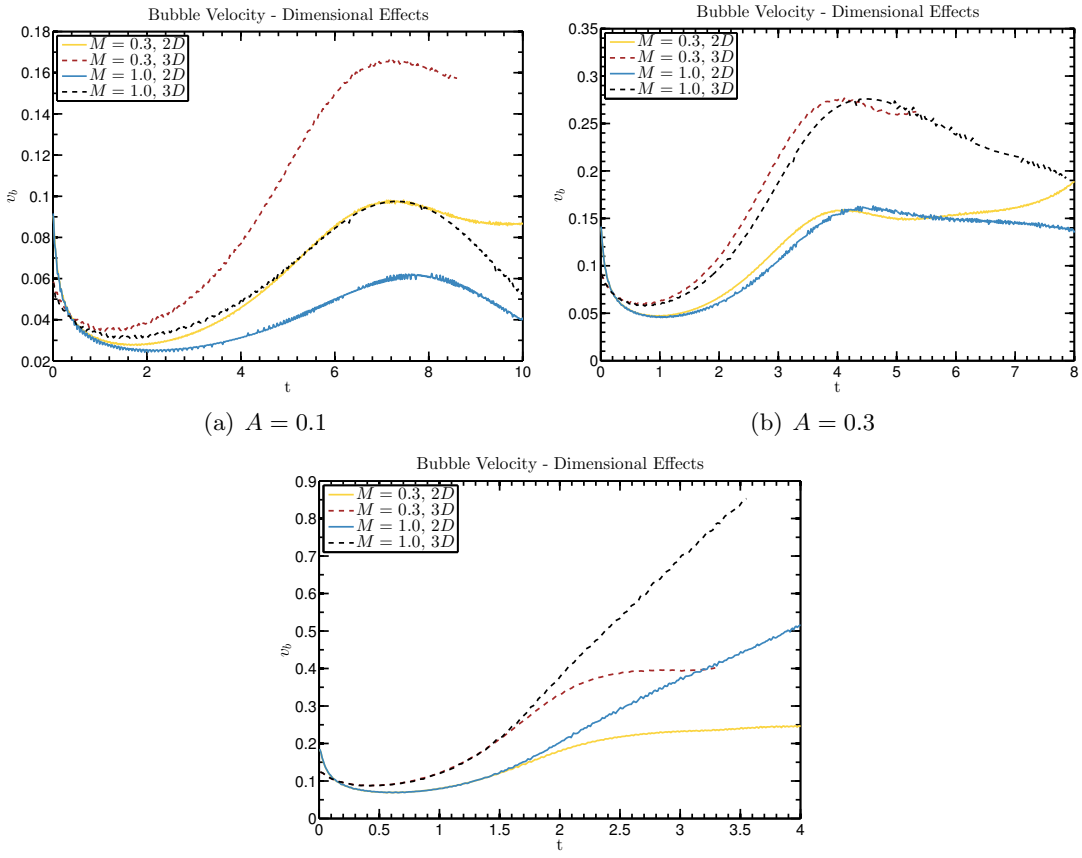

(a) $A = 0.1$

(b) $A = 0.3$

(c) $A = 0.7$

Figure 4.22: Dimensional effects on bubble velocity evolution.

into the late time RTI growth. There are large visual differences, yet the bubble growth is largely unaffected.

4.6 Dimensionality Effects on Rayleigh-Taylor Instability

Three dimensional single-mode RTI cases are presented as a qualitative comparison of the dynamics observed in the two dimensional cases. The dimensional effects on single-mode RTI are investigated for $Re_p = 1500$. A comparison of the bubble velocity evolution is shown in Figure 4.22. The three dimensional cases have the same change in monotonic behavior observed for the two dimensional cases. That is, the compressibility effects suppress RTI growth at low-A and enhance the late-time bubble growth at high-A, for both 2D and 3D. The transition occurs around

(a) Bubble, $M = 0.3$, $A = 0.1$
(b) Spike, $M = 0.3$, $A = 0.1$
(c) Bubble, $M = 1.0$, $A = 0.1$
(d) Spike, $M = 1.0$, $A = 0.1$
(e) Bubble, $M = 0.3$, $A = 0.3$
(f) Spike, $M = 0.3$, $A = 0.3$
(g) Bubble, $M = 1.0$, $A = 0.3$
(h) Spike, $M = 1.0$, $A = 0.3$
(i) Bubble, $M = 0.3$, $A = 0.7$
(j) Spike, $M = 0.3$, $A = 0.7$
(k) Bubble, $M = 1.0$, $A = 0.7$
(l) Spike, $M = 1.0$, $A = 0.7$

Figure 4.23: The three dimensional RTI cases are presented with isosurfaces of the interface, where the fluids are equally mixed based on the molar mass fraction.

$A = 0.3$. The drag coefficient used to obtain the asymptotic velocity from potential flow theory is lower for the 3D case than for 2D. A deceleration of the 3D bubbles occurs upon reaching the asymptotic velocity for the cases run in the incompressible limit.

Figure 4.23 highlights the shapes of the 3D bubbles and spikes at the point where the bubble

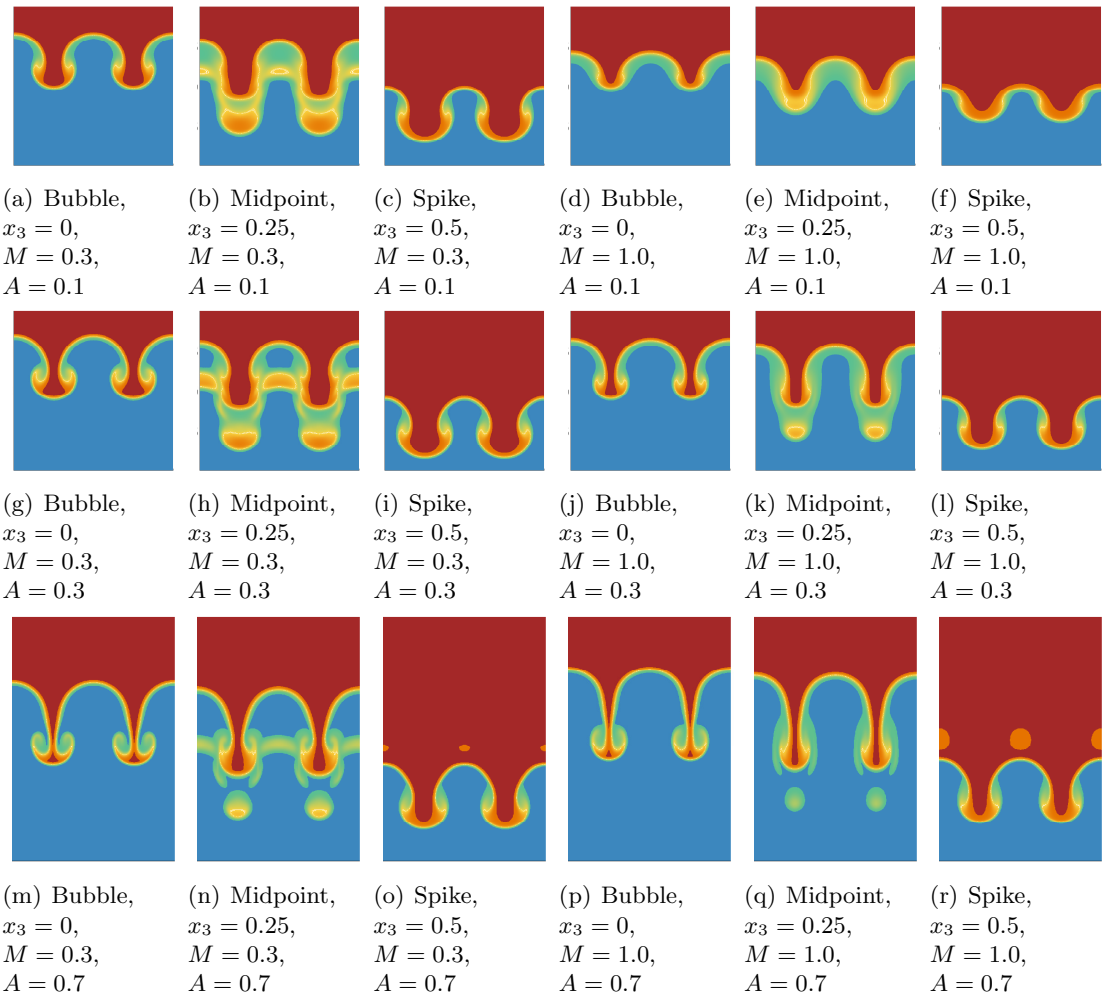

(a) Bubble, $x_3 = 0$, $M = 0.3$, $A = 0.1$ | (b) Midpoint, $x_3 = 0.25$, $M = 0.3$, $A = 0.1$ | (c) Spike, $x_3 = 0.5$, $M = 0.3$, $A = 0.1$ | (d) Bubble, $x_3 = 0$, $M = 1.0$, $A = 0.1$ | (e) Midpoint, $x_3 = 0.25$, $M = 1.0$, $A = 0.1$ | (f) Spike, $x_3 = 0.5$, $M = 1.0$, $A = 0.1$

(g) Bubble, $x_3 = 0$, $M = 0.3$, $A = 0.3$ | (h) Midpoint, $x_3 = 0.25$, $M = 0.3$, $A = 0.3$ | (i) Spike, $x_3 = 0.5$, $M = 0.3$, $A = 0.3$ | (j) Bubble, $x_3 = 0$, $M = 1.0$, $A = 0.3$ | (k) Midpoint, $x_3 = 0.25$, $M = 1.0$, $A = 0.3$ | (l) Spike, $x_3 = 0.5$, $M = 1.0$, $A = 0.3$

(m) Bubble, $x_3 = 0$, $M = 0.3$, $A = 0.7$ | (n) Midpoint, $x_3 = 0.25$, $M = 0.3$, $A = 0.7$ | (o) Spike, $x_3 = 0.5$, $M = 0.3$, $A = 0.7$ | (p) Bubble, $x_3 = 0$, $M = 1.0$, $A = 0.7$ | (q) Midpoint, $x_3 = 0.25$, $M = 1.0$, $A = 0.7$ | (r) Spike, $x_3 = 0.5$, $M = 1.0$, $A = 0.7$

Figure 4.24: Vertical slices of three dimensional cases

begins to decelerate. Isosurfaces are shown, representing the interface where the heavy and light fluids are equally mixed based on the molar mass fraction, that is, $X = 1/2$. To further enhance the bubble and spike shape comparison, vertical slices of the molar mass fraction at the same time instances are shown in Figure 4.24. Each case is represented by three images, with A increasing downwards and M increasing to the right. The small density differences for $A = 0.1$ lead to an instability growth that is nearly symmetric about the mid-plane. The shapes of the bubbles and spikes are nearly identical. This is also apparent when looking at horizontal slices, presented in Figure 4.25. The low-A case is shown in the first row. As the density difference is increased, the spikes become more narrow surrounded by smoother and rounder bubbles. As M is increased, the

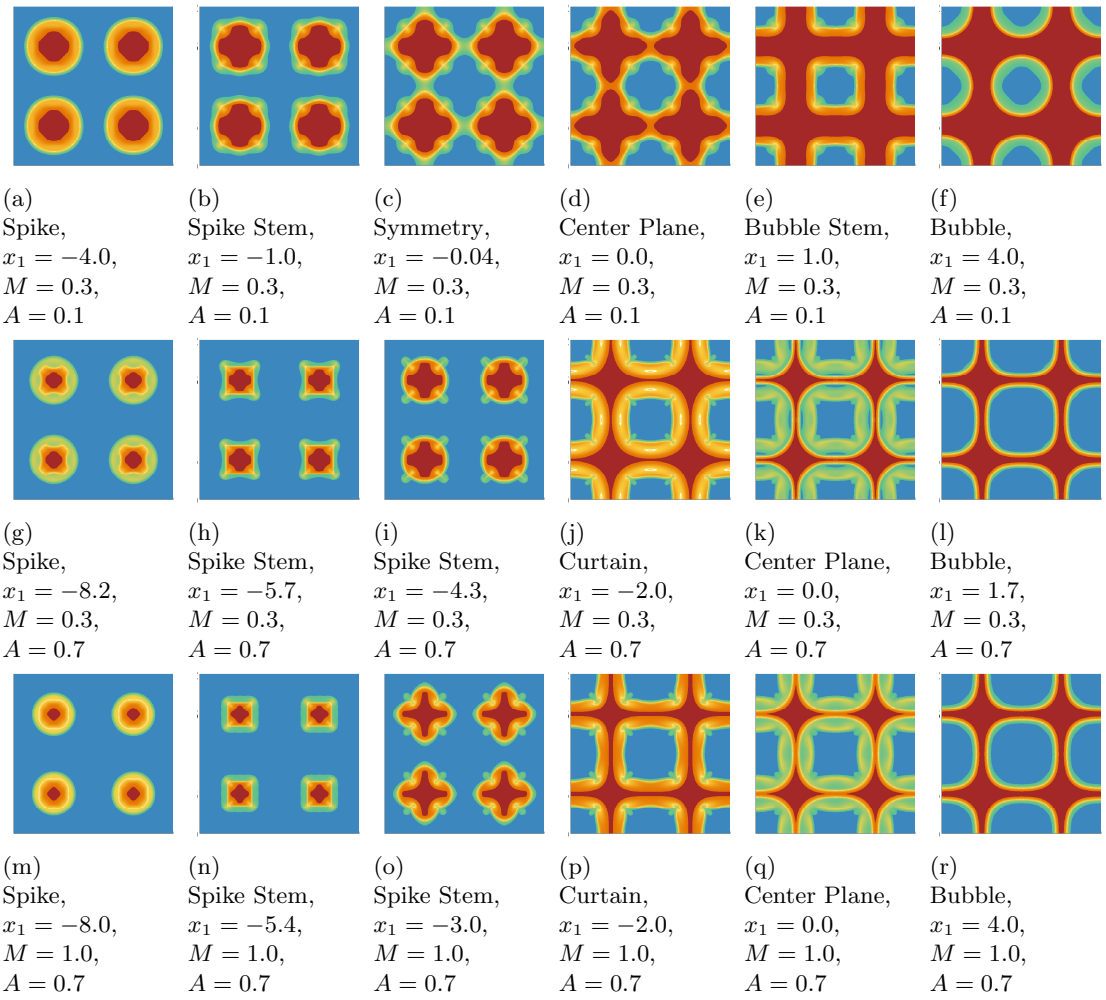

(a) Spike, $x_1 = -4.0$, $M = 0.3$, $A = 0.1$
(b) Spike Stem, $x_1 = -1.0$, $M = 0.3$, $A = 0.1$
(c) Symmetry, $x_1 = -0.04$, $M = 0.3$, $A = 0.1$
(d) Center Plane, $x_1 = 0.0$, $M = 0.3$, $A = 0.1$
(e) Bubble Stem, $x_1 = 1.0$, $M = 0.3$, $A = 0.1$
(f) Bubble, $x_1 = 4.0$, $M = 0.3$, $A = 0.1$

(g) Spike, $x_1 = -8.2$, $M = 0.3$, $A = 0.7$
(h) Spike Stem, $x_1 = -5.7$, $M = 0.3$, $A = 0.7$
(i) Spike Stem, $x_1 = -4.3$, $M = 0.3$, $A = 0.7$
(j) Curtain, $x_1 = -2.0$, $M = 0.3$, $A = 0.7$
(k) Center Plane, $x_1 = 0.0$, $M = 0.3$, $A = 0.7$
(l) Bubble, $x_1 = 1.7$, $M = 0.3$, $A = 0.7$

(m) Spike, $x_1 = -8.0$, $M = 1.0$, $A = 0.7$
(n) Spike Stem, $x_1 = -5.4$, $M = 1.0$, $A = 0.7$
(o) Spike Stem, $x_1 = -3.0$, $M = 1.0$, $A = 0.7$
(p) Curtain, $x_1 = -2.0$, $M = 1.0$, $A = 0.7$
(q) Center Plane, $x_1 = 0.0$, $M = 1.0$, $A = 0.7$
(r) Bubble, $x_1 = 4.0$, $M = 1.0$, $A = 0.7$

Figure 4.25: Horizontal slices of the three dimensional cases.

vortical structures generated near the spike tip remain more localized to the stem of the spike. Thus, the compressibility effects cause the spike to become more streamlined. These structural observations of the 3D RTI growth match the 2D cases. However, there are some characteristics of RTI growth that can only exist in the full three dimensional system. For example, when the Atwood number is high, the descending spikes are accompanied by thin curtains of heavy fluid that surround the wide bubbles, as seen in the middle row of the horizontal slices matrix. The curtain effect is enhanced by increasing the Mach number (bottom row of the horizontal slices matrix), as the spike shape becomes more streamlined. Another three dimensional effect is the square cross-sectional of the spike stems, which results from a forced symmetry due to the geometry of the

bubbles and spikes.

Chapter 5

Conclusions and Future Work

Simulations of compressible Rayleigh-Taylor systems require the development and implementation of computational tools that efficiently handle acoustic waves, extreme density ranges, and a wide array of physical scales. These difficulties are successfully dealt with by the use of the Parallel Adaptive Wavelet Collocation Method in conjunction with two different, but equally effective, boundary treatments that successfully remove acoustic disturbances from the computational domain. The first method applies a buffer zone near the vertical edges, where strong numerical diffusion is applied. The use of a dynamically adaptive grid allows the diffusion zone to be extended to extreme lengths, which ensures maximum damping of the acoustic waves with negligible added computational cost. The second method utilizes characteristic analysis to apply a non-reflecting boundary condition that removes the energy in the acoustic waves from the system at the domain boundaries. The analysis takes into account the background stratification present in compressible Rayleigh-Taylor systems. The generation of acoustic waves due to inconsistencies in the initialization is limited by minimizing pressure disturbances near the interface, which further optimizes the use of computational resources.

The advanced computational framework developed specifically for direct numerical simulations of compressible Rayleigh-Taylor systems has shed new light on the true nature of the instability. The compressive quality cannot be summarized by any one single quantity, nor are the effects universal. Stratification is closely tied to the intrinsic compressibility within the system, but it is also affected by the molar mass difference between the two fluids. When the difference is small,

compressibility acts to quickly suppress any mixing, and global stability can be achieved quickly. Such a suppression of Rayleigh-Taylor instability is required for the future feasibility of inertial confinement fusion technology. Conversely, for systems like type Ia supernovae, where there is a large difference in molar mass, unstable configurations within a highly compressive system lead to an enhanced growth when compared to the incompressible system.

It is apparent that the late-time behavior of single-mode Rayleigh-Taylor instability is heavily influenced by the vortical nature of the system. Vorticity is initially generated inside the mixing layer due to the misalignment of the density and pressure fields. The vortical structures are then transported outward and may reach the bubble and spike tips, where the induced velocities cause a chaotic growth. When compressibility effects are high, the vorticity generation is weakened and the spike takes on a more streamlined shape, where the vortices remain close to the spike stem. Additionally, the compressive nature of the fluids provide a mechanism to enhance the induced motion near the spike tip. Because the late-time growth is dominated by vortical influences, the strength of viscous and diffusion effects on Rayleigh-Taylor systems becomes important. If the Reynolds number is too small, vorticity may be suppressed before the induced motion has any affect on the flow, which can drastically alter the nature of the instability growth at late-times. In order to investigate real systems where Rayleigh-Taylor instability plays a role, simulations must be carried out at significantly high Reynolds numbers. Furthermore, the late-time Rayleigh-Taylor instability growth must be studied in a three-dimensional domain to allow the tilting of vorticity that is absent from two-dimensional flows. Many of the flow characteristics observed in the two-dimensional system extend to the three-dimensional case, including exponential growth, deceleration near the asymptotic velocity from potential flow theory, reacceleration, vorticity production near the spike tip, Atwood-dependence on the bubble and spike shape, Mach-dependence on the streamlining of the spike, and the combined Mach-Atwood growth rate effects. Whereas the qualitative behavior of the early-time growth is unaffected by the additional dimension, the intrinsic three-dimensionality of turbulent flows is likely to play an important role in the late-time growth of Rayleigh-Taylor instability.

A complete investigation of compressible Rayleigh-Taylor instability must consider the relevant parameters listed in Table 5.1. The simulations presented in this dissertation need to be extended to higher resolutions in order to achieve the large Reynolds number flows required to fully understand the true late-time behavior. Only then can it be concluded whether or not the growth of the single-mode system is an upper bound for the multi-mode compressible Rayleigh-Taylor instability. Furthermore, it must be determined whether or not the compressibility effects on the multi-mode instability growth have a reversal at high Mach numbers, as observed for the single-mode case.

The true nature of Rayleigh-Taylor instability will only be understood by looking deeper. High-resolution three-dimensional numerical simulations are the key to unlocking the true physics behind the seemingly simple interfacial instability that plays such a large role in countless systems across the universe: from supernovae to inertial confinement fusion; from galaxies to the Earth's rocks, atmosphere, and oceans; from the tiny shrimp living in those oceans, just looking for a meal, to a human enjoying a cup of coffee and the beauty of the extra-bubbly clouds in the sky. Look deeper, for only then will it be understood better.

Parameter	**Definition**	**Effect**	**Relevant Values**
Mach number	$M = \left(\frac{\rho_I g L}{P_0}\right)^{1/2}$	acoustic, compressibility, stratification	$10^{-2} - 10^{2}$
Specific heat ratio	$\gamma_I = \frac{c_{p_I}}{c_{v_I}}$	compressibility	$1 - 5/3$
Atwood number	$A = \frac{W_2 - W_1}{W_2 + W_1}$	variable density, stratification	$0.01 - 0.99$
Schmidt number	$Sc = \frac{\mu_I}{\rho_I D_I}$	mass diffusivity	$10^{-3} - 10^{3}$
Reynolds number	$Re = \frac{\rho_I g^{1/2} L^{3/2}}{\mu_I}$	viscous	$10^{2} - 10^{6}$
Prandtl number	$Pr = \frac{c_{p_I} \mu_I}{k_I}$	thermal diffusivity	$10^{-2} - 10^{2}$
Froude number	$Fr = \frac{U_0}{(gL)^{1/2}}$	gravitational, stratification	$10^{-2} - 10^{2}$
Peak wavelength	$\lambda_0^* = \frac{\lambda_0}{L}$	initial condition	$10^{-3} - 1$
Initial amplitude	$\eta_0^* = \frac{\eta_0}{L}$	initial condition	$10^{-6} - 1$
Interfacial thickness	$\delta^* = \frac{\delta}{L}$	interfacial gradient	$10^{-6} - 10^{-2}$
Interfacial resolution	$N_I = \frac{\delta}{\Delta}$	resolution	$8 - 32$

Table 5.1: The effects and ranges for the parameters relevant to simulations of compressible Rayleigh-Taylor instability are listed.

Bibliography

[1] U. Alon, J. Hecht, D. Mukamel, and D. Shvarts. Scale-invariant mixing rates of hydrodynamically unstable interfaces. Phys. Rev. Lett., **72**:2867–70, 1994.

[2] U. Alon, J. Hecht, D. Ofer, and D. Shvarts. Power laws and similarity of Rayleigh-Taylor and Richtmyer-Meshkov mixing fronts at all density ratios. Phys. Rev. Lett., **74**:534–7, 1995.

[3] U. Alon, D. Shvarts, and D. Mukamel. Scale-invariant regime in Rayleigh-Taylor bubble-front dynamics. Phys. Rev. E, **48**:1008–14, 1993.

[4] M. J. Andrews and D. B. Spalding. A simple experiment to investigate two-dimensional mixing by Rayleigh-Taylor instability. Phys. Fluids A, **2**:922–7, 1990.

[5] N. N. Anuchina, Y. A. Kucherenko, V. E. Neuvazhaev, V. N. Ogibina, L. I. Shibarshov, and V. G. Yakovlev. Turbulent mixing at an accelerating interface between liquids of different densities. Izv. Akad. Nauk SSSR, **6**:161–4, 1978.

[6] U. M. Ascher, S. J. Ruuth, and R. J. Spiteri. Implicit-explicit Runge-Kutta methods for time-dependent partial differential equations. Appl. Numer. Math., **25**:151–67, 1997.

[7] G. K. Batchelor, V. M. Canuto, and J. R. Chasnov. Homogeneous buoyancy-generated turbulence. J. Fluid Mech., **235**:349–78, 1992.

[8] M. J. Berger and J. Oliger. Adaptive mesh refinement for hyperbolic partial-differential equaitons. J. Comput. Phys., **53**:484–512, 1984.

[9] W. H. Cabot and A. W. Cook. Reynolds number effects on Rayleigh-Taylor instability with possible implications for type-Ia supernovae. Nat. Phys., **2**:562–8, 2006.

[10] W. H. Cabot, A. W. Cook, P. L. Miller, D. E. Laney, M. C. Miller, and H. R. Childs. Large-eddy simulation of Rayleigh-Taylor instability. Phys. Fluids, **17**, 2005.

[11] W. H. Calvin. The great climate flip-flop. Atlantic Monthly, **281**:47–64, 1998.

[12] S. Chandrasekhar. Hydrodynamic and Hydromagnetic Stability. (New York: Dover), 1981.

[13] C. Cherfils and K. O. MIkaelian. Simple model for the turbulent mixing width at an ablating surface. Phys. Fluids A-Fluid, **8**:522–35, 1996.

[14] D. Chung and D. I. Pullin. Direct numerical simulation and large-eddy simulation of stationary buoyancy-driven turbulence. J. Fluid Mech., **643**:279–308, 2010.

[15] A. W. Cook, W. Cabot, and P. L. Miller. The mixing transition in Rayleigh-Taylor instability. J. Fluid Mech., **511**:333–62, 2004.

[16] A. W. Cook and P. E. Dimotakis. Transition stages of Rayleigh-Taylor instability between miscible fluids. J. Fluid Mech., **443**:69–99, 2001.

[17] S. B. Dalziel. Rayliegh-Taylor instability - experiments with image-analysis. Dynam. Atmos. Oceans, **20**:127–53, 1993.

[18] S. B. Dalziel, P. F. Linden, and D. L. Youngs. Self-similarity and internal structure of turbulence induced by Rayleigh-Taylor instability. J. Fluid Mech., **399**:1–48, 1999.

[19] M. K. Davey and J. A. Whitehead. Rotating Rayleigh-Taylor instability as a model of sinking events in the ocean. Geophys. Astro. Fluid, **17**:237–53, 1981.

[20] G. Dimonte. Spanwise homogeneous buoyancy-drag model for Rayleigh-Taylor mixing and experimental evaluation. Phys. Plasmas, **7**:2255–69, 2000.

[21] G. Dimonte. Dependence of turbulent Rayleigh-Taylor instability on initial perturbations. Phys. Rev. E, **69**, 2004.

[22] G. Dimonte, P. Ramaprabhu, and M. Andrews. Rayleigh-Taylor instability with complex acceleration history. Phys. Rev. E, **76**, 2007.

[23] G. Dimonte, P. Ramaprabhu, D. L. Youngs, M. J. Andrews, and R. Rosner. Recent advances in the turbulent Rayleigh-Taylor instability. Phys. Plasmas, **12**, 2005.

[24] G. Dimonte and M. Schneider. Density ratio dependence of Rayleigh-Taylor mixing for sustained and impulsive acceleration histories. Phys. Fluids, **12**:304–21, 2000.

[25] G. Dimonte, D. L. Youngs, A. Dimits, S. Weber, M. Marinak, S. Wunsch, C. Garasi, A. Robinson, M. J. Andrews, P. Ramaprabhu, A. C. Calder, B. Fryxell, J. Biello, L. Dursi, P. MacNeice, K. Olson, P. Ricker, R. Rosner, F. Timmes, H. Tufo, Y. N. Young, and M. Zingale. A comparative study of the turbulent Rayleigh-Taylor instability using high-resolution three-dimensional numerical simulations: The Alpha-Group collaboration. Phys. Fluids, **16**:1668–93, 2004.

[26] P. E. Dimotakis. The mixing transition in turbulence. J. Fluid Mech., **409**:69–97, 2000.

[27] R. E. Duff, F. H. Harlow, and C. W. Hirt. Effects of diffusion on interface instability between gases. Phys. Fluids, **5**:417–25, 1962.

[28] D. R. Farley and L. M. Logory. Single-mode, nonlinear mix experiments at high Mach number using Nova. Astrophys. J. Suppl. Ser., **127**:311–6, 2000.

[29] N. Freed, D. Ofer, D. Shvarts, and S. A. Orszag. Two-phase flow-analysis of self-similar turbulent mixing by Rayleigh-Taylor instability. Phys. Fluids A-Fluid, **3**:912–8, 1991.

[30] S. Gauthier and B. Le Creurer. Compressibility effects in Rayleigh-Taylor instability-induced flows. Philos. T. R. Soc. A, **368**:1681–704, 2010.

[31] E. George, J. Glimm, X. L. Li, A. Marchese, and Z. L. Xu. A comparison of experimental, theoretical, and numerical simulation Rayleigh-Taylor mixing rates. P. Natl. Acad. Sci. USA, **99**:2587–92, 2002.

[32] P. Givi. Model-free simulations of turbulent reacting flows. Prog. Energy Combust. Sci., **15**:1–107, 1989.

[33] J. Glimm, J. W. Grove, X. L. Li, W. Oh, and D. H. Sharp. A critical analysis of Rayleigh-Taylor growth rates. J. Comput. Phys., **169**:652–77, 2001.

[34] J. Glimm, X. L. Li, and A. D. Lin. Nonuniform approach to terminal velocity for single mode Rayleigh-Taylor instability. Acta Math. Appl. Sinica, **18**:1–8, 2002.

[35] J. Glimm, X. L. Li, R. Menikoff, D. H. Sharp, and Q. Zhang. A numerical study of bubble interactions in Rayleigh-Taylor instability for compressible fluids. Phys. Fluids A-Fluid, **2**:2046–54, 1990.

[36] V. N. Goncharov. Analytical model of nonlinear, single-mode, classical Rayleigh-Taylor instability at arbitrary Atwood numbers. Phys. Rev. Lett., **88**, 2002.

[37] X. Y. He, S. Y. Chen, and R. Y. Zhang. A lattice Boltzmann scheme for incompressible multiphase flow and its application in simulation of Rayleigh-Taylor instability. J. Comput. Phys., **152**:642–63, 1999.

[38] J. Hecht, U. Alon, and D. Shvarts. Potential flow models of Rayleigh-Taylor and Richtmyer-Meshkov bubble fronts. Phys. Fluids, **6**:4019–30, 1994.

[39] J. Hecht, D. Ofer, U. Alon, D. Shvarts, S. A. Orszag, and R. L. McCrory. Three-dimensional simulations and analysis of the nonlinear stage of the Rayleigh-Taylor instability. Laser Part. Beams, **13**:423–40, 1995.

[40] Z. Huang, A. De Luca, T. J. Atherton, M. Bird, C. Rosenblatt, and P. Carles. Rayleigh-Taylor instability experiments with precise and arbitrary control of the initial interface shape. Phys. Rev. Lett., **99**, 2007.

[41] N. A. Inogamov. Turbulent stage of the Rayleigh-Taylor instability. Sov. Tech. Phys. Lett., **4**:299–300, 1978.

[42] N. K. R. Kevlahan and O. V. Vasilyev. An adaptive wavelet collocation method for fluid-structure interaction at high Reynolds numbers. SIAM J. Sci. Comput., **26**:1894–915, 2005.

[43] J. D. Kilkenny, S. G. Glendinning, S. W. Haan, B. A. Hammel, J. D. Lindl, D. Munro, B. A. Remington, S. V. Weber, J. P. Knauer, and C. P. Verdon. A review of the ablative stabilization of the Rayleigh-Taylor instability in regimes relevant to inertial confinement fusion. Phys. Plasmas, **1**:1379–89, 1994.

[44] J. P. Knauer, R. Betti, D. K. Bradley, T. R. Boehly, T. J. B. Collins, V. N. Goncharov, P. W. McKenty, D. D. Meyerhofer, V. A. Smalyuk, C. P. Verdon, S. G. Glendinning, D. H. Kalantar, and R. G. Watt. Single-mode, Rayleigh-Taylor growth-rate measurements on the OMEGA laser system. Phys. Plasmas, **7**:338–45, 2000.

[45] Y. A. Kucherenko, O. E. Shestachenko, Y. A. Piskunov, E. V. Sviridov, V. M. Medvedev, and A. I. Baishev. Experimental investigation into the self-similar mode of mixing of different density gases in the Earths gravitational field. Laser Part. Beams, **21**:385–8, 2003.

[46] M. A. Lafay, B. Le Creurer, and S. Gauthier. Compressibility effects on the Rayleigh-Taylor instability between miscible fluids. Europhys. Lett., **79**, 2007.

[47] D. Layzer. On the instability of superposed fluids in a gravitational field. Astrophys. J., **122**:1–12, 1955.

[48] X. L. Li. Study of three-dimensional Rayleigh-Taylor instability in compressible fluids through level set method and parallel computation. Phys. Fluids A-Fluid, **5**:1904–13, 1993.

[49] H. Lin, B. D. Storey, and A. J. Szeri. Rayleigh-Taylor instability of violently collapsing bubbles. Phys. Fluids, **14**:2925–8, 2002.

[50] P. F. Linden, J. M. Redondo, and D. L. Youngs. Molecular mixing in Rayleigh-Taylor instability. J. Fluid Mech., **265**:97–124, 1994.

[51] Q. Liu and O. V. Vasilyev. A Brinkman penalization method for compressible flows in complex geometries. J. Comput. Phys., **227**:946–66, 2007.

[52] Q. Liu and O. V. Vasilyev. Nonreflecting Boundary Conditions Based on Nonlinear Multidimensional Characteristics. Int. J. Num. Meth. Fluids, **62**:24–55, 2010.

[53] D. Livescu. Compressibility effects on the Rayleigh-Taylor instability growth between immiscible fluids. Phys. Fluids, **16**:118–27, 2004.

[54] D. Livescu and J. R. Ristorcelli. Buoyancy-driven variable-density turbulence. J. Fluid Mech., **591**:43–71, 2007.

[55] D. Livescu and J. R. Ristorcelli. Variable-density mixing in buoyancy-driven turbulence. J. Fluid Mech., **605**:145–80, 2008.

[56] D. Livescu, J. R. Ristorcelli, R. A. Gore, S. H. Dean, W. H. Cabot, and A. W. Cook. High-Reynolds number Rayleigh-Taylor turbulence. J. Turbul., **10**:1–32, 2009.

[57] N. J. Mueschke and O. Schilling. Investigation of Rayleigh-Taylor turbulence and mixing using direct numerical simulation with experimentally measure initial conditions. I. Comparison to experimental data. Phys. Fluids, **21**, 2009.

[58] N. J. Mueschke and O. Schilling. Investigation of Rayleigh-Taylor turbulence and mixing using direct numerical simulation with experimentally measure initial conditions. II. Dynamics of transitional flow and mixing statistics. Phys. Fluids, **21**, 2009.

[59] N. J. Mueschke, O. Schilling, D. L. Youngs, and M. J. Andrews. Measurements of molecular mixing in a high-Schmidt-number Rayleigh-Taylor mixing layer. J. Fluid Mech., **632**:17–48, 2009.

[60] B. J. Olson and A. W. Cook. Rayleigh-Taylor shock waves. Phys. Fluids, **19**, 2007.

[61] D. Oron, L. Arazi, D. Kartoon, A. Rikanati, U. Alon, and D. Shvarts. Dimensionality dependence of the Rayleigh-Taylor and Richtmyer-Meshkov instability late-time scaling laws. Phys. Plasmas, **8**:2883–9, 2001.

[62] G. Pacitto, C. Flament, J. C. Bacri, and M. Widom. Rayleigh-Taylor instability with magnetic fluids: experiment and theory. Phys. Rev. E, **62**:7941–8, 2000.

[63] T. J. Poinsot and S. K. Lele. Boundary-conditions for direct simulations of compressible viscous flows. J. Comput. Phys., **101**:104–29, 1992.

[64] P. Ramaprabhu and M. J. Andrews. Experimental investigation of Rayleigh-Taylor mixing at small Atwood numbers. J. Fluid Mech., **502**:233–71, 2004.

[65] P. Ramaprabhu and M. J. Andrews. On the initialization of Rayleigh-Taylor simulations. Phys. Fluids, **16**:L59–L62, 2004.

[66] P. Ramaprabhu and G. Dimonte. Single-mode dynamics of the Rayleigh-Taylor instability at any density ratio. Phys. Rev. E, **71**, 2005.

[67] P. Ramaprabhu, G. Dimonte, and M. J. Andrews. A numerical study of the influence of initial perturbations on the turbulent Rayleigh-Taylor instability. J. Fluid Mech., **536**:285–319, 2005.

[68] P. Ramaprabhu, G. Dimonte, Y. N. Young, A. C. Calder, and B. Fryxell. Limits of the potential flow approach to the single-mode Rayleigh-Taylor problem. Phys. Rev. E, **74**, 2006.

[69] L. Rayleigh. Investigation of the character of the equilibrium of an incompressible heavy fluid of variable density. Proc. R. Math. Soc., **14**:170–7, 1883.

[70] K. I. Read. Experimental investigation of turbulent mixing by Rayleigh-Taylor instability. Physica D, **12**:45–58, 1984.

[71] S. J. Reckinger, D. Livescu, and O. V. Vasilyev. Adaptive wavelet-collocation method simulations of Rayleigh-Taylor instability. Phys. Scr., **T142**, 2010.

[72] S. M. Reckinger, O. V. Vasilyev, and B. Fox-Kemper. Adaptive volume penalization for ocean modeling. Ocean Dynam., **62**:1201–15, 2012.

[73] J. D. Regele and O. V. Vasilyev. An adaptive wavelet-collocation method for shock computations. Int. J. of Comput. Fluid Dyn., **23**:503–18, 2009.

[74] B. A. Remington, S. V. Weber, M. M. Marinak, S. W. Haan, J. D. Kilkenny, R. J. Wallace, and G. Dimonte. Single-mode and multi-mode Rayleigh-Taylor experiments on NOVA. Phys. Plasmas, **2**:241–55, 1995.

[75] J. R. Ristorcelli and T. T. Clark. Rayleigh-Taylor turbulence: self-similar analysis and direct numerical simulations. J. Fluid Mech., **507**:213–53, 2004.

[76] D. L. Sandoval. The dynamics of variable density turbulence. PhD thesis, Univiversity of Washington, 1995.

[77] D. L. Sandoval, T. T. Clark, and J. J. Riley. Buoyancy-generated variable density turbulence. Proc. IUTAM Symp. on Variable Density Low-Speed, pages 847–64, 1996.

[78] W. Schmidt. Turbulence - From tea kettles to exploding stars. Nat. Phys., **2**:505–6, 2006.

[79] K. Schneider and O. V. Vasilyev. Wavelet methods in computational fluid dynamics. Annu. Rev. Fluid Mech., **42**:473–503, 2010.

[80] C. W. Shu and S. Osher. Efficient implementation of essentially non-osicllatory shock-capturing schemes. J. of Comput. Phys., **77**:439–71, 1988.

[81] W. Sweldens. The lifting scheme: A construction of second generation wavelets. SIAM J. Math. Anal., **29**:511–46, 1998.

[82] G. Taylor. The instability of liquid surfaces when accelerated in a direction perpendicular to their planes .1. Proc. R. Soc. London, Ser. A, **201**:192–6, 1950.

[83] K. W. Thompson. Time dependent boundary conditions for hyperbolic systems. J. Comput. Phys., **68**:1–24, 1987.

[84] O. V. Vasilyev. Solving multi-dimensional evolution problems with localized structures using second generation wavelets. Int. J. of Comput. Fluid Dyn., **17**:151–68, 2003.

[85] O. V. Vasilyev and C. Bowman. Second-generation wavelet collocation method for the solution of partial differential equations. J. of Comput. Phys., **165**:660–93, 2000.

[86] O. V. Vasilyev and S. Paolucci. A fast adaptive wavelet collocation algorithm for multidimensional PDEs. J. Comput. Phys., **138**:16–56, 1997.

[87] M. Versluis, B. Schmitz, A. von der Heydt, and D. Lohse. How snapping shrimp snap: Through cavitating bubbles. Science, **289**:2114–7, 2000.

[88] J. T. Waddell, C. E. Niederhaus, and J. W. Jacobs. Experimental study of Rayleigh-Taylor instability: Low Atwood number liquid systems with single-mode initial perturbations. Phys. Fluids, **13**:1263–73, 2001.

[89] T. Wei and D. Livescu. Late-time quadratic growth in single-mode Rayleigh-Taylor instability. Phys. Rev. E, **86**, 2012.

[90] F. A. Williams. Combustion Theory. (Menlo Park: Benjamin/Cummings), 1985.

[91] W. D. Woidt. Finite element calculations applied to salt dome analysis. Tectonophysics, pages 369–86, 1978.

[92] Y. N. Young, H. Tufo, A. Dubey, and R. Rosner. On the miscible Rayleigh-Taylor instability: two and three dimensions. J. Fluid Mech., **447**:377–408, 2001.

[93] D. L. Youngs. Numerical-simulation of turbulent mixing by Rayleigh-Taylor instability. Physica D, **12**:32–44, 1984.

[94] D. L. Youngs. Modeling turbulent mixing by Rayleigh-Taylor instability. Physica D, **37**:270–87, 1989.

[95] D. L. Youngs. Three-dimensional numerical-simulation of turbulent mixing by Rayleigh-Taylor instability. Phys. Fluids A-Fluid, **3**:1312–20, 1991.

[96] D. L. Youngs. Numerical-simulation of mixing by Rayleigh-Taylor and Richtmyer-Meshkov instabilities. Laser Part. Beams, **12**:725–50, 1994.

[97] D. L. Youngs. Application of monotone integrated large eddy simulation to Rayleigh-Taylor mixing. Philos. T. R. Soc. A, **367**:2971–83, 2009.

[98] H. Yu and D. Livescu. Rayleigh-Taylor instability in cylindrical geometry with compressible fluids. Phys. Fluids, **20**, 2008.

[99] M. Zingale, S. E. Woosley, C. A. Rendleman, M. S. Day, and J. B. Bell. Three-dimensional numerical simulations of Rayleigh-Taylor unstable flames in type Ia supernovae. Astrophys. J., **632**:1021–34, 2005.

[100] E. Zweibel. Galactic magnetic-fields - spinning a tangled web. Nature, **352**:755–6, 1991.